

H-BN NANOSTRUCTURES: SYNTHESIS AND APPLICATIONS

by

DENİZ KÖKEN

Submitted to Graduate School of Engineering and Natural Sciences

in partial fulfillment of

the requirements for the degree of

Doctor of Philosophy

Sabancı University

Fall 2021

H-BN NANOSTRUCTURES: SYNTHESIS AND APPLICATIONS

APPROVED BY

Assoc. Prof. Dr. Fevzi Çakmak Cebeci
(Dissertation Supervisor)

Prof. Dr. Yusuf Z. Menceloglu
(Jury Member)

Asst. Prof. Dr. Nuri Solak
(Jury Member)

Prof. Dr. Burç Mısırlıoğlu
(Jury Member)

Assoc. Prof. Dr. Hülya Cebeci
(Jury Member)

DATE OF APPROVAL: 16.12.2021

©Deniz Köken 2021

All Rights Reserved

ABSTRACT

H-BN NANOSTRUCTURES: SYNTHESIS AND APPLICATIONS

DENIZ KÖKEN

PhD Dissertation, December 2021

Dissertation Supervisor: Assoc. Prof. Dr. Fevzi Çakmak Cebeci

Keywords: Boron nitride, Boron nitride nanotubes, Interface Engineering, Microdroplet testing, Dielectric materials, Polymer composites, Boron minerals, Chemical vapor deposition, Surface functionalization

Exploring boron nitride (BN) structures at materials science carries a great potential for evolving technology. BN nano/microstructures consist of alternating B and N atoms with sp^2 and sp^3 hybridization that provides excellent mechanical, thermal, thermomechanical, and electrical properties with strong chemical and thermal stability. Lately, special attention has been given to BN nano/microstructures such as BN nanotubes (BNNT), BN microfibers (BN-MF), and BN nano/microparticles (BN-NP, BN-MP). Incorporating the properties as mentioned earlier BN nano/microstructures with polymers and/or other ceramics can provide strong structural composites, dielectric insulating materials, *etc.* However, due to difficulties in the synthesis of the BN nano/microstructures and challenges encountered during the dispersion of the BN inside the composite matrix inhibit the comprehensive research. Herein, we show two possible applications of the BN nano/microstructures as well as a novel, low-cost synthesis method

for the synthesis of boron nitride nanotubes BNNT. We found that decoration of SiC fiber surfaces with “fuzzy fiber” BNNTs can lead to increased interfacial shear strength (IFSS) that can result in composites with better mechanical properties. Moreover, we have evaluated the dielectric performance of the BN/Resin composites and showed that both the dielectric constant and the dielectric loss of the composites lower significantly whereas the glass transition temperature of the composites increased. Finally, we have proposed a modified chemical vapor deposition (CVD) method that utilizes colemanite as boron precursor and sulfur-molecules to increase the catalytic activity of the Fe_2O_3 catalyst. Our results showed that, with the addition of thiophene, BNNT synthesis is achievable at 1050 °C. Our works have shown that BN nano/microstructures have a wide range of applications from CMCs to dielectric insulators and synthesis of BNNTs can be accomplished in a low-cost, environmentally friendly system.

ÖZET

H-BN NANO YAPILAR: SENTEZ VE UYGULAMALARI

DENİZ KÖKEN

Doktora Tezi, Aralık, 2021

Tez Danışmanı: Doç. Dr. Fevzi Çakmak Cebeci

Anahtar Kelimeler: Bor nitrür, Bor nitrür nano tüpler, Ara yüzey mühendisliği, Mikro damla testi, Dielektrik malzemeler, Polimer kompozitler, Bor mineralleri, Kimyasal gaz biriktirme, yüzey fonksiyonlandırılması

Malzeme biliminde bor nitrür (BN) yapılarının araştırılması gelişen teknoloji için büyük bir potansiyel taşımaktadır. BN nano/mikroyapıları, güçlü kimyasal ve termal stabilité ile mükemmel mekanik, termal, termomekanik ve elektronik özellikler sağlayan sp₂ ve sp₃ hibridizasyonuna sahip sıralı B ve N atomlarından oluşur. Son zamanlarda, BN nanotüpler (BNNT), BN mikrofiberler (BN-MF) ve BN nano/mikropartiküller (BN-NP, BN-MP) gibi BN nano/mikroyapılarına özel önem verilmiştir. BN nano/mikro yapıların yukarıda bahsedilen özelliklerinin polimerler ve/veya diğer seramiklerle birleştirilmesi, güçlü yapısal kompozitler, dielektrik yalıtmalzemeleri vb. üretimine olanak sağlayacaktır. Ancak, BN nano/mikroyapılarının sentezinin zorluğu ve BN'nin kompozit matrisi içerisinde zor dağılıyor olması ayrıntılı bir araştırmanın yapılmasını zorlaştırmıştır. Bu tez çalışmasında, BN nano/mikroyapılarının iki olası uygulamasını ve

bor nitrür nanotüplerinin sentezi için yeni, düşük maliyetli bir sentez yöntemini gösterdik. SiC fiber yüzeylerinin “bulanık fiber” BNNT'lerle süslenmesinin, daha iyi mekanik özelliklere sahip kompozitlerle sonuçlanabilecek artan arayüzey kesme mukavemetine (IFSS) yol açabileceğini bulduk. Ayrıca, BN/Reçine kompozitlerinin dielektrik performansını değerlendirdik ve kompozitlerin hem dielektrik sabitinin hem de dielektrik kaybının önemli ölçüde düştüğünü, buna karşın kompozitlerin camsı geçiş sıcaklığının arttığını gösterdik. Son olarak, BNNT sentezi için bor öncüsü olarak kolemanit ve Fe_2O_3 katalizörünün katalitik aktivitesini artırmak için kükürt molekülleri kullanan modifiye edilmiş bir kimyasal buhar biriktirme (CVD) yöntemi önerdik. Sonuçlarımız, tiyofen ilavesiyle BNNT sentezinin 1050 °C'de elde edilebileceğini gösterdi. Çalışmalarımız, BN nano/mikro yapıların CMC'lerden dielektrik yalıtkanlara kadar geniş bir uygulama alanına sahip olduğunu ve BNNT'lerin sentezinin düşük maliyetli, çevre dostu bir sistemde gerçekleştirilebileceğini göstermiştir.

ACKNOWLEDGEMENTS

First and foremost, I would like to extend my deepest gratitude towards my thesis advisor Assoc. Prof. Dr. Fevzi Çakmak Cebeci for his unending support and compassion he provided through my thesis study, his unwavering patience, motivation and, wisdom he shared with me during my PhD. Ever since I have started my academic career in 2014, he has been my mentor and academic idol. He has been there for me when I was going through rough patches as well as at my happiest day. I could not have selected a better advisor and a teacher for my academic career.

I would like to express my endless admiration to Dr. Hülya Cebeci for her irreplaceable role during my Ph.D. studies. She had provided me with every tool and opportunity necessary to succeed and supported me in every possible way she can. Our discussions on various aspects of my research allowed me to mature into a Ph.D. candidate.

Along with my advisor, I would like to thank Dr. Yusuf Z. Mencelioğlu, Dr. Nuri Solak, Dr. Burç Mısırlıoğlu and of my thesis committee for their invaluable comments and feedback which allowed completion of this thesis. Their inputs along the way helped shape the foundation of this thesis which I am deeply grateful for.

I would also like to acknowledge everyone who collaborated with me during my thesis research. Ayşemin Top, Fırat Tugut, Beyza Bozali, Dr. Elid Özden-Yenigün, Dr. Merve Senem Seven, Dilan Kaya, Dr. Bekir Dizman, Dr. Serkan Ünal, Dr. Pelin Sungur and Dr. Gözde İnce. I believe any scientific research to be accumulation of knowledge from different people and they shared their knowledge and experience with me to complete my research. I will forever be in debt of them.

Dr. Mehmet Ali Gülgün and Dr. Cleva W. Ow-Yang, the two people I look up to. I am honored to be their student and lucky to have them to speak whether about academic research or when I need a life advice. Their doors were always open to me and I can't even describe how much this meant to me. If I am the person I am today, they are to thank for.

My campus family, no words can describe my love and admiration I have for you. Dr. Omid and Tuğçe Mohammad Moradi, Dr. Senem and Utku Seven, Dr. Aysu Yurdeşen, and many more friends I made along the way. You have become the irreplaceable part of my life, my support through the hard times and the architects of the fond memories I will always cherish.

Most importantly, my family. I would like to show my gratitude to my parents, Hakkı and Rahime Köken by dedicating this thesis to them. I am unbelievably lucky to have these two amazing people as my parents. They are the best parents any kid can wish for. They are the foundation of anything I have achieved and will ever achieve.

Last but not least, I would like to thank my wife, Rüya Özlem for making me whole. Her love and compassion provided me the necessary tools to complete this thesis. She has been on my side since the day we meet and I can only hope to be the person she thinks of I am.

To my family, blood and chosen

TABLE OF CONTENTS

ABSTRACT.....	iv
ÖZET	vi
ACKNOWLEDGEMENTS	viii
TABLE OF CONTENTS	xi
LIST OF FIGURES.....	xiv
LIST OF TABLES.....	xviii
LIST OF ABBREVIATIONS	xviii
LIST OF SYMBOLS AND NOTATIONS.....	xx
Chapter 1 INTRODUCTION	23
1.1 Introduction.....	23
1.2 Motivation.....	24
1.3 Focus.....	25
1.4 Objectives	26
Chapter 2 AN EFFECTIVE GROWTH OF HIERARCHICAL BNNTs/SiC FIBERS WITH ENHANCED INTERFACIAL PROPERTIES	30
2.1 Introduction.....	30
2.2 Experimental.....	43
2.2.1 Techniques and Methods Used.....	43
2.2.2 Desizing of the Fibers	44
2.2.3 Surface Decoration of the SiC fibers via Dip-coating	45
2.2.4 Growth of “Fuzzy Fiber” BNNTs on the SiC _f Surfaces	47

2.2.5 Preparation of SiC for Tensile Testing	49
2.2.6 Microbond Test Sample Preparation	50
2.3 Results and Discussion	53
2.3.1 Techniques and Methods Used	53
2.3.2 BNNT Growth on The SiC fibers	53
2.3.3 Parametric Study on Growth Conditions	57
2.3.4 Mechanical Characterization of BNNT/SiC _f Hierarchical Structure	62
2.3.4.1 Tensile Testing of Single SiC Fiber	62
2.3.4.2 Interfacial Shear Strength of the BNNT/SiC _f Hierarchical Structures	65
2.4 Conclusions	70
2.5 Acknowledgments	71
Chapter 3 H-BN NANO/MICROSTRUCTURE REINFORCED NORYL COMPOSITES AS INSULATING DIELECTRIC MATERIALS.....	72
3.1 Introduction	72
3.2 Experimental	85
3.2.1 Techniques and Methods Used	85
3.2.2 Synthesis of Boron Nitride Microfibers	86
3.2.3 Fabrication of BN/Noryl Composites	87
3.3 Results and Discussion	89
3.3.1 Synthesis of BN-MF from M.2B precursor	89
3.3.2 BN/Noryl Composite Fabrication	96
3.3.2.1 SEM analysis of the Composites	96
3.3.2.2 Determination of Glass Transition Temperatures of the BN/Noryl Composites	99
3.3.2.3 Dielectric Properties of BN/Noryl Composites	103
3.4 Conclusions	108
Chapter 4 LOW-TEMPERATURE SYNTHESIS of BORON NOTRODE NANOTUBES FROM BORON MINERALS ASSISTED by SULFUR BASED MOLECULES	110

4.1 Introduction.....	110
4.2 Experimental.....	118
4.2.1 Chemicals and Equipment Used.....	118
4.2.2 Synthesis of BNNTs via GVT-BOCVD method.....	119
4.2.3 CB-iCVD Deposition of PTFE on the Surface of the As-synthesized BNNTs.	
.....	120
4.3 Results and Discussion	122
4.3.1 BNNT Synthesis from Colemanite Mineral	123
4.3.2 Temperature Optimization of the BNNT Synthesis	126
4.3.3 The Efficiency of the S-Based Molecules	130
4.3.4 Synthesis of BNNTs from Ulexite and Etidot-67 Minerals.....	133
4.3.5 CB-iCVD Deposition of PTFE on the Surfaces of BNNTS.....	137
4.4 Conclusions.....	139
4.5 Acknowledgments	140
Chapter 5 CONCLUSIONS AND FUTURE WORK.....	141
REFERENCES.....	143
CURRICULUM VITAE.....	161

LIST OF FIGURES

Figure 1.1 Flow Chart of the research carried out within this thesis.....	29
Figure 2.1 Schematic of fiber debonding and fiber pullout mechanisms observed in fiber-reinforced composites [21].	33
Figure 2.2 Crack bridging sequence observed in fiber-reinforced composites. (1) Crack deflection, (2) fiber debonding, (3) fiber pull-out, (4) growth of bridging, (5) steady-state bridging zone [21].	34
Figure 2.3 Stress-strain curve for the continuous fiber-reinforced composite. Although not depicted, too weak interface strength would have resulted in lower mechanical properties than of optimum interface strength composite due to diminishing of the load transfer capabilities of the composite [24].....	35
Figure 2.4 Flexural Strength vs PyC layer thickness plot for the single-layered PyC coatings on SiC _f /SiC composites clearly showing the enhancement of the mechanical properties of the composite by PyC coating. 150nm coating thickness appears to have optimum mechanical properties for the composite [39].	37
Figure 2.5 TEM image of the SiC fiber micro composite prepared by Lee <i>et al.</i> [43] Crack deflection and fiber pull out happened within the zirconia phased shown above in dark contrast.....	38
Figure 2.6 Schematic of inside debonding (i.e. where debonding happens between the fiber and the interface) and outside debonding (i.e. where debonding happens between the matrix and BN interphase) [36].	39
Figure 2.7 Mechanical properties of the SiC/SiC composites tested during the research done by Morscher and his group [36].....	40
Figure 2.8 Flow chart of the production of BNNT/SiC _f hierarchical structures research.	43
Figure 2.9 Schematic of the surface decoration. (a) Plasma treatment of the fiber surface, (b) dip coating of the fibers inside catalyst/ethanol solution and (c) Reduction of the catalyst particles under H atmosphere	46
Figure 2.10 Schematic of the sample preparation for the tensile testing	50
Figure 2.11 Plot of the weight of the samples measured by the UTM vs measured by the analytical balance with a fitted trendline	52

Figure 2.12 SEM images of (a) chemically desized, plasma-treated, and dip catalyzed SiC fiber, (b) SiC fiber with BNNT “fuzzy fiber” grown on it at 1200 °C for 60 minutes, (c) selectively etched surface of the SiC fiber showing the nucleation sites on the surface, and (d) cross-section image of the fiber with a preserved circular cross-section of the fiber.....	55
Figure 2.13 (a) HRTEM image of the single BNNT with hollow core and dark fringes present, confirming the tube morphology of the as-grown BNNTs, (b) profile analysis of single BNNTs with each peak on the graphic representing a wall in the tube structure, (c) EELS analysis of the BNNTs with strong B and N K-edge showing the chemical composition of the BNNTs. (d) Selective area diffraction pattern of the single BNNT showing the circular halo around the tube axes.	56
Figure 2.14 (a) RAMAN spectra of the as-grown BNNTs showing one strong and narrow peak at E_{2g} in-plane vibration band, (b) FTIR spectra of the BNNTs demonstrating characteristic absorption peaks of the BNNTs.....	57
Figure 2.15 SEM images of BNNTs grown at (a) 1000 °C, (b) 1100 °C and (c) 1200 °C	58
Figure 2.16 SEM images of the fibers with the BNNT growth time of (a) 30 minutes, (b) 60 minutes and (c) 90 minutes at 1200 °C	59
Figure 2.17 EDX spectrums of SiC fibers with a soaking time of (a) without soaking, (b) 15 minutes, (c) 60 minutes, and (d) 120 minutes.....	60
Figure 2.18 SEM images of fibers that were soaked in catalyst solution for (a) without any soaking, (b) 15 minutes, (c) 60 minutes, and (d) 120 minutes.....	61
Figure 2.19 (a) Tensile test setup and prepared specimen, (b) tensile test results of T-2, T-3, T-5, and BNNTs/SiCf, (c) XRD spectrum of T-2, T-3, T-5 samples. SEM images of (d) T-3, and (e) T-4.....	64
Figure 2.20 (a) Photo and (b) schematic view of the home-built microdroplet test setup, (c) SEM image of fiber with the epoxy droplet, (d) BNNT coated SiCf sample after microbond test. Load – displacement curves of (e) as-received SiCf and (f) BNNTs/SiCf.....	66
Figure 2.21 Force vs Embedded area plot for the neat SiCf and BNNT/SiCf with regression line intercepting the origin.	69
Figure 3.1 Evolution of interconnect delay and intrinsic gate delay versus feature size [123].....	73
Figure 3.2 Dependence of permittivity and loss to frequency [127].	75
Figure 3.3 Roadmap of integration of DLC to SiCOH interconnect materials [128]....	76
Figure 3.4 Thermal conductivities of the as-prepared composites at 55 °C show the bad performance of the silica fillers [143].....	78
Figure 3.5 Effect of orientation of the h-BN filler on the anisotropic thermal diffusivity of the PI films [155].....	79
Figure 3.6 Change of (a) dielectric constant and (a) dielectric loss with the frequency and the BNNT filler amount [122].	81
Figure 3.7 (a) The experimental flow of the BNMF synthesis, (b) photograph of the as-synthesized product, (c, d) Schematic of the BNMF, (e, f) showcase of the low density of the BNMFs, (g, h) large size BNMF foam, (i, j, k) SEM images of the BNMFs and (l) TEM image of the single fiber.....	83

Figure 3.8 (a) The precursor placed inside the alumina boat, (b) alumina boat covered with silica substrates to prevent precursor loss, (c) 3-zone tube furnace used for the pyrolysis, (d) schematic of the pyrolysis step, (e) final BN-MF white product.	87
Figure 3.9 The experimental flow of the BN-MF synthesis showing all three processes.	89
Figure 3.10 (a) Low magnification SEM image of the M. 2B precursors and (b) cross-section of the single M.2B precursor fiber.	90
Figure 3.11 (a) Low magnification SEM image of the BN-MF and (b) high magnification SEM image of the BN-MF showing the decreased fiber diameter.....	91
Figure 3.12 (a) TEM image of a single BNMF showing the porous structure of the fibers, (b) polycrystalline structure of the BNMFs with stacked BN layers, inset showing the SAED. (c) Tip of the BNMF with porous channels running inside the fibers, (d) Interwall distance of BN layers, (e) EELS plot of the fibers showing the characteristic B and N K-edge.	92
Figure 3.13 SEM images of the BN-MF with pyrolysis temperature of (a) 1000 °C, (b) 1100 °C, (c) 1200 °C, and (d) 1300 °C.....	93
Figure 3.14 (a) RAMAN spectrum of BN-MF pyrolyzed at different temperatures, (b) FTIR spectrum of BN-MF pyrolyzed at 1100 °C.	94
Figure 3.15 Molecular diagram of the precursor to BN-MF transformation during pyrolysis [164].	95
Figure 3.16 SEM images of (a) BN-MP, (b) BN-NP and FTIR spectrums of (c) BN-MP and (d) BN-NP	97
Figure 3.17 Isotherm linear plots of the h-BN fillers.	98
Figure 3.18 SEM images of the (a) neat noryl resin, (b) BN-MP, (c) BN-NP, (d) BN-MF with 1.5 w % for all fillers.	99
Figure 3.19 (a) DSC curves of 2 nd heating cycles of the composites, (b) T _g of the BN/noryl composites.	100
Figure 3.20 (a) Loss factor tan(delta) plot of the BN/Noryl composites, (b) T _g of the composites with different filler morphology and filler amount.....	101
Figure 3.21 (a) E (modulus) vs temperature plot of the composites, (b) Calculated E (modulus) values of the composites.....	102
Figure 3.22 Change of dielectric properties of the composites in respect to filler ratio.	104
Figure 4.1 (a) Schematic of the experimental setup used by Lee et al. and (b) BNNT deposition on the walls of the alumina boat [67].	112
Figure 4.2 Schematic of induction plasma processing system designed by Kim et al. [211] excluding the filtration chamber.	115
Figure 4.3 (a) The schematic representation of the reaction chamber for the BNNT synthesis. (b) Furnace system used in the BNNT synthesis.	119
Figure 4.4 Photograph of the CB-iCVD setup we have used for the deposition of the PTFE.	121
Figure 4.5 SEM images of the synthesis products when (a) Ulexite and (b) Etidot-67 was used as boron precursors.....	123
Figure 4.6 (a) SEM image of the BNNT clusters collected on the Si wafers at 1200 °C synthesis temperature. (b) TEM image of the single BNNT synthesized at 1200 °C showing hallow center and darker walls. (c) EELS of the single BNNT with distinct B	

and N edges, (d) FTIR spectrum of the BNNTs, (e) RAMAN spectrum of the Colemanite and BNNTs.....	124
Figure 4.7 SEM images of the BNNTs synthesized at (a) 1050 °C, (b) 1100 °C, (c) 1150 °C, and (d) 1200 °C.	127
Figure 4.8 (a) SEM image of the BNNTs synthesized at 1050 °C, (b) TEM image of single BNNT with a hollow center, (c) EELS of the BNNT showing the characteristic B and N edges.....	129
Figure 4.9 Chemical structures of the S-based molecules used in the BNNT synthesis.	131
Figure 4.10 SEM images of the products synthesized (a) without any S-based molecule, with (b) thiophene, (c) L-cystine and (d) L-methionine	131
Figure 4.11 SEM images of BNNTs synthesized with Ulexite precursor at (a) 1050 °C and (b) 1200 °C. (c) RAMAN spectrum of the BNNTs.	136
Figure 4.12 SEM images of synthesis products at (a) 1050 °C and (b) 1200 °C from Etidot-67.	136
Figure 4.13 (a) SEM image of the non-coated as-synthesized BNNTs, and (b) its EDX spectrum. (c) SEM image of the PTFE coated as-synthesized BNNTs and (d) its EDX spectrum.....	138
Figure 4.14 (a) TEM image of the single PTFE coated BNNT showing the (1) amorphous polymer coating, (2) parallel aligned walls, and (3) hallow tube center. (b) EELS of the single coated BNNT showing B and N K-edge from BNNT and C K-edge from polymer coating.....	139

LIST OF TABLES

Table 2-1 Properties of β -SiC phase which forms the SiC fiber [13].....	31
Table 2-2 The measured weights by analytical balance and by UTM.....	51
Table 2-3 Equation of fitted trendline.....	52
Table 2-4 Tensile strength values and Weibull modulus of the SiC _f samples.....	63
Table 2-5 Calculated IFSS values of the SiC fiber samples	68
Table 3-1 Pyrolysis conditions.	87
Table 3-2 Curing conditions of the BN/Noryl composites	88
Table 3-3 Reactions during the transformation of precursor to BN-MF reported by Wu <i>et al.</i> [164].....	95
Table 3-4 Dielectric properties of the as-fabricated composites at 10 GHz.....	104
Table 4-1. Chemical composition of the boron minerals used in this study. (*: in ppm)	134

LIST OF ABBREVIATIONS

BET: Brown-Emmet-Teller

BN: Boron nitride

BN-MF: Boron nitride microfiber

BN-MP: Boron nitride microparticle

BN-NP: Boron nitride nanoparticle

BNNT: Boron nitride nanotube

CB-iCVD: Closed-batch initiated chemical vapor deposition

CMC: Ceramic matrix composite

CNT: Carbon nanotube

CVD: Chemical vapor deposition

CVI: Chemical vapor infiltration

DMA: Dynamic mechanical analysis

DSC: Differential scanning calorimetry

EDX: Energy dispersive X-ray analysis

EELS: Electron energy loss spectroscopy

F/M: Fiber matrix interface

FTIR: Fourier-transform infrared spectroscopy

GVT-BOCVD: Growth vapor trapping boron oxide chemical vapor deposition

IC: Integrated circuit

iCVD: Initiated chemical vapor deposition

IFSS: Interfacial shear strength

ILSS: Interlaminar shear strength

MMC: Metal matrix composite

MWCNT: Multi-walled carbon nanotube

PLS: Proportional limit stress

PyC: Pyrolytic carbon

SEM: Scanning electron microscope

SiC_f: Silicon carbide fiber

SPDR: Split post dielectric resonance

TEM: Transmission electron microscope

UFS: Ultimate flexural stress

UTM: Universal testing machine

VLS: Vapor-liquid-solid

LIST OF SYMBOLS AND NOTATIONS

T_g : Glass transition temperature

τ : Sliding resistance

P_N : Probability of whisker nucleation

T : Temperature

α : Super saturation ratio

σ : Surface energy

m : Shape parameter

σ_0 : Scale parameter

P_f : Distribution function of strength

F_{Max} : Maximum force

l_e : Embedded length

d_f : Fiber diameter

ρ : Resistance

ϵ : Dielectric constant

ϵ_0 : Dielectric constant of vacuum

ϵ' : Permittivity

ϵ'' : Dielectric loss

L: Length

P: Distance between conducting lines

T: Signal delay time

R: Resistance

C: Capacitance

E: Young modulus

α_e : Electronic polarization

α_d : Distortion polarization

μ : Orientation polarization

Q: Heat

m: Mass

C_p : Heat capacity

Chapter 1 INTRODUCTION

1.1 Introduction

The integrating nano/microparticles into state-of-the-art technology is a significant part of materials science and nanoengineering. The utilization of extraordinary mechanical, thermal, electrical, and optical properties of these nano/microstructures as a composite reinforcement material are the driving force of this thesis. Various aspects of boron nitride (BN) nanostructures with respect to their use as ceramic reinforcement material are investigated. Their effect on the surface interactions between fiber filler and matrix when boron nitride nanotubes (BNNTs) were used as surface decorating structures on the fiber filler was evaluated in terms of interfacial shear strength (IFSS) between fiber and the matrix. Dielectric properties of the varying morphology BN-reinforced polymers were analyzed in terms of dielectric constant and dielectric loss changes. Lastly, low-cost, novel, and environmentally friendly synthesis routes for BNNTs were proposed to promote the use of BN structures in composite applications.

1.2 Motivation

Although BN nano/microstructures have various application fields, we have addressed the following three topics within this thesis.

1. High thermal stability, chemical resistance, high specific surface area, and excellent thermomechanical properties of the BNNTs make them ideal candidates for use in ceramic matrix composites. Design of BNNT/Ceramic fiber hierarchical structures to provide better interface interactions between the ceramic fiber filler and matrix can lead to exploitation of the full potential of the ceramic fiber fillers in terms of thermomechanical properties.
2. Miniaturization of the electronic devices have become a bottleneck for the development of next generation electronics. The need for low dielectric constant and dielectric loss polymer composites are critical to achieving high signal propagating speed with low signal propagating loss that allows miniaturization. Insulating BN nano/microstructures offers low dielectric properties as well as improved thermal conductivity which makes them highly sought-after dielectric fillers. However, the relationship between the morphology of the filler and the dielectric property of the composite material is relatively unknown. Evaluation of different BN morphologies in terms of their effect on dielectric properties at high frequencies can lead to new application fields for the BN.
3. Low-cost, novel, and environmentally friendly synthesis routes for the BNNTs are critical to realizing their full potential. So far, the traditional methods that have been used to synthesize BNNTs suffer from the use of dangerous chemicals, complex instrumentation, and the requirement of high temperatures, all of which drive the cost of the BNNTs upwards. The utilization of boron minerals (which are abundant in Turkey) with the assistance of S-based molecules can provide a more suitable route to synthesize BNNTs.

1.3 Focus

In a time where nanoengineering and nanomaterials are the driving force behind most technological advancements, boron nitride nano/microstructures are one of the intriguing materials at state-of-the-art technologies such as structural composites and dielectric insulating materials.

Ceramic matrix composites that can withstand harsh environments as well as elevated temperatures offer exciting opportunities in aerospace, automotive, and gas turbine industries with their high thermal and oxidative stability, wear resistance, low density, and high strength. Several routes to improve before mentioned properties of the ceramic matrix composites (CMCs) have been proposed, and BNNTs show a promising future in such approaches. The combination of the unique morphology of the BNNTs and their excellent properties coupled with the intrinsic properties of the ceramic fiber fillers provides CMCs that showcase their true potential. We have focused our research to better understand the effect of the BNNTs on the interface interactions between the individual fiber and the matrix and evaluated the hierarchical structures thereof using straightforward mechanical testing utilizing polymer matrix.

Another exciting aspect of the BN materials has been their stable electronic properties, especially their high band-gap as well as low dielectric constant and loss. Development of interconnecting insulating materials to prevent RC delay of the electronic systems allows efficient miniaturization of devices which is expected as the technology progresses forward. Lately, polymer composites have been offered as a low dielectric constant and dielectric loss alternative for insulating materials. However, their low thermal conductivity limits their performance. Literature suggests that reinforcement of these polymers with ceramic particles can enhance their thermal conductivity. BN materials have been evaluated to this end and showed promising results. Contrary to the literature, we have focused our research on the morphology of the BN filler and its effect on the

dielectric properties of the polymer. The relationship between the particle size and the morphology offers a unique perspective to understand BN fillers.

During our research, we have evaluated applications of the BN materials and assessed their potential. However, as our studies continued, we have noticed one of the drawbacks of working with BN nano/microstructures is the synthesis. Both BNNTs and boron nitride microfibers (BN-MFs) suffer from similar challenges during synthesis (low yield, high cost, complex instrumentation). Although recent literature showed that BN-MFs could be synthesized without use of complex processes, the synthesis of BNNTs is still a challenging topic. As a result, we have focused our research on studying novel, low-cost, and scalable synthesis routes for BNNTs. Considering the availability of boron minerals in Turkey, our aim became the evaluation of different boron minerals as boron precursors along with reduction of synthesis temperature to allow inexpensive BNNT synthesis.

1.4 Objectives

The two main objectives of the thesis with respect to boron nitride nano/microstructures are:

To showcase possible applications of BN structures with respect to their thermomechanical properties and dielectric properties via hierarchical BN structures and BN/polymer composites respectively.

To introduce a possible low-cost, novel, and environmentally friendly synthesis route that utilizes boron minerals as precursors via growth vapor trapping boron oxide chemical vapor deposition (GVT-BOCVD) at relatively low temperatures which allows scalability to BNNT synthesis.

Experimental work is mainly focused on BNNTs, BN-MF, and BN micro/nanoparticles. The thesis can be divided into three parts with distinctive aims mainly focused on BN structures as a key component.

The research presented in chapter 2 is titled “An Effective Growth of Hierarchical BNNTs/SiC Fibers with Enhanced Interfacial Properties”. This chapter has been published as a research article. Although this work does not cover the ceramic matrix composites, it evaluates one of the most important parameters that dictate the final properties them, the interface interactions. This chapter mainly aimed towards the growth of the BNNTs on the surfaces of the SiC (silicon carbide) fibers to decorate the surfaces with “fuzzy fiber” coatings which provide better interface interactions between the fiber and the matrix through “velcro-like” interactions. The optimization of the growth process in terms of temperature, growth time, and catalyst decoration was evaluated. The effect of these parameters was shown by scanning electron microscopy (SEM), transmission electron microscopy (TEM), electron energy loss spectroscopy (EELS), RAMAN spectroscopy, and Fourier-Transform Infrared spectroscopy (FTIR). Following the decoration of the SiC fibers, we have analyzed the mechanical properties of the as-decorated fibers from two perspectives. First, we have used a universal testing machine (UTM) and x-ray diffraction (XRD) to show the effect of temperature and BNNT decoration on the tensile strength of the fibers followed by a micro-droplet pull out test to calculate IFSS of the as-decorated fibers inside the epoxy matrix. The research was completed with collaboration with Ayşemin Top, Fırat Turgut, Beyza Bozalı, Dr. Nuri Solak and Dr. Hülya Cebeci of İstanbul Technical University (ITU) and Aerospace Research Center (ITU-ARC) as well as Dr. Elif Özden-Yenigün of Royal College of Art.

Chapter 2 titled “h-BN Nano/microstructure Reinforced Noryl Composites as Insulating Dielectric Materials” is a comparative study evaluating BN-MF, BN nanoparticles (BN-NP), BN microparticles (BN-MP) as an effective filler material for the fabrication of dielectric composites with low dielectric constant and dielectric loss. First, the synthesis and the temperature optimization of the BN-MFs are discussed with results derived from SEM, TEM, EELS, RAMAN, and FTIR. Followed by the fabrication of polymer matrix composites with varying amounts of BN filler materials which are then evaluated in terms of their glass transition temperature (T_g) calculated through differential scanning calorimetry (DSC) and dynamic mechanical analysis (DMA) characterization methods. The composites’ dielectric properties are then compared to the neat polymer via split post dielectric resonator (SPDR). The research was carried out in collaboration with Dr. Merve Senem Seven, Dr. Yusuf Menceloglu, Dr. Serkan Ünal, Dr. Bekir Dizman of Sabancı

University and Dilan Kaya and Dr. Hülya Cebeci of Istanbul Technical University and Aerospace Research Center.

Chapter 3 titled “Low-Temperature Synthesis of Boron Nitride Nanotubes from Boron Minerals with the Assistance of Sulfur-Based Molecules” proposes a synthesis method for BNNTs which can feasibly be modified to large-scale synthesis. The main goal of this chapter can be divided into three distinctive parts. (1) Synthesis of BNNTs from cheap and environmentally friendly boron minerals colemanite, ulexite, and Etidot-67. (2) Evaluation of different sulfur-containing compounds thiophene, L-methionine, and L-cystine to lower the synthesis temperature of the BNNT synthesis, and (3) surface functionalization of BNNTs with polytetrafluoroethylene (PTFE) via closed-batch infiltration chemical vapor deposition (CB-iCVD) technique. The results of the experimental work were discussed with the help of TEM, EELS, RAMAN, and FTIR. During this research, we have collaborated with Dr. Omid Mohammad-Moradi and Dr. Gözde İnce.

Following this introductory chapter, the literature reviews for each chapter are discussed within that chapter. The complete flow diagram of this thesis can be found below (Figure 1.1). We sincerely hope that the research presented here can advance the boron nitride research and literature and open new possibilities for this extraordinary material.

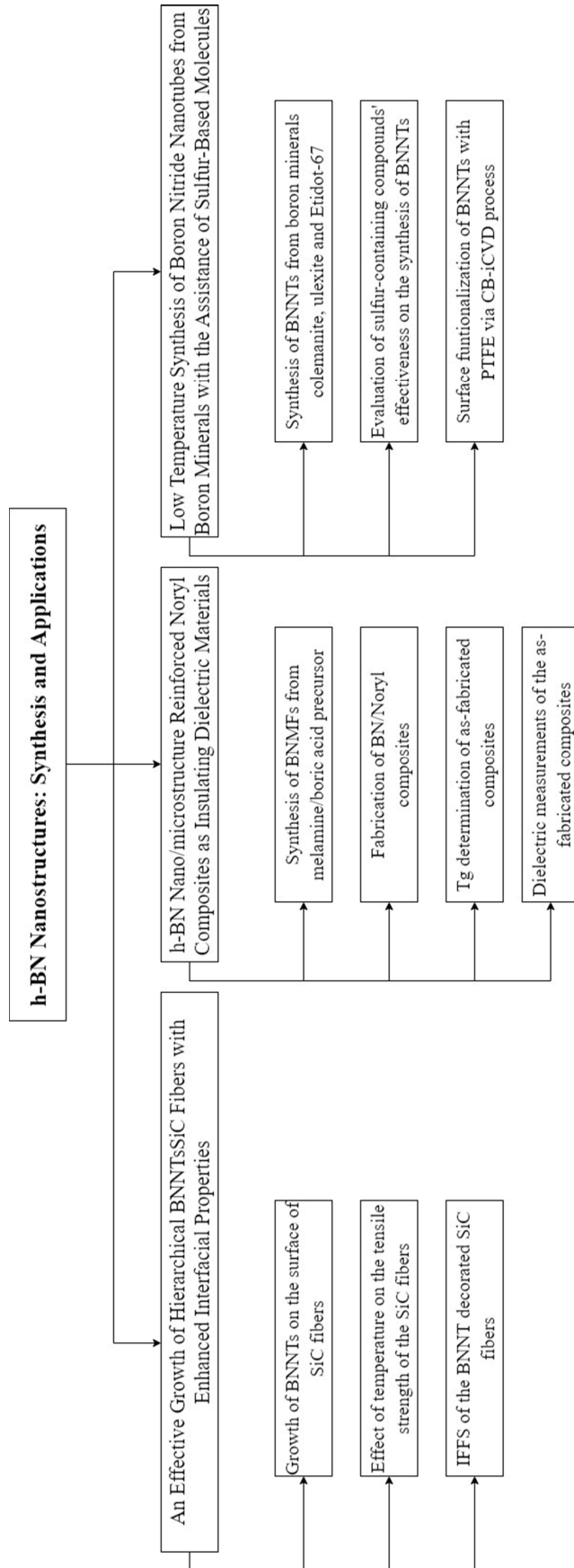


Figure 1.1 Flow Chart of the research carried out within this thesis.

Chapter 2 AN EFFECTIVE GROWTH OF HIERARCHICAL BNNTs/SiC FIBERS WITH ENHANCED INTERFACIAL PROPERTIES

2.1 Introduction

Ceramic matrix composites (CMCs) are the most preferred materials in high-temperature applications such as; aerospace [1-3], automotive [4], gas turbines [4], and in similar applications where high thermal and oxidative stability, wear resistance, low density and high strength properties of the CMCs can be utilized [5]. However, two drawbacks of these materials exist; (1) Fabrication of these materials are often carried out in high temperatures meaning the reinforcements that are planned to be used in these materials also should be stable in high temperature. (2) Due to high-temperature fabrication processes that are employed, the thermal expansion coefficient of the matrix material and the reinforcement should be close enough to prevent any crack formation during the production and subsequent cooling [6]. Above mentioned problems not only limit the research and applications into CMCs but also hinder it from reaching their true potential.

Continuous SiC fiber (SiC_f) reinforced SiC composites are lightweight thermostructural composites mainly used in hot sections of the gas turbine engines for turbomachinery applications [7] and as a structural material for fusion power reactors [8]. SiC fibers exhibit high thermal stability, high oxidation resistance, low activity under irradiation conditions, and superior mechanical properties [9], and using these fibers as both

reinforcement material and matrix material solves the thermal stability and thermal expansion coefficient difference problems explained before.

SiC fibers were first prepared by the spun polymer precursor in 1975 by Yajima *et al.* [10]. The general properties of β -SiC fibers can be seen in Table 2-1. Following the invention of the SiC fibers by Prof. Yajima, Nippon Carbon Co. Ltd. successfully manufactured multi filament continuous SiC fiber called Nicalon and its ultra-high temperature derivative Hi-Nicalon [11]. However, due to their high β -SiC microcrystals and excess carbon content, these fibers suffered from relatively low creep resistance and oxidation stability. To address these drawbacks a new type of SiC fiber was designed with stoichiometric composition and high crystallinity that can allow improved properties at elevated temperatures called Hi-Nicalon S [12].

Table 2-1 Properties of β -SiC phase which forms the SiC fiber [13].

Property	Value
Crystallography	Cubic (fcc), $a = 0.4360$ nm
Melting Point	2830 °C (at 3.55 MPa (35 atmospheres), decomposes at 101 kPa (atmospheric pressure))
Density	3.21 gcm ⁻³
Hardness	3100 – 3500 (Knoop)
Coefficient of thermal expansion	3.8×10^{-6} °C ⁻¹ (200 °C) 5.8×10^{-6} °C ⁻¹ (1000 °C)
Thermal Conductivity	0.25 W/cm°C (200 °C) 0.15 W/cm°C (1000°C)
Young Modulus	450 GPa (RT), 420 GPa (1000 °C)
Poissons Ratio	0.17 (RT), 0.18 (1000 °C)
Fracture Toughness, K_{1C}	3 – 4.5 MNm ^{-3/2}

Non-oxide CMC composites fabricated through the use of SiC fibers as both matrix and reinforcement has gained interest due to their high operation temperatures (up to 1500 °C) in areas such as gas turbines, fusion reactors, high-temperature furnaces, and aerospace engines where elevated temperature properties can be utilized [14]. Although SiC fibers exhibit brittle behavior, SiC fiber-reinforced SiC ceramics show pseudo-ductile characteristics which makes them highly sought after as structural materials [15].

SiC_f/SiC composites to be used in fusion reactors as structural materials have shown promising potential. A study of the SiC_f/SiC composites in Tokamak fusion reactors done

by Jones *et al.* [16] highlighted the strengths of these composites where it showed adequate thermal shock and low-cycle fatigue properties coupled with radiation stability even in temperatures as high as 800 °C to 1000 °C. In their paper, Katoh *et al.* [17] reviewed the current status of SiC_f/SiC composites for fusion applications and claimed that SiC_f/SiC composites have moved on from “stage of potential viability and proof of principle to system demonstration”. They also found that SiC_f/SiC composites showed no strength degradation under irradiation and preserved their creep resistance in elevated temperatures.

Corman *et al.* [18] from General Electric developed SiC_f/SiC composites via melt infiltration technique and reported optimal mechanical properties even at a relatively low loading of 20-25 %. Furthermore, their composites showed sufficient thermal stability in the air atmosphere which is a crucial parameter in gas turbine applications. Christin *et al.* outlined the requirements of CMCs that can be used in gas turbine engines as, preservation of mechanical properties above 1100 °C and lifetime of 100 hours in harsh conditions such as high-stress levels, moisture, oxygen, and jet fuel [19]. They claimed that SiC_f/SiC composite can be used in the exhaust and reheat sections of the engines and outlined them in their article.

The final mechanical properties of the fiber-reinforced composites highly depend on the interactions on the interface between the fiber reinforcement and the matrix. It is widely known that brittle ceramic materials suffer from low toughness and SiC fibers are no exception to this phenomenon [20]. Toughness can be defined as energy that can be absorbed by the material without suffering any catastrophic failure. In fiber-reinforced ceramic composites toughness can be achieved by “fiber debonding” and/or “fiber pull-out” mechanism which allows crack bridging (Figure 2.1).

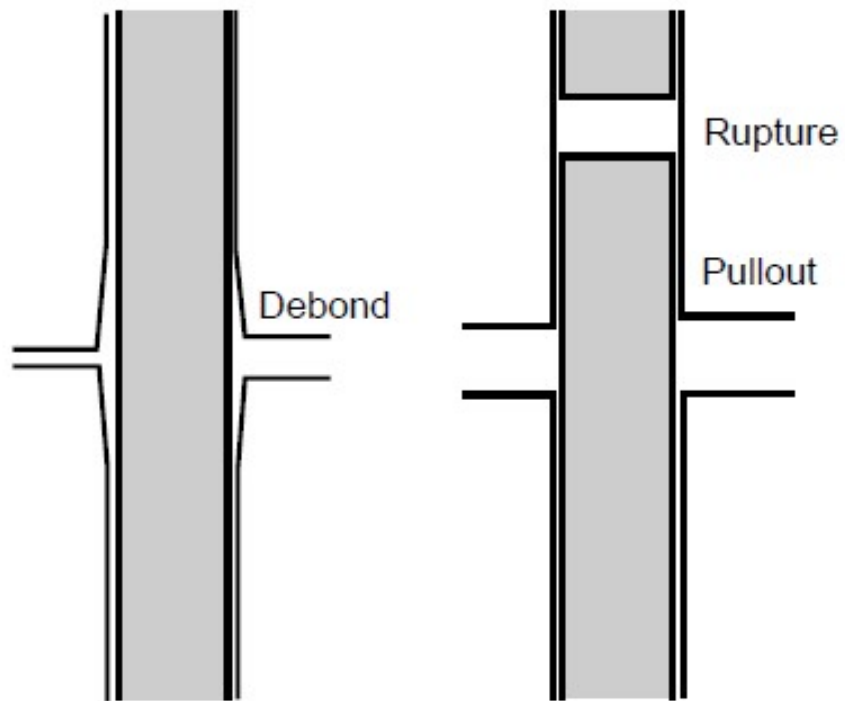


Figure 2.1 Schematic of fiber debonding and fiber pullout mechanisms observed in fiber-reinforced composites [21].

In essence, the crack tip widens due to debonding of the fiber from the matrix, decreasing the stress intensity at the crack tip and preventing fiber failure which can lead to catastrophic failure in the ceramic. As the crack widens, energy continues to be absorbed due to consecutive debonding of the fibers which creates slip resistances. This resistance further absorbs the energy and diminishes the stress at the crack tip. Ultimately, fibers fail and produce a crack-bridging ahead of the advancing crack tip (Figure 2.2) [21].

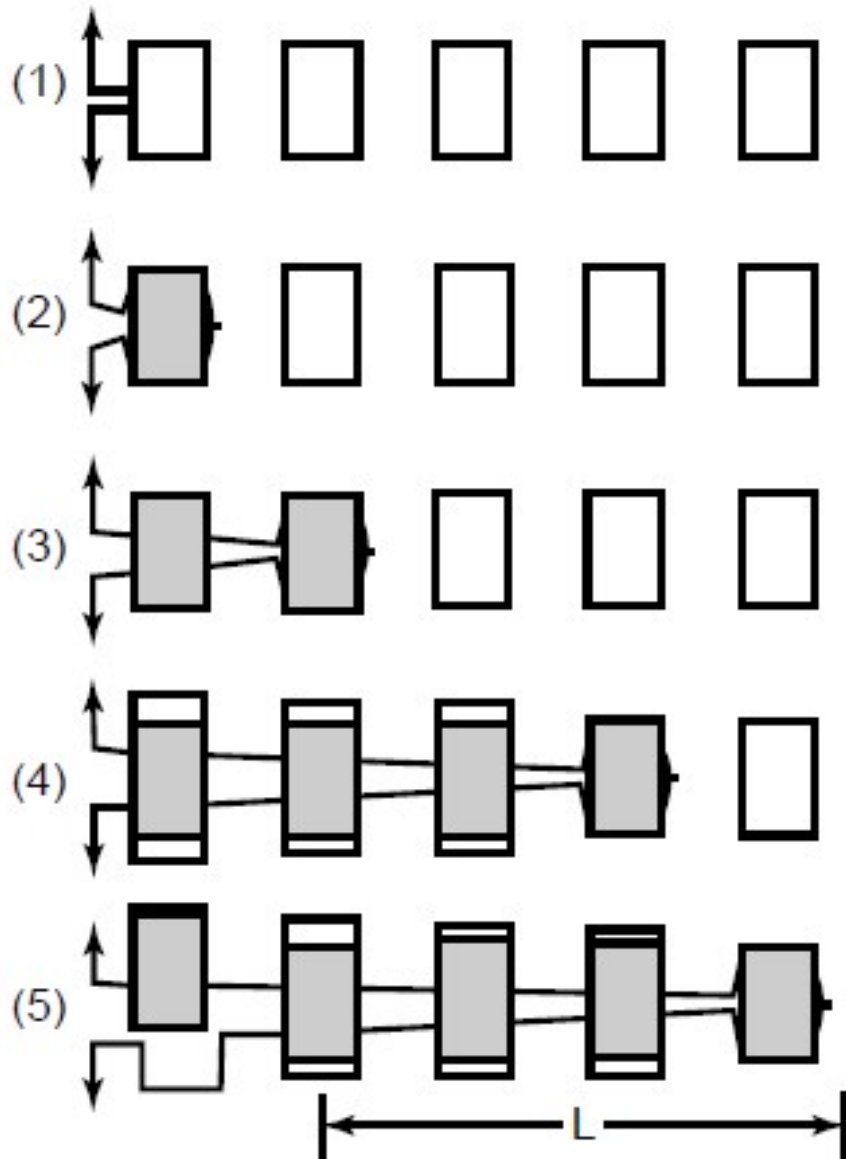


Figure 2.2 Crack bridging sequence observed in fiber-reinforced composites. (1) Crack deflection, (2) fiber debonding, (3) fiber pull-out, (4) growth of bridging, (5) steady-state bridging zone [21].

When the above-mentioned mechanism occurs, sliding resistance, τ , dictates the load transfer from the matrix to fiber. Large τ promotes better load transfer thus, decaying the stress acting on the fiber as it gets further away from the matrix crack plane [22]. However, for debonding to occur (rather than fiber failure) fracture energy of the interface must be lower than the fracture energy of the fiber. In conclusion, too weak nor too strong interface strength is desired for the ceramic composites to be used in applications. If the interfacial strength of the composite is too low, load transfer between matrix and the fiber

is insufficient to achieve desired mechanical properties whereas a strong interface can result in brittle characteristics for the composite due to fiber failure before any debonding or pull-out of the fibers [23]. Effects of the strength of the fiber-matrix interface were eloquently illustrated by Prof. Dr. King [24] (Figure 2.3) by using a simple stress-strain graphic. As can be seen from the graphic as well, if the interface strength of the composite is too high, it fails similar to brittle material with low toughness and without any debonding behavior. However, if the interfacial strength is weaker, energy is dissipated due to fiber debonding and fiber pull-out that enhances the fracture toughness of the composite drastically.

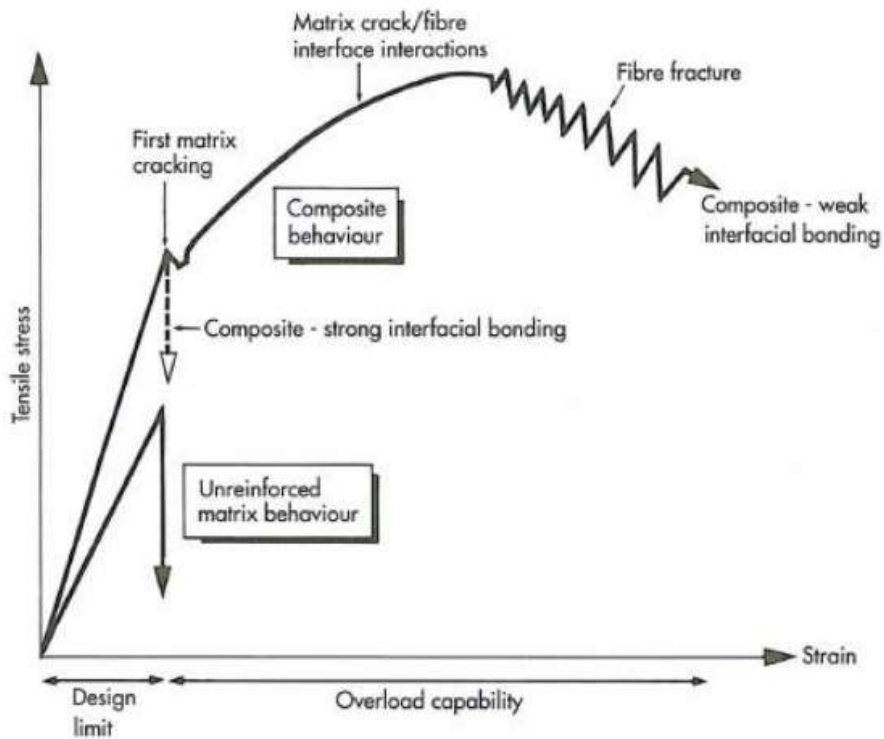


Figure 2.3 Stress-strain curve for the continuous fiber-reinforced composite. Although not depicted, too weak interface strength would have resulted in lower mechanical properties than of optimum interface strength composite due to diminishing of the load transfer capabilities of the composite [24].

Another major setback in non-oxide CMCs is the degradation due to oxidation in elevated temperatures and an oxide-rich environment [25]. Under loading conditions, a matrix that

prevents oxygen from reaching the matrix forms cracks in it which allow oxygen to penetrate inside the matrix fiber interface. Under the oxygen atmosphere, the interface and the fiber degrade to a point where debonding characteristics of the fiber change dramatically. This degradation causes composite to lose its desired mechanical properties such as toughness, strength, and viability in elevated temperatures [26].

In the literature, fiber coatings have been utilized for the creation of a weak interface between the fiber and the matrix to promote higher toughness in the ceramic [27-37]. These coatings are generally used to weaken the interface interaction between the fiber and matrix, thus promoting more fiber debonding and pullout, resulting in increased toughness for the ceramic. Furthermore, these coatings, especially BN coatings which will be discussed later, provide much-needed oxidation resistance to the fiber thus enabling them to be used in elevated temperatures at their full potential.

Pyrolytic carbon (PyC) is one of the most commonly used coating materials in SiC_f/SiC composites due to its high melting point, thermal conductivity, corrosion resistance, thermal stability, and novel processing [38]. Yang *et al.* [39] demonstrated the flexural properties of 2D plain-woven SiC_f/SiC composites with single and multilayered PyC coatings with respect to thickness and architecture. They used the chemical vapor infiltration (CVI) technique to coat their composites in varying thicknesses/architectures and used a three-point bending test for flexural properties and SEM for the investigation of the fiber pull-out and debonding behavior. Their results showed that, at the optimum coating thickness of the PyC, both proportional limit stress (PLS) and ultimate flexural strength (UFS) increased relative to non-coated fibers (Figure 2.4). Additionally, they showed that fiber debonding and crack deflection were present after the PyC coating for both composites, single layer, and multi-layer. However, multilayer coatings allowed the arresting of the crack between interlayers whereas single layer coatings only showed crack arresting at the fiber-matrix interface. Likewise, Cao *et al.* [40] also reported the effect of PyC coatings on the SiC fibers in their research. They claimed that composite experienced enhanced flexural strength when coated with a PyC layer depending on the thickness of the coating. Furthermore, the fracture toughness of their composites reached $25 \text{ MPa.m}^{1/2}$ when PyC thickness was 450 nm compared to $8.4 \text{ MPa.m}^{1/2}$ for 50 nm coating thickness. However, PyC coatings exhibit oxidation even at low temperatures which limits their use in elevated temperatures such as gas turbines and engine parts [41].

Although the above-mentioned studies confirm the mechanical enhancement of the composites with PyC coatings, all of their mechanical testings were done at room temperature which is an unrealistic environment for their intended applications.

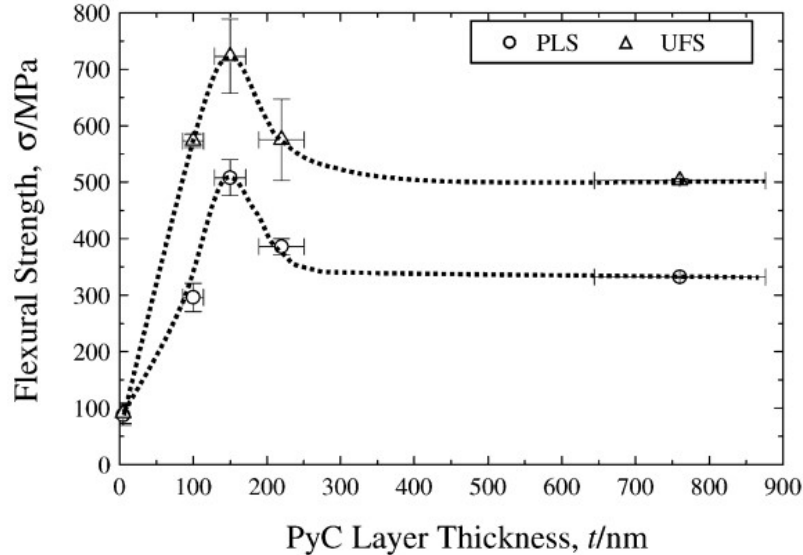


Figure 2.4 Flexural Strength vs PyC layer thickness plot for the single-layered PyC coatings on SiC_f/SiC composites clearly showing the enhancement of the mechanical properties of the composite by PyC coating. 150nm coating thickness appears to have optimum mechanical properties for the composite [39].

One of the alternative coating materials suggested to replace PyC due to their low thermal stability is ZrO_2 . Weak interface interaction stems from the phase transition of the ZrO_2 tetragonal phase to the monoclinic phase causing volume change in the structure [32]. Li *et al.* [42] analyzed the tensile and stress-rupture behavior of SiC_f/SiC composites that are coated with ZrO_2 interphase via chemical vapor deposition (CVD). They concluded that weak bonding resulted due to continuous coverage of the zirconia phase throughout the fiber and phase transition of the zirconia from tetragonal to monoclinic phase. Their interphase coating provided much-needed protection from the processing degradation and weak interface toughening of the SiC composite as well as mechanical strength retaining at elevated temperatures. Lee *et al.* [43] on the other hand, designed a multilayer coating system where they sandwiched ZrO_2 layer in between the amorphous SiO_2 layer to achieve crack deflection and fiber pullout within the sandwich coating. As can be seen from Figure 2.5 (reproduced from their article) they successfully coated the fiber with amorphous SiO_2 and zirconia phases (unintentional zirconia phase was also observed

which they argue caused by the residues left on the CVD system they are using) and these micro composites showed similar composite behavior even after the oxidation treatment at 960 °C for 1 hour. It did however lose some of its load capacity after the treatment.

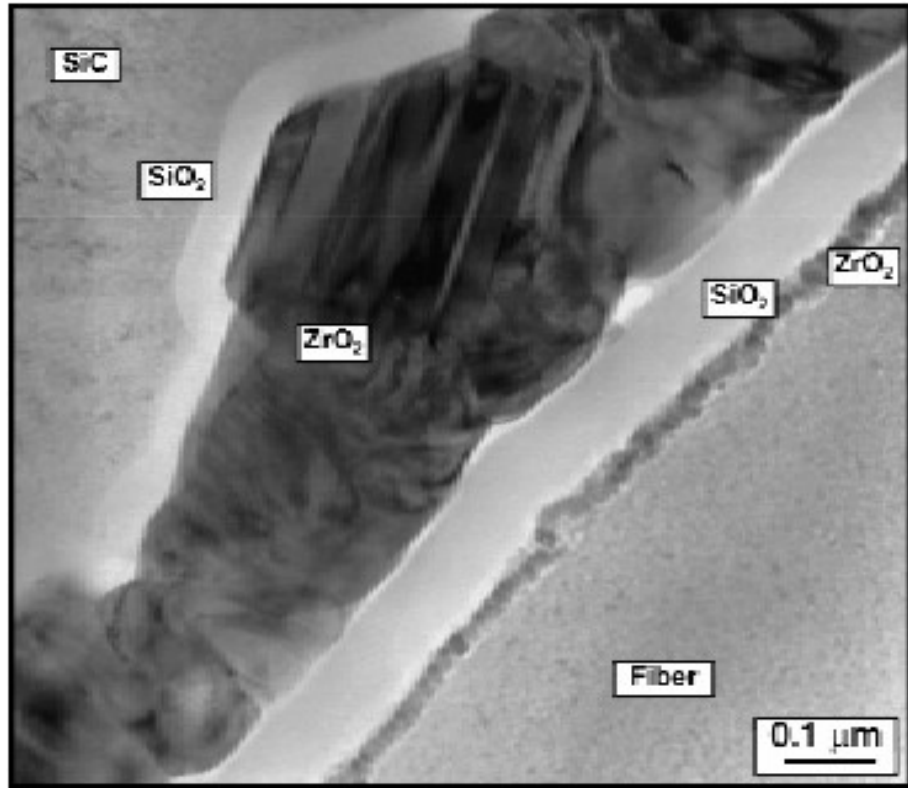


Figure 2.5 TEM image of the SiC fiber micro composite prepared by Lee *et al.* [43]
Crack deflection and fiber pull out happened within the zirconia phased shown above in dark contrast.

Hexagonal Boron Nitride coatings have been used extensively in SiC_f/SiC composites as interphase materials due to their extraordinary oxidation protection. In summary, in a moisture-free environment boron oxide reacts with the silica from borosilicate, filling any voids between the fiber and matrix and preventing oxygen from penetrating to the fiber surface or the interface [44]. However, if the moisture is introduced into the atmosphere, the BN phase reacts with the moisture to create boron hydroxides which readily evaporates and leaves behind voids. This effect is especially dangerous at temperatures range 600 °C to 800 °C where a protective SiO₂ layer is unable to form. To overcome these challenges, a multilayer BN interphase has been proposed [45]. The main idea behind the multilayer architecture comes from the notion that, if the debonding and

sliding happen further away from the fiber, unwanted B species can be avoided near the fiber, and as a result fiber will not experience brittle behavior (Figure 2.6) [36].

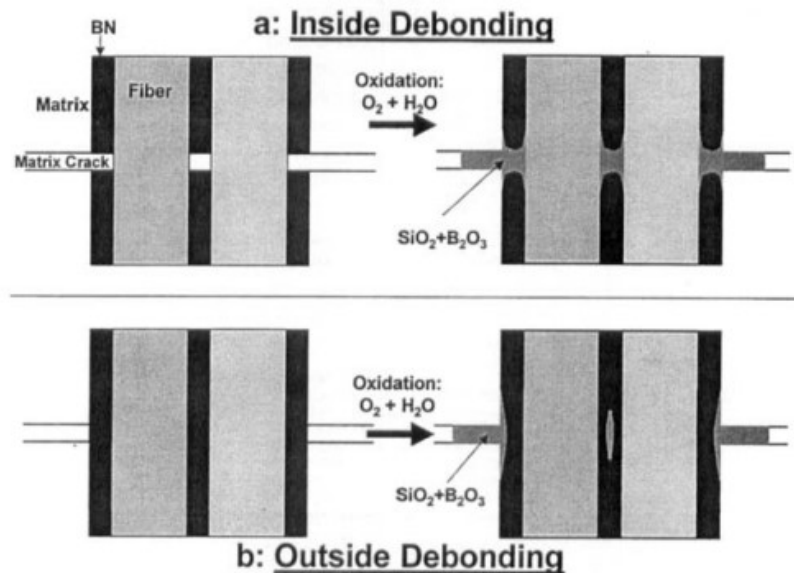


Figure 2.6 Schematic of inside debonding (i.e. where debonding happens between the fiber and the interface) and outside debonding (i.e. where debonding happens between the matrix and BN interphase) [36].

A comprehensive analysis of this design idea was done by Morscher *et al.* [36] and showed improvement in the mechanical properties (Figure 2.7) as well as oxidation resistance in the intermediate temperature range. They postulated that these improvements were the result of better adhesion between BN interphase material and the fiber. Thus, fibers were protected from the oxidizing environment more effectively. However, due to process conditions required for the outside debonding is challenging for the SiC fibers and can be more suitable to other ceramic composites.

Specimen-location of debonding	epcm ¹ /No. plies	f	E (GPa)	σ_{ult} (MPa)	ϵ_{ult} (%)	τ (MPa)	
						Estimated from σ/ϵ curve	Measured from push-in test
HNS-outside	7.1/8	0.17	200	352	0.46	—	—
HNS-inside	7.1/8	0.18	240	311	0.38	—	—
SYL-outside	7.1/6	0.13	224	224	0.27	37	—
SYL-outside	5.0/8	0.15	219	297	0.43	25	—
SYL-mixed	7.9/8	0.19	246	353	0.33	45	26
SYL-inside	6.3/8	0.19	246	397	0.36	—	—
SYL-inside	8.7/8	0.2	265	389	0.3	65	64
SYL-inside	7.1/8	0.17	270	310	0.31	63	70
SYL-iBN outside	8.7/8	0.2	216	456	0.5	18	7
SYL-iBN outside	7.1/8	0.17	220	395	0.49	11	6
SYL-iBN mixed	7.9/8	0.19	228	>476	0.51	43	31
SYL-iBN inside	8.7/8	0.2	277	404	0.31	73	83
SYL-iBN inside	7.9/8	0.2	248	502	0.42	—	—
SYL-iBN inside	5.0/8	0.12	279	284	0.21	63	—

Figure 2.7 Mechanical properties of the SiC/SiC composites tested during the research done by Morscher and his group [36].

Above mentioned coatings were primarily designed for the introduction of a weak interface between the fibers and matrix to enhance the toughness of the SiC_f/SiC composites. Lately, a different approach has started to gain interest [30, 46-48]. Strong interface interactions allow cracks to be arrested within the coating into short and branched cracks. These multitrack increases the toughness of the composites via shear number since more cracks can absorb more energy resulting in higher toughness for the composite. Furthermore, improved load transfer leads to improved strength for the composite [46]. Overall, the strength, toughness, lifetime, and creep resistance of the composites can be enhanced by the introduction of strong interfaces [47]. Rebillet *et al.* [46] showed that the load necessary to initiate fiber pull-out is 4 times higher for the strong interface interaction fibers and interfacial shear strength is 10 times higher than weak interface SiC/SiC composites. Their results showed that strongly bonded interfaces show not only stronger mechanical properties but are expected to have a higher fatigue life compared to their weakly bonded counterparts. Pasquier *et al.* [49] also argued the same points discussed by Rebillet *et al.* and reported that when the strongly bonded interfaces are present, fatigue lifetime and behavior greatly improve for the SiC composites even in elevated temperatures in an oxidizing environment.

Lately, an area of particular focus has been on growing carbon nanotubes (CNTs) onto the surface of micron-sized fibers with the potential to expand the performance and functionality of fiber-reinforced composites. To date, Garcia *et al.* [50] have synthesized aligned CNTs onto the surface of alumina fibers in fuzzy form and infused epoxy matrix on the fibers via a simple layup procedure. Their architecture showed a 69 % increase in

the interlaminar shear strength (ILSS) in addition to better electrical conductivity. Wicks *et al.* [51] also studied the effect of fuzzy fiber CNTs on the fiber-reinforced polymer matrix finding that the fracture toughness of the composite was enhanced by 76 %, as well as achieving a minor increase in critical strength and ultimate strength in tension-bearing tests – 9 % and 5 % respectively. Additionally, CNTs have been utilized as reinforcements in SiC_f/SiC composites to increase fracture toughness and flexural properties [52], as an interphase material [52-56] to achieve electromagnetic shielding [57] and to enhance thermal conductivity [58]. Although all of these mechanical properties and thermal conductivity were noticeably enhanced by CNTs, the thermo-oxidative stability of CNTs was insufficient, making them unsuitable for high-temperature applications due to their low thermal stability (approximately 400 °C – 600 °C) in the air [59]. To satisfy the high thermal stability requirement in CMCs, Hart *et al.* [60] suggested the growth of Velcro-inspired SiC nanowire and nanotube coating with “fuzzy fiber” architecture. They grew SiC nanostructures on the surface of SiC_f by using CNTs as a template and enhanced Young’s modulus of the composite by 47 %, with increasing thermal resistance under an oxygen atmosphere. However, the growth of SiC nanostructures on the surface of the SiC_f requires a two-step CVD process, starting from growing CNTs and followed by their conversion to SiC tubes.

BNNTs satisfy the requirements of CMCs in a similar fashion to CNTs in the F/M interface through a high specific surface area and very high thermal stability, high corrosion resistivity, and excellent mechanical properties at elevated temperatures [61-63]. Hurst *et al.* [64] showed that it is possible to decorate fiber surfaces with BNNTs, and achieved a 2.5 – 3 times higher tensile strength for the BNNTs/SiC_f composite coupons prepared by the thermal CVD method; however, they did not evaluate their composites ILSS, which is crucial for such hybrid approach. Similarly, Zhu *et al.* [65] prepared SiC_f/BNNTs-SiC architectures by growing BNNTs onto SiC_f in-situ via ball milling, and while 87.8 % of the SiC_f/SiC strength was retained at elevated temperature, SiC_f/BNNTs-SiC composites showed 94.7 % strength retention. Moreover, no decrease in fracture toughness was reported. Also, there have been studies where BNNTs were used as interface materials in metal matrix composites (MMCs). Nautiyal *et al.* [66] fabricated layered Al-BNNT-Al MMCs using ultra-long BNNTs in which they showed a 400 % tensile strength increase compared to neat Al. The results were attributed to an effective load transfer of directionally aligned BNNTs and strong interfacial interaction

between the Al matrix and BNNTs. The application of these fuzzy architectures as BNNTs/SiC_f may be used in next-generation CMCs for advanced applications with an industrially compatible approach as similar to BN coatings applied onto SiC_f to prevent from oxidative environments.

The aim of this research was the growth of fuzzy fiber BNNTs on the surface of the SiC fibers to produce hierarchical BNNT/SiC_f structures. This fuzzy fiber coating can improve the strength of the interface interactions between fiber and the matrix via the “hook and loop” mechanism and increase the specific surface area of the fibers. This improvement was investigated by calculating the IFSS of the individual fibers via a single fiber micro-bonding test. The growth of the BNNTs was achieved using growth vapor trapping boron oxide chemical vapor deposition technique at 1200 °C using elemental amorphous boron nano powder as boron precursor and Fe₂O₃ and MgO as catalyst nano powders. Ammonia gas was used as a nitrogen source for the growth of the BNNTs. The effect of process temperature and the time with respect to surface coverage and BNNT quality were investigated using scanning electron microscopy. SiC fiber surfaces were decorated by a simple dip-coating method to create Mg and Fe nucleation sites and the effect of these nucleation sites was characterized by SEM as well. Although the GVT-BOCVD method utilizes relatively lower reaction temperatures compared to other techniques reported in the literature, the degradation effect on the SiC fibers due to growth of the BNNTs was also investigated by comparing the tensile strength of the fibers after and before BNNT growth via universal testing machine. The complete experimental flow of this research can be seen in Figure 2.8.

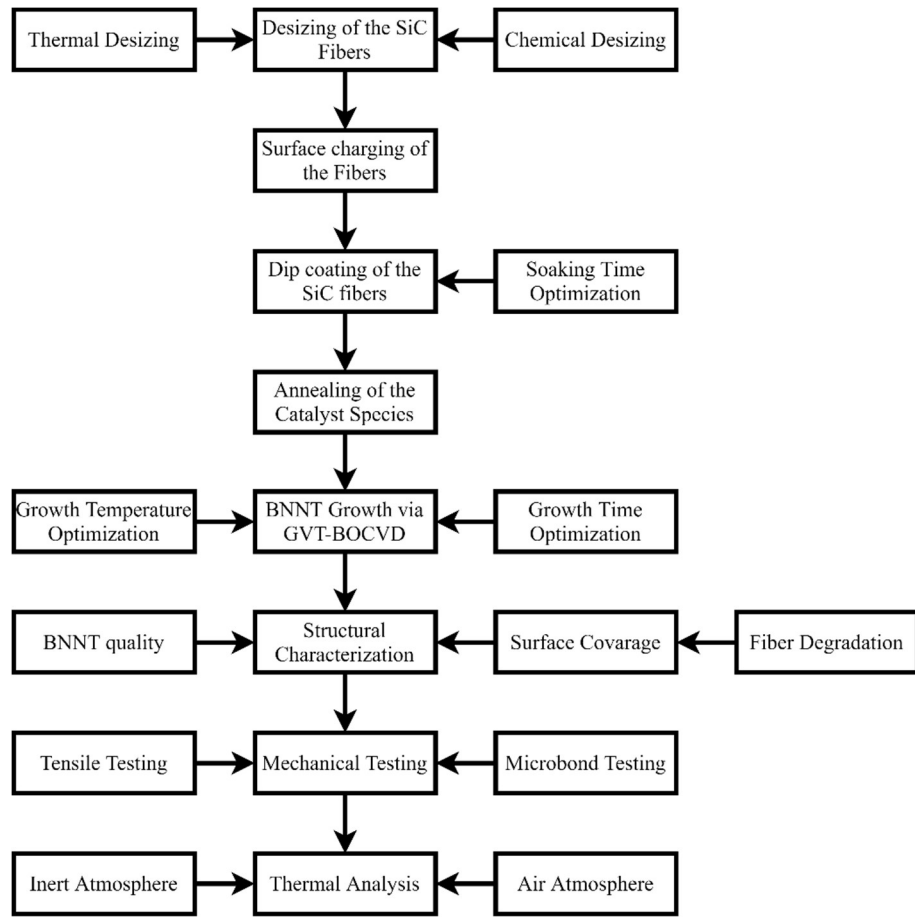


Figure 2.8 Flow chart of the production of BNNT/SiC_f hierarchical structures research.

2.2 Experimental

2.2.1 Techniques and Methods Used

For the growth of “Fuzzy fiber” BNNTs on the surface of SiC fibers below equipment was used;

PFT 15/50/450 Protherm tube furnace, TFF 55035C-1 Thermo Fisher Scientific split furnace, 0-1 slpm Alicat flowmeter, 0-500 sccm Alicat flowmeter with corrosive gas

resistance, 0-500 sccm Aalborg flowmeter with hydrogen gas calibration, 0-5 slpm Aalborg flowmeter with argon gas calibration, 2" diameter, 1 meter long alumina tube, 36 mm inner diameter, 1 meter long one-end closed quartz test tube, 1" diameter, 500 mm long quartz tube, alumina boats with various sizes, quartz substrate holder, 6" silicon wafer, Honeywell ammonia sensor, United ultrasonic bath, Ozone Systems Inc., Harric plasma, PDS-002 (230 V) plasma cleaner, Universal Tensile Machine (UTM) (Shimadzu).

For the desizing, catalyzing and growth of the BNNTs below chemicals were used;

Hi-Nicalon S type SiCf (Safran Herakles Company), PVZ nano Boron (Pavezum), Sigma Aldrich, iron (III) oxide powder, $< 5 \mu\text{m}$, $\geq 99 \%$, Sigma Aldrich, magnesium oxide, $\geq 99 \%$ trace metals basis, -325 mesh, Iron(III) acetylacetone ($>99.9 \%$ trace metal basis, Sigma Aldrich), magnesium acetylacetone (Aldrich^{CPR}, Sigma Aldrich), Ethanol (absolute for analysis EMSURE[®] ACS, ISO, Reag. Ph Eur, Sigma Aldrich).

2.2.2 Desizing of the Fibers

Hi-Nicalon S type SiC fibers were received in a tow form with 500 single fibers with a diameter of $17 \mu\text{m}$ present in the tow. As-received fibers are sized with a polymer coating in order to protect from outside effects and ease of handling that needs to be removed before any processing on them. Although sizing was known to be a polymer, the type of polymer is kept as a trade secret. To remove this sizing, two different approaches were tried.

The first approach is the removal of the polymer sizing with a common polymer-solvent DMF. SiC fiber tow with a 10 cm length (appropriate for the size of the alumina boat) was cut from the master tow and place inside a DMF solvent. The fibers were left inside the DMF solvent for 48 hours undisturbed to allow the dissolution of the polymer sizing. Afterward, de-sized fibers were washed with distilled water three times and placed into an oven at 60°C overnight for drying. SEM images of the fibers were taken to confirm no degradation to fibers after the DMF treatment and FTIR analysis was performed to

verify the desizing process. A tensile test of the fibers was also used to investigate the effect of the desizing on the mechanical properties of the fibers.

Another method to get rid of polymer desizing is to take advantage of the low degradation temperature of the polymers. For this purpose, a 10 cm long fiber tow was placed on a quartz substrate and placed into a split furnace. Fibers were heated to 900 °C under constant argon flow to prevent oxidation of the excess carbon of the fibers. After allowing it to cool down to room temperature under an argon atmosphere, fibers were collected and prepared for the SEM, FTIR, and tensile testing characterization.

2.2.3 Surface Decoration of the SiC fibers via Dip-coating

Decoration of the SiC fibers with catalyst consists of three phases: (1) Surface charging of the fibers with plasma treatment, (2) dip-coating of the fibers inside a catalyst-ethanol solution, and (3) reduction of the catalyst particles under H atmosphere (Figure 2.9).

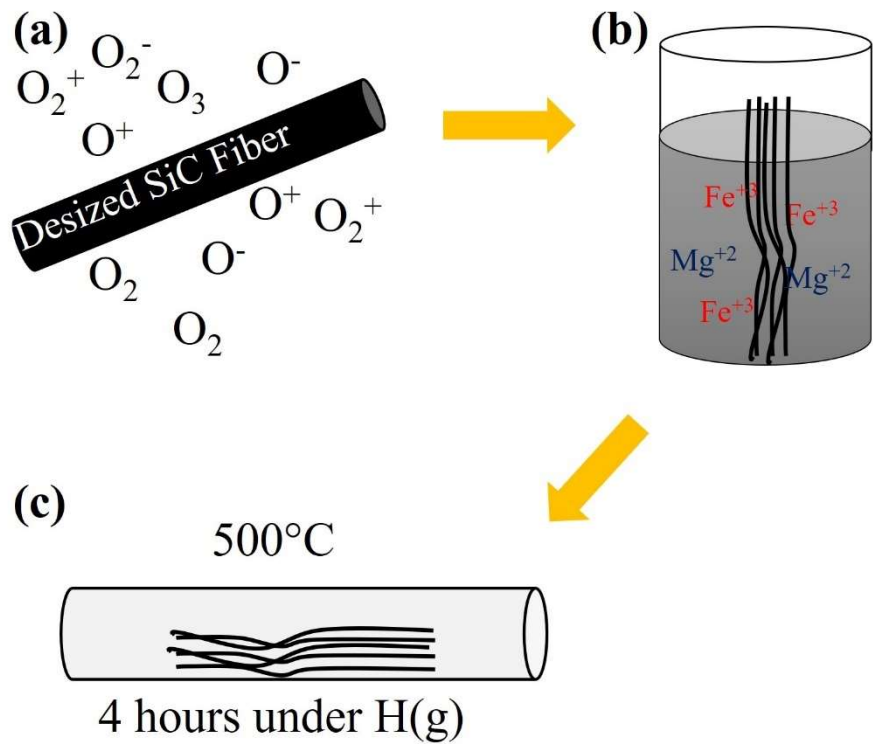


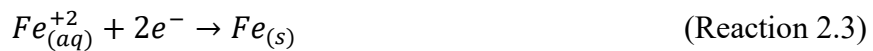
Figure 2.9 Schematic of the surface decoration. (a) Plasma treatment of the fiber surface, (b) dip coating of the fibers inside catalyst/ethanol solution and (c) Reduction of the catalyst particles under H₂ atmosphere

Surface decoration of the fibers starts with the oxygen plasma treatment of the fibers. This step allows fibers to have a clean and smooth surface where catalyst can absorb and negatively charge the fiber surface via oxygen bombardment that enhances the catalyst absorption on the surface of the fibers. However, as the plasma exposure time increases, fiber degradation and the surface roughness of the fibers also increase. To avoid this, plasma treatment was only applied for only 3 minutes. After plasma treatment, SEM images of the fibers were taken to the confirm cleanliness of the surface and preservation of the surface smoothness.

Following the plasma treatment, fibers were dipped into Fe and Mg catalyst containing ethanol solution. The catalyst solution was prepared by dissolving 0.375 g of iron (III) acetylacetone and 0.375 g of magnesium acetylacetone inside 20 mL ethanol (2.5:2.5 Fe(acac)₃:Mg(acac)₂ w/w %) and stirred with a magnetic stirrer at room temperature until a homogenous solution was achieved. SiC fibers were placed inside the catalyst solution and kept there for 15, 60, and 120 minutes to investigate the effect of residence time on

the absorption of the catalyst particles. Afterward, fibers were removed from the solution and placed into a vacuum oven at 60 °C for 30 minutes to eliminate any ethanol residues.

The final step of the surface decoration is the reduction of the catalyst Fe^{+3} and Mg^{+2} to activated Fe and Mg atoms. De-sized, plasma-treated and dip-coated fibers were placed into the hot zone of the split furnace and heated to 250 °C under an air atmosphere with a heating rate of 10 °C/min and held at that temperature for 60 minutes for the oxidation of the magnesium ions according to reaction 2.1. Following this stabilization step, the air atmosphere was replaced with the argon with a flow of 200 sccm, and the furnace was further heated to 500 °C with a 5 °C/min heating rate. When the 500 °C was reached, argon flow was decreased to 150 sccm, and 50 sccm of hydrogen flow was introduced to the system. At this temperature for 4 hours, iron ions were reduced under a hydrogen atmosphere according to reactions 2.2 and 2.3. After the completion of the reduction, the system was allowed to cool down to room temperature under an argon atmosphere.



2.2.4 Growth of “Fuzzy Fiber” BNNTs on the SiC_f Surfaces

Growth of BNNTs on the surfaces of the SiC fibers was achieved via the GVT-BOCVD method. This method is frequently employed in the growth of BNNTs as mentioned in the introduction chapter. The growth of the BNNTs relies on the vapor-liquid-solid (VLS) mechanism which several researchers claimed to be the primary BNNT growth mechanism [67-69]. Essentially, this method dictates that; BN growth vapors produced due to the reaction between boron oxides and ammonia diffuses into the catalyst droplets. When the supersaturation of the growth vapors is achieved, BNNTs start the grow out of the catalyst droplets. The theory of nucleation for the whiskers can also be adopted for the nanotube growth if the growth mechanism can be defined as VLS [70].

In the theory of nucleation, the probability of nucleation for a whisker (P_N) is given as a function of temperature (T), supersaturation ratio (α), and surface energy of the catalyst droplets (σ) (Eq. 2.1). According to the equation, we can see that P_N is proportional to $\exp\left(\frac{1}{T^2}\right)$ meaning that, as the growth temperature increases, the yield of the growth also increases. This corresponds well with the reported high-temperature growth of the BNNTs in the literature. The theory also shows that the surface energy of the catalysts used in the growth also plays a role in the probability of nucleation. Finally, and the backbone of the GVT-BOCVD growth of BNNTs, the supersaturation ratio of the growth vapors has a proportional relationship with the nucleation probability of the whiskers (BNNTs).

$$P_N = B \exp\left(-\frac{\pi\sigma^2}{k^2 T^2 \ln}\right) \quad (\text{Equation 2.1})$$

Supersaturation ratio can be written as p/p_0 where p is the partial pressure of the growth vapors and p_0 is the partial pressure of the condensed phase at equilibrium. If the partial pressure of the growth vapors can be increased, it increases the probability of the nucleation and directly increases the yield of the BNNT growth. The GVT-BOCVD system is achieved, by placing the reaction vessel (alumina boat) inside a one-end closed quartz test tube and covering the alumina boat with a Si wafer. As the reaction volume is decreased, partial pressure of the growth vapors is increased thus supersaturation ratio is increased leading to a higher probability of the nucleation for BNNTs.

For the growth of the BNNTs, SiC fibers with Fe and Mg decorated surfaces were placed on top of a Fe_2O_3 , MgO , and B powder mixture (2:1:1 w/w) inside an alumina boat. To prevent any contamination from the catalyst mixture, SiC fibers were fixated on top of the catalyst mixture without touching by clamping both ends of the fibers between two Si wafers at an elevated height. The prepared alumina boat was then placed inside a one-end closed test tube 60 in length, next to the close-end of the tube. The test tube was then placed in the hot zone of the furnace with care to ensure the boat's position on the furnace corresponded to the stable zone of the tube furnace. The tube furnace was sealed, and the ends of the flanges were cooled down by the water-cooling system. Ammonia gas used during the growth is highly dangerous to human life, so it was monitored closely with an ammonia sensor.

Typical growth run proceeds as follow. Catalyst mixture was mixed using vortex mixer with a weight ratio of 2:1:1 of B: Fe₂O₃: MgO. The prepared catalyst mixture was placed inside an alumina boat and spread evenly. Afterward, SiC fibers were placed as instructed previously. The furnace is first vacuumed until 0.5 mbar was reached and purged with argon gas for 10 minutes to clean the tube and get rid of any oxygen or other air gasses. Following the purge, the furnace was heated up to 1000 °C with a constant Ar flow (200 sccm) with a heating rate of 5 °C/min. When the desired temperature was reached, Ar flow was replaced with an ammonia flow with 200 sccm, and the system was heated to a growth temperature of 1200°C. The growth process continues for 60 minutes after which, ammonia flow was again replaced with argon flow and the furnace was allowed to cool to room temperature. When the room temperature is achieved, a quartz tube can be taken out of the furnace and the SiC fibers with BNNT grown on them were collected.

2.2.5 Preparation of SiC for Tensile Testing

Tensile testing of the SiC fibers was performed in order to investigate the effect of the BNNT growth on the mechanical properties of the SiC fibers. A total of 5 different samples were prepared and tested. As-received SiC fibers (T-1), chemically desized SiC fibers (T-2), desized SiC fibers heated to 1200 °C under an argon atmosphere (T-3), desized and catalyzed SiC fibers heated to 1200 °C under ammonia atmosphere (T-4) and SiC fibers with BNNT grown on them (T-5). Single fiber tensile test was done using Universal Tensile Machine (UTM) with 1 kN load cell (1mN sensitivity) equipped.

Handling of the fibers during the sample preparation was highly difficult due to their brittle nature. Each fiber tow was separated into individual fibers under a light microscope with the utmost care. After single fibers were prepared, they were mounted on a paperboard frame suited to 25 mm gauge length. Fibers were fixed onto the frame using quick-drying adhesive (Figure 2.10). Fiber samples were tested according to ASTM D3379 [71] standard under quasi-static tensile loading with a deformation rate of 0.5 mm/min.

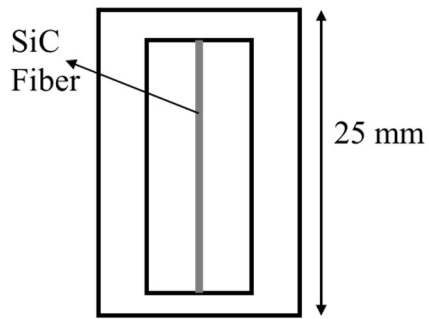


Figure 2.10 Schematic of the sample preparation for the tensile testing

Weibull analysis of the samples was also performed using the distribution function of strength (P_f) [72] (Equation 2.2), where shape (m) and scale parameters (σ_0) were expressed with linear regression method by arranging maximum breaking strength of each fiber sample from highest to lowest and calculating the failure probability of each sample with median rank estimator which converts equation 2.2 to equation 2.3 [73, 74].

$$P_f = 1 - \exp \left[- \left(\frac{\sigma}{\sigma_0} \right)^m \right] \quad (\text{Equation 2.2})$$

$$\ln(\ln \frac{1}{1-P_f}) = m \cdot \ln \sigma - m \cdot \ln(\sigma_0) \quad (\text{Equation 2.3})$$

2.2.6 Microbond Test Sample Preparation

For the calculation of IFSS of the fibers, several methods have been proposed by the literature such as nano-indentation [75], single fiber fragmentation [76], and fiber pull-out [77]. However, most of these tests require expensive and specialized equipment to be performed. Moreover, the brittle nature of the SiC fibers make it very challenging to use any fragmentation test on the SiC samples. To overcome these problems, a microbond test was selected. Microbond test has been utilized for several different types of fibers [78-80] and offers a simple, inexpensive, and direct method to calculate the IFSS of the fibers. Microbond test calculates the IFSS of the fibers via a simple equation, utilizing maximum load fiber can endure (F_{\max}), embedded fiber length (l_e) and fiber diameter (d_f) (Equation 2.4)

$$\tau_{IFSS} = \frac{F_{max}}{\pi d_f l_e} \quad (\text{Equation 2.4})$$

Results of this test can be interpreted via the average value of the calculated IFSS values or as the slope of the regression line intercepting origin in force vs. embedded area plot. Additionally, the calibration process for the microbond test should be carried out before any experiment due to extremely low maximum load values collected during the testing.

The single fiber microbond test was performed on the SiC fibers with and without BNNT grown on them to see the effect of the BNNTs on the IFSS of the fibers. A homemade fixture was prepared to fit into UTM (Figure 2.19 a) and epoxy droplets prepared via L160 - H160 epoxy resin system from Hexion with a mixing ratio of 4:1 (Resin: Hardener w/w), were dropped onto the surface of the fiber samples by hand-held syringe. Each sample droplet was cured for 24 hours at ambient temperature (Figure 2.19 a).

Calibration of the microbond test setup was carried out to investigate the precision of the UTM since the force readings during the microbond test showed smaller values than the recommended resolution of the UTM machine. Six weights (1 g to 50 g) were weighed using a highly sensitive analytical balance and their true weights were noted. Afterward, these weights were loaded onto UTM and five sets of tests were performed. The calibration results can be seen in Table 2-2

Table 2-2 The measured weights by analytical balance and by UTM

Weight no	Weight (N) (analytical balance)	Weight in N (UTM)
1	0.00867 (2.7×10^{-6})	0.023 (0.001)
2	0.01977 (4.0×10^{-6})	0.380 (0.002)
3	0.04912 (3.9×10^{-6})	0.065 (0.002)
4	0.09814 (3.7×10^{-6})	0.114 (0.001)
5	0.19615 (3.8×10^{-6})	0.212 (0.001)
6	0.49037 (5.4×10^{-6})	0.504 (0.001)

After the calibration, a trendline was fitted to a plot of the collected data with an R-square value of 0.99996 (Figure 2.11).

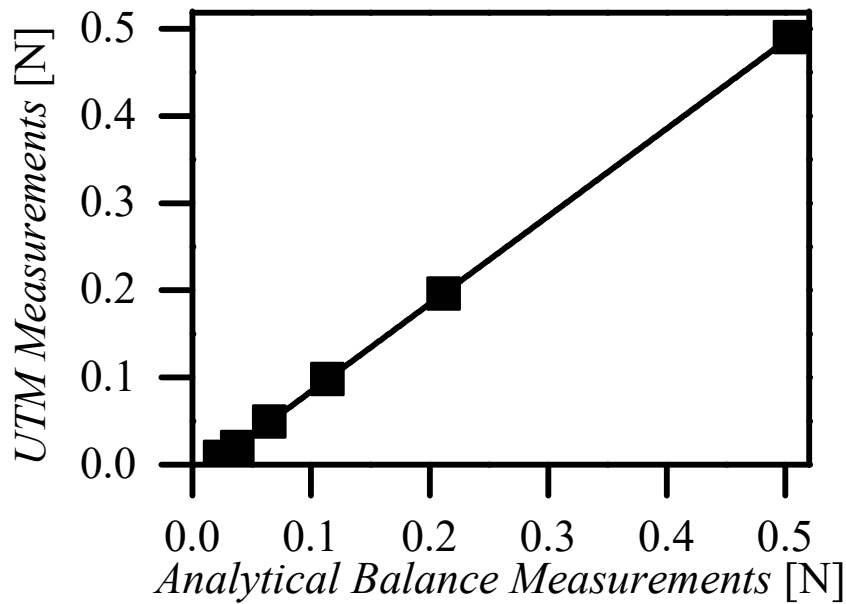


Figure 2.11 Plot of the weight of the samples measured by the UTM vs measured by the analytical balance with a fitted trendline.

Although, UTM data and analytical balance data showed a good correlation, offset between the measurements were also observed (-0.0167 with a standard error of 0.00074). Using the function outlined in Table 2-3, we have corrected the measured UTM data during the microbond testing.

Table 2-3 Equation of fitted trendline

Equation of function	$y = ax + b$
Slope (a)	1.00545
Intercept (b)	-0.01657
R-Square	0.99996

2.3 Results and Discussion

2.3.1 Techniques and Methods Used

The morphology of as-received SiC_f and BNNTs/ SiC_f were investigated by Scanning Electron Microscopy (SEM) (A FEI-Qanta FEG250, USA) and Ultra High-Resolution Transmission Electron Microscopy (Jeolden JEM-200CFEG UHR-TEM CS corrected equipped with Garanti Quantum GIF). Structural characterization of BNNTs was attained using RAMAN spectroscopy (Renishaw inVia Reflex Raman Microscopy and Spectrometer (532 nm laser unit)). The average diameter of the nanotubes was determined by measuring the diameters of 100 different BNNTs on the SEM images of each sample, using ImageJ software. X-Ray Diffraction (XRD) (A Bruker TM D8, Cu $\text{K}\alpha$, 1.542\AA) was performed in order to understand the crystal structure of SiC_f and BNNTs.

2.3.2 BNNT Growth on The SiC fibers

Morphologies of the BNNT grown SiC fiber surface was analyzed using scanning electron microscopy. SEM images of BNNT/ SiC_f structures using secondary electron and in-lens techniques allowed detailed evaluation of the BNNT morphologies. However, since both BNNTs and SiC fiber are insulators, samples were coated with gold/platinum to introduce an electron flow path from the sample-to-sample stage to the ground. In typical SEM analysis, samples were coated with conductive material for two minutes under 40 kV voltage. The main parameters that were evaluated to confirm successful growth were the surface coverage of the BNNTs on the fiber surfaces, bamboo-like morphologies for the BNNTs which ensures the highest specific surface area, no

degradation at the core of the fibers ensuring preserved mechanical properties, SiC surface growth of the BNNTs rather than the floating BNNT growth and finally low diameter for the BNNTs.

SEM images of the samples prepared at 1200 °C reaction temperature in 60 minutes growth time are shown in Figure 2.12. Figure 2.12. a show the clean surface of the SiC fiber as a result of the chemical desizing and plasma cleaning. Although fiber is coated with Fe and Mg catalyst particles, their size is too small to be observed under the SEM. The second image shows the final product of the growth, a thick “fuzzy fiber” coating on the surface of the fibers. Full coverage of the surface can be interpreted from the SEM image. BNNTs on the surface of the SiC have diameters around 80 – 150 nm with a bamboo-like morphology. The inset of the image shows the dense morphology of the BNNT coating and its networked nature (Figure 2.12. b).

When the surface of the fiber was etched selectively (Figure 2.12. c), we have seen that BNNTs were grown on the surface of the fiber rather than anchor-free floating. The surface of the fibers has some droplets on it which we believed to be BNNT nucleation sites in line with the V-L-S growth theory mentioned in the introduction part. A cross-section image of the BNNT/SiC fiber sample (Figure 2.12. d) showed that a circular cross-section of the fiber was preserved even after the growth of BNNTs on the surface. Although most of the BNNTs have clean tips, some of them also have cone-like tips with relatively short lengths. We theorize that this might be the result of either overgrowth of the BNNTs that allow diameter increase as well as length increase resulting in cone-like BNNTs [81] or it can be because these nanotubes are grown from different by-product boron sources like $Mg_3(BO_3)_2$ rather than the traditionally accepted $B_2O_3 + NH_3$ reaction product boron precursor [82].

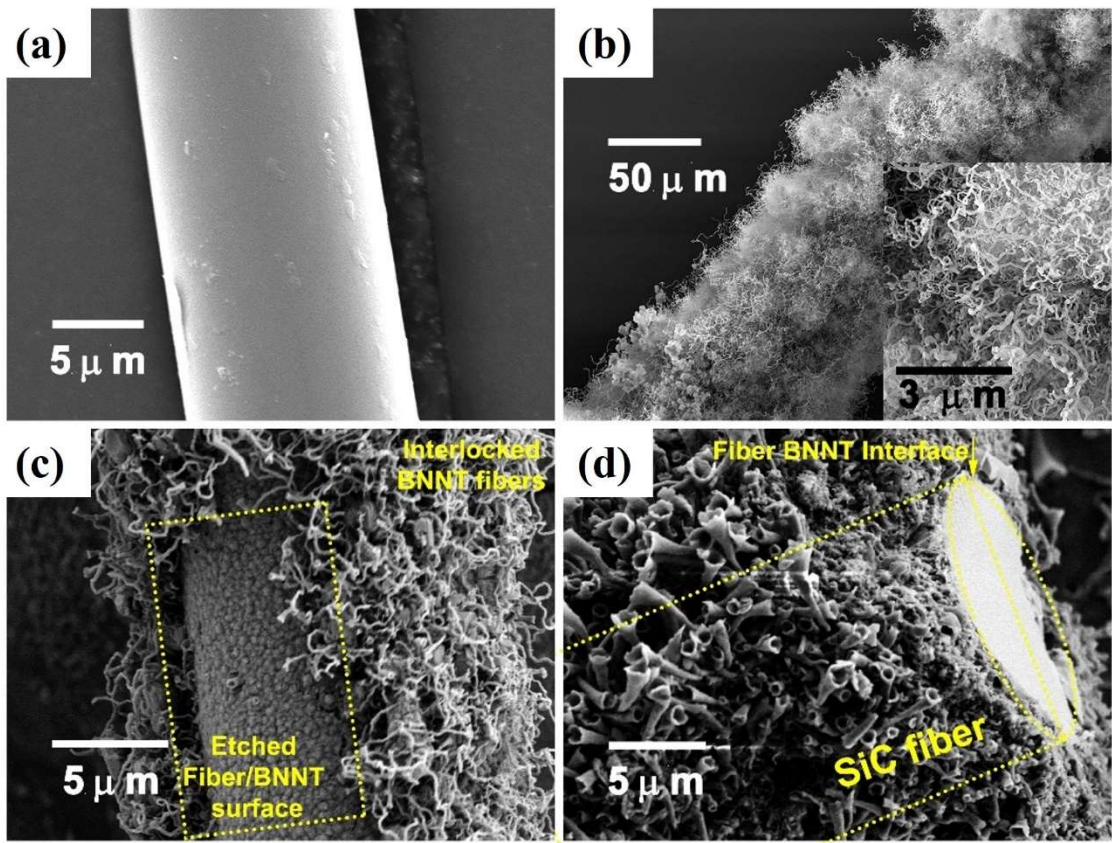


Figure 2.12 SEM images of (a) chemically desized, plasma-treated, and dip catalyzed SiC fiber, (b) SiC fiber with BNNT “fuzzy fiber” grown on it at 1200 °C for 60 minutes, (c) selectively etched surface of the SiC fiber showing the nucleation sites on the surface, and (d) cross-section image of the fiber with a preserved circular cross-section of the fiber.

In order to confirm the quality and the morphology of the BNNTs, a TEM image of the single BNNTs was also taken. TEM images allowed us to calculate the number of walls for the as-grown BNNTs, confirmed the tube morphology and the chemical composition of the nanotubes. Figure 2.13. a show the HRTEM image of the single nanotube. The lighter color of the core of the tube compared to the darker color of the edges proved the hollow tube morphology of the tubes. Moreover, the walls of the tubes have a parallel orientation with respect to tube axes, suggesting a highly ordered zig-zag nanotube structure [68]. The nanotubes seem to have diameters close to 20 – 30 nm, with a multi-walled tube morphology. Profile analysis of the single BNNT (Figure 2.13. b) also showed the multiwalled characteristic of the nanotubes with a 33 number of walls, with each peak representing a wall, for the nanotube with an interwall distance of 0.33 nm

(consistent with the d_{002} interlayer spacing of the h-BN) [83]. EELS spectrum of the single BNNT (Figure 2.13. c) confirmed the purity and the quality of the BNNTs with visible B K-edge and the N K-edge at the previously reported electron energy loss positions [84]. Furthermore, strong π^* peaks of both B and N supported the existence of sp^2 -type bonding of h-BN. Finally, the diffraction pattern for the BNNT is also given in Figure 2.13. d. The characteristic circular halo diffraction pattern of the nanotubes was visible on the selected area diffraction pattern, again confirming the tube morphology of the tubes [85].

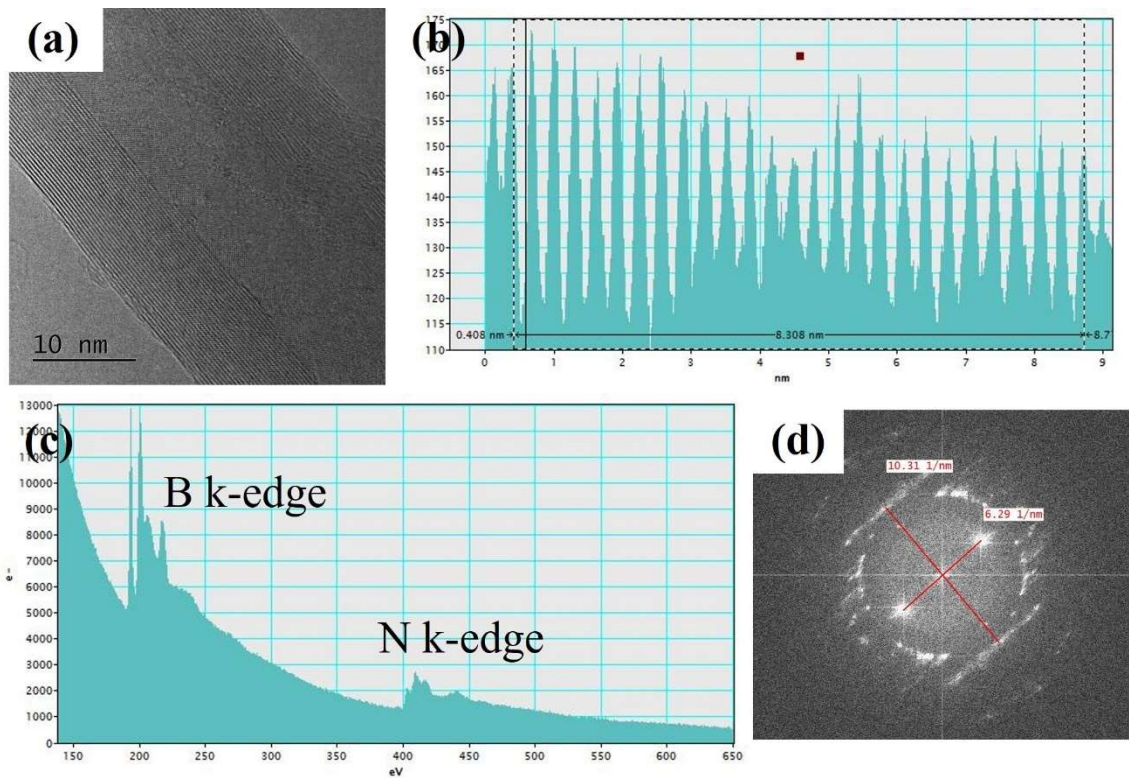


Figure 2.13 (a) HRTEM image of the single BNNT with hollow core and dark fringes present, confirming the tube morphology of the as-grown BNNTs, (b) profile analysis of single BNNTs with each peak on the graphic representing a wall in the tube structure, (c) EELS analysis of the BNNTs with strong B and N K-edge showing the chemical composition of the BNNTs. (d) Selective area diffraction pattern of the single BNNT showing the circular halo around the tube axes.

RAMAN and FTIR analyses of the BNNTs were also performed to evaluate their chemical structure and compositions. RAMAN spectroscopy (Figure 2.14. a) of the

BNNTs showed a strong intense peak at 1367 cm^{-1} corresponding to the well-defined E_{2g} in-plane vibrational mode of the h-BN structures. Furthermore, narrow and single peak also indicated the high purity of the as-grown BNNTs [86]. FTIR spectrum of the BNNTs (Figure 2.14. b) showed the 3 characteristic adsorption modes for the BNNTs. (1) Plane stretching mode of h-BN at $\sim 1348\text{ cm}^{-1}$, (2) out-of-plane radical buckling mode of BNNTs at 786 cm^{-1} , and shoulder at 1530 cm^{-1} corresponding to LO mode of BNNTs [87]. Overall, both characterization methods proved the formation of BNNTs with high purity and quality via the GVT-BOCVD method.

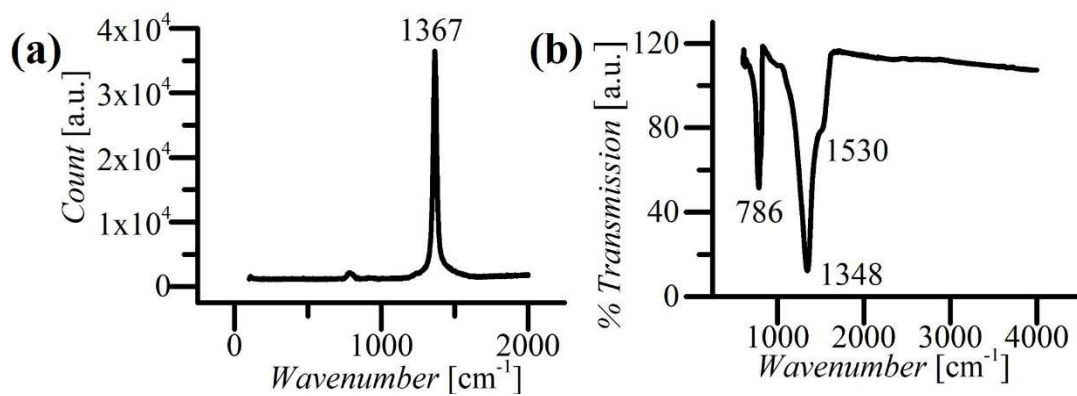


Figure 2.14 (a) RAMAN spectra of the as-grown BNNTs showing one strong and narrow peak at E_{2g} in-plane vibration band, (b) FTIR spectra of the BNNTs demonstrating characteristic absorption peaks of the BNNTs.

2.3.3 Parametric Study on Growth Conditions

Parametric study of the growth conditions was performed in order to optimize the coverage of the SiC fiber surface, the quality of the BNNTs, and the yield of the BNNTs on the SiC fiber surface. As explained earlier, the nucleation probability of the BNNTs highly depends on the temperature and the catalyst droplets according to whiskers theory of nucleation. Theory suggests that, as the temperature of the growth increases, the probability of the BNNT nucleation also increases. However, as the temperature of the process increases, so does the diameter of the BNNTs. Furthermore, an increase in temperature might cause further degradation of the SiC fiber as well as increase the cost

of the process. In order to pinpoint optimized temperature for the growth process, where fuzzy fiber BNNT coverage is maximum and the diameter of the BNNTs is minimum, we have tried out three different growth temperatures; 1000 °C, 1100 °C, and 1200 °C with growth time fixed at 60 minutes.

SEM images of the SiC fibers with BNNTs grown on them at different temperatures can be seen in Figure 2.15. When the temperature was selected to be 1000 °C (Figure 2.15. a), there was no BNNT growth observed on the surfaces of the fibers although nucleation sites could be seen. It is known that B_xO_y gasses are generated after the 1100 °C via reaction between the catalyst and the boron source and that might be the reason why nucleation is present without any growth on the surfaces of the SiC fibers. Increasing the growth temperature to 1100 °C, resulted in the growth of the BNNTs on the surface of the fibers (Figure 2.15. b). As-grown BNNTs showed uniformed coverage of the fiber surface as well as bamboo-like tube morphology. When the growth temperature was increased to 1200 °C (Figure 2.15. c), BNNT coverage again showed conformal coverage with close diameter distribution BNNTs. However, the coating became denser which is desired for our application. The denser coating can allow more Velcro-like locking between the fibers to increase interfacial interactions between the fibers. Furthermore, denser BNNT coating can prevent oxygen penetration to fiber surface more efficiently allowing better environmental protection for the fiber.

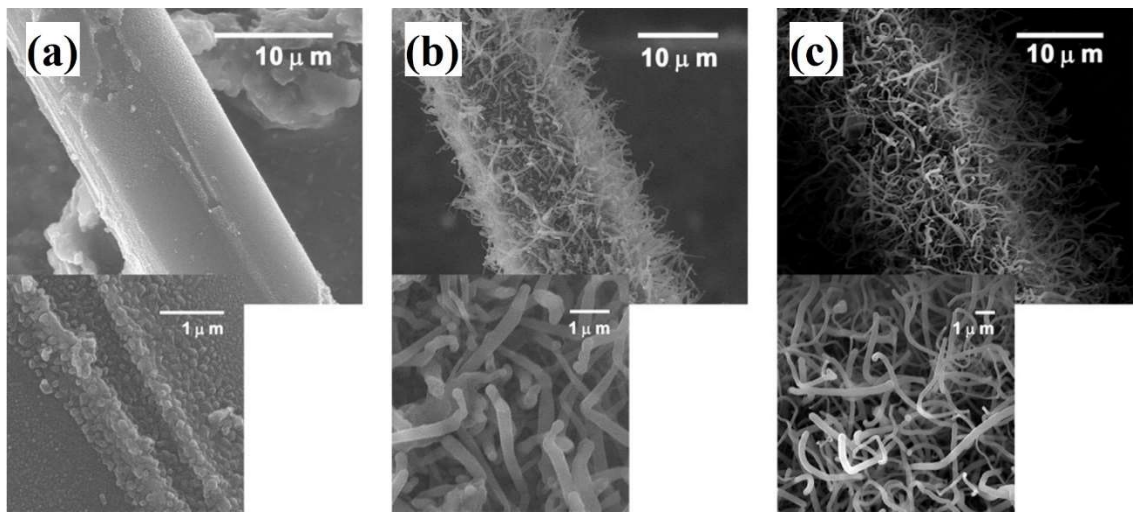


Figure 2.15 SEM images of BNNTs grown at (a) 1000 °C, (b) 1100 °C and (c) 1200 °C

Another growth parameter we investigated was the growth time of the BNNTs and their effect on the quality of the BNNTs and surface coverage of the fuzzy fiber BNNT coating.

The growth time parameter was evaluated at three different growth times; 30 minutes, 60 minutes, and 90 minutes with a fixed growth temperature of 1200 °C. SEM images of the 3 different fiber surfaces with different growth times can be seen in Figure 2.16. When the growth time was selected to be 30 minutes, BNNT growth resulted in low yield and caused partial coverage of the fiber surface which is highly undesirable for the planned application (Figure 2.16 a.). Fiber-reinforced fibers are considered as strong as their weakest point and uncovered surfaces bear the risk of lowering the mechanical properties of the overall composite. Best growth results were achieved when the growth time was selected to be 60 minutes as evident with the SEM images (Figure 2.16. b) since BNNTs grown on the surface had bamboo-like morphologies and the surface of the fibers was covered completely. However, as the growth time was increased to 90 minutes (Figure 2.16 c), the morphology of the BNNTs started to get deformed as evident in the higher magnification SEM images. In summary, 60 minutes of growth time resulted in the low BNNT diameter, high surface coverage without any deformation on the morphologies of the tubes and was selected to be optimum growth time.

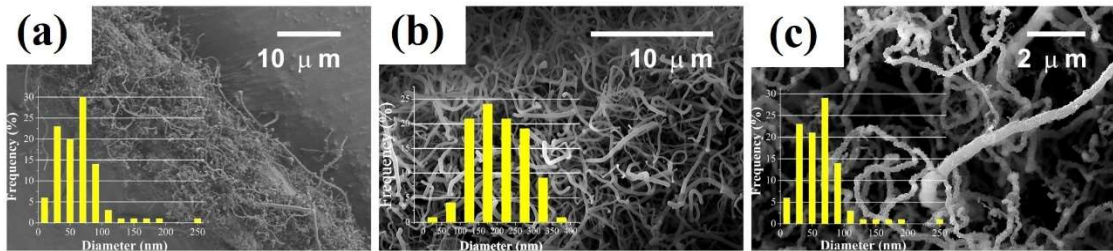


Figure 2.16 SEM images of the fibers with the BNNT growth time of (a) 30 minutes, (b) 60 minutes and (c) 90 minutes at 1200 °C

Finally, to optimize the catalyst dipping time during the catalyzing process, we have dipped SiC fibers inside the catalyst solution at three different soaking times; 15 minutes, 60 minutes, and 120 minutes. Optimizing the fiber soaking time allows achieving the highest catalyst concentration on the surface of the fibers which in turn can increase the nucleation probability of the BNNTs. EDX analysis of the three different soaking times in respect to non-soaked fibers shows that increasing the soaking time does not necessarily mean increasing the catalyst concentration on the surface of the SiC fiber (Figure 2.17). The highest Mg concentration on the surface of the fibers was achieved when the soaking time of the fiber was 15 minutes with a weight concentration of 04.62

%. However, as the time increased to 60 minutes this value regressed to 0.42 wt. % and at 120 minutes there was no Mg signal coming from the fiber surface. We think that this might be the result of the desorption of the Mg ions back into the catalyst solution with time. In EDX analysis, Fe ions were not visible which we believe due to the low concentration of the Fe compared to Si and Mg that surpasses the peak of the Fe.

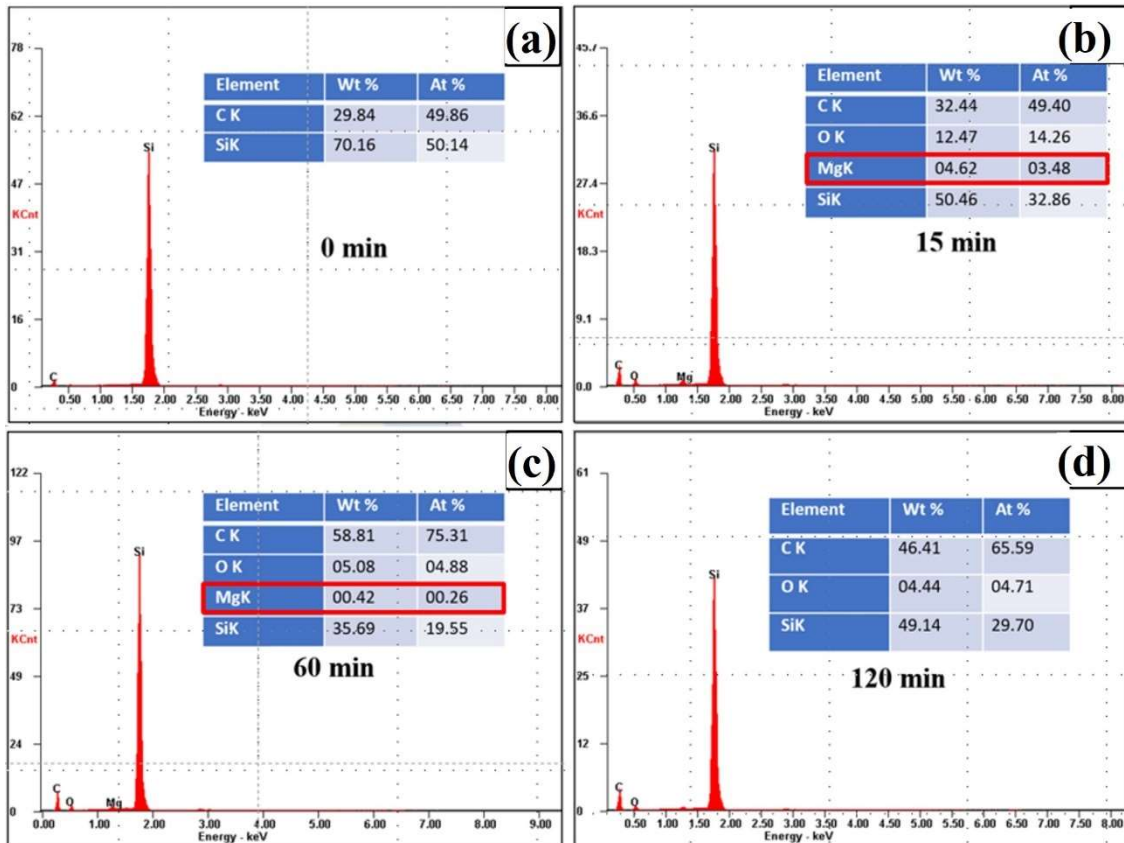


Figure 2.17 EDX spectrums of SiC fibers with a soaking time of (a) without soaking, (b) 15 minutes, (c) 60 minutes, and (d) 120 minutes.

SEM images of the above-mentioned samples also support the EDX findings (Figure 2.18). BNNTs were grown onto each sample at 1200 °C for 60 minutes and the SEM images of the samples were taken right after the growth without any after processing. Fiber without any catalyzing shows virtually no BNNT growth with BN metastable phases present on the surface of the fiber (Figure 2.18. a). When the catalyst soaking time was selected to be 15 minutes, we have observed uniform and dense coverage of the fuzzy fiber BNNT on the surface of fibers (Figure 2.18. b) and increasing the catalyst soaking time only led to BNNT phases that are formed due to insufficient growth as expected due to lack of (insufficient) catalyst droplets (Figure 2.18. c, d).

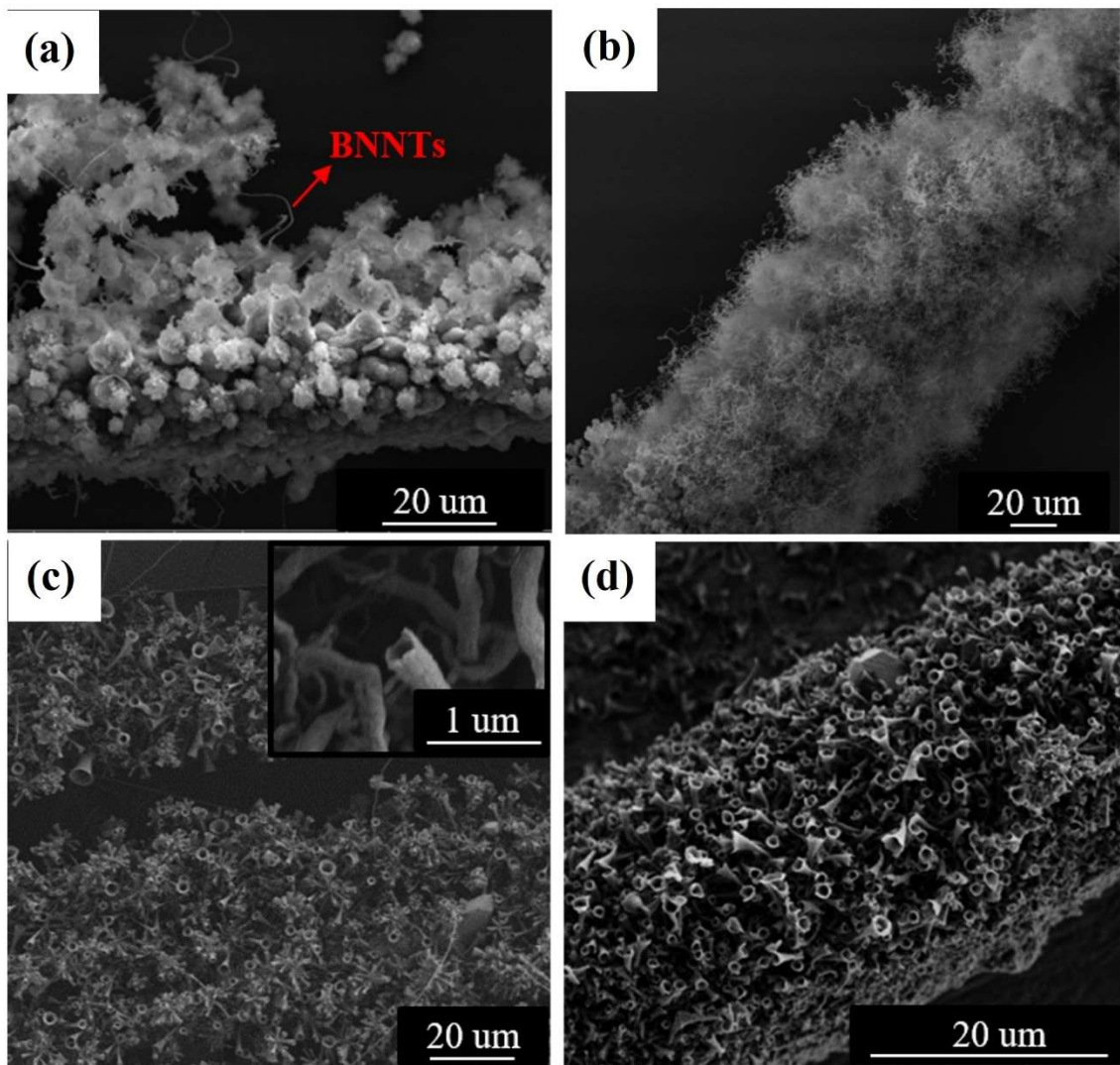


Figure 2.18 SEM images of fibers that were soaked in catalyst solution for (a) without any soaking, (b) 15 minutes, (c) 60 minutes, and (d) 120 minutes

As a result of the optimization process, we have selected 1200 °C for the temperature with 60 minutes of growth time and catalyst soaking time of 15 minutes to be optimum growth conditions for the BNNT growth on the SiC fiber surfaces. These parameters allow conformal coverage of the fiber surfaces with homogenous and small tube diameters as well as bamboo-like morphology.

2.3.4 Mechanical Characterization of BNNT/SiC_f Hierarchical Structure

The mechanical characterization of the as-prepared hierarchical structures is critical to evaluate their potential in composite applications. As such, we have conducted two different mechanical characterization: The single fiber tensile test and single fiber micromechanical bonding test.

2.3.4.1 Tensile Testing of Single SiC Fiber

In order to investigate the effect of BNNT growth on the mechanical properties of the SiC fibers, we have conducted a single fiber tensile test as explained in the experimental section. During the growth of the BNNTs, SiC fibers were exposed to high temperatures (up to 1200 °C) and highly corrosive gases that led to inevitable mechanical degradation of the fiber. The degree of the degradation and the loss of mechanical properties loss can be a deciding factor on the viability of the BNNT growth on the surface of the SiC fibers. BNNT growth without any unexpected mechanical loss coupled with the increase in the IFSS of the fiber can allow further use of these fibers in future applications. To validate this assumption, we have designed an experiment where we compared the tensile strengths of the as-received fibers (T-1), chemically desized fibers (T-2), desized fibers heated to 1200 °C under an argon atmosphere (T-3), catalyzed fibers exposed to ammonia flow at 1200°C without any BNNT growth (by removing the boron source) (T-4) and SiC fibers with BNNT grown on them (T-5). Tensile testing results can be seen in Table 2-4

Table 2-4 Tensile strength values and Weibull modulus of the SiC_f samples.

Sample Code	Conditions	Tensile Strength [MPa]	Weibull Modulus
T-1	As-received SiC _f	2101 ± 98	3.31
T-2	Desized (with DMF)	2295 ± 36	3.51
T-3	Desized /heat treated at 1200 °C	1833 ± 87	3.30
T-4	Desized/ catalyzed/ NH ₃ flow, 1200 °C	1088 ± 59	3.31
T-5	BNNT on SiC _f as ‘fuzzy fiber’	926 ± 46	4.01

The tensile strength of the T-1 samples is in line with the supplied values from the supplier with 2101 ± 98 MPa [88]. Desizing the fibers with DMF resulted in no strength loss for the fibers which is highly desirable for a desizing process to not introduce defects to fiber. Heat treating the fibers at 1200 °C which is the highest recognized temperature during the growth process showed a decrease in the tensile of the fibers with the tensile strength of the T-2 decreasing to 1833 ± 36 MPa for the T-3. This strength loss is reported extensively in the literature [89-91]. Mah *et al.* [90] explained the encountered strength loss as a result of evaporation of the CO and subsequent β-SiC grain growth. Cao *et al.* [91] further investigated the grain size increase and reported that the formation of the SiC grains was the result of vapor-solid deposition mechanism where precipitated nano-sized SiC particles (from the decomposition of the fiber surface) acted as a nucleation site for the β-SiC grain growth and the growth of the grains were driven by the reaction between SiO and the CO.

When Argon atmosphere was replaced with the more corrosive NH₃ ammonia atmosphere, the degradation and the loss of the tensile strength for the fiber became more severe. The tensile strength of the T-4 was calculated to be 1088 ± 59 MPa. However, the tensile strength of the BNNT grown SiC fiber (T-5) shows only a 14 % decrease in the tensile strength loss which represents no critical decrease in the tensile strength of the fibers. Furthermore, studies on the literature where BN coating was applied to the surface of the SiC fibers also show a similar decrease in the tensile strength of the fibers, further supporting the non-effect of the BNNT growth on the fiber surface [92, 93]. Additionally, BNNT grown fibers showed a more uniform stress distribution of flaws among the fibers as indicated by the higher Weibull modulus Figure 2.19 b.

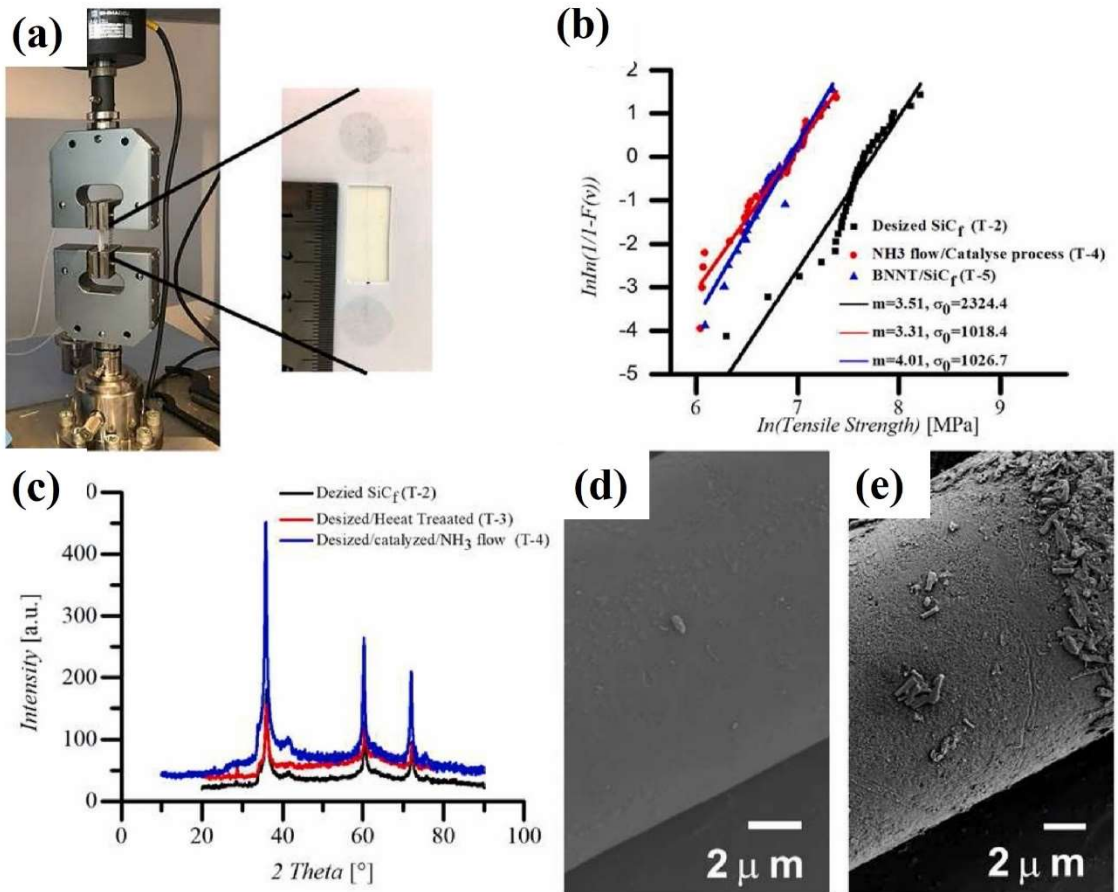


Figure 2.19 (a) Tensile test setup and prepared specimen, (b) tensile test results of T-2, T-3, T-5, and BNNTs/SiC_f, (c) XRD spectrum of T-2, T-3, T-5 samples. SEM images of (d) T-3, and (e) T-4.

XRD analysis was performed to determine this significant decrease wherein typical SiC_f peaks of the β -SiC phase were observed for desized, heat-treated, and NH₃ flown catalyzed fibers to identify the effect of NH₃ reactant gas on the SiC_f. The peaks at 36.15°, 60.2° and 71.8° of 2 Θ values corresponded to (111), (220), and (311) planes, respectively, which are typical for a SiC_f (Figure 2.19 c). 2 Θ of 41.5° in the XRD spectrum denoted the disordered stacking structure of the β -SiC ((200) plane). Although SEM images of the neat SiC_f (Figure 2.19 d) which were heat-treated at 1200 °C (T-3), depicted a smooth fiber surface with no degradation or roughness. Significant β -SiC crystal growth was detected by calculating the crystallite size of the β -SiC ((111) plane) via a Scherer equation from XRD data. While the crystallite size of the β -SiC in desized SiC_f (T-2) was 3.29 nm, after heat treatment at 1200 °C (T-3), the crystallite size of the β -SiC was 10.91 nm. In addition, for fibers exposed to BNNT growth conditions (T-4), the crystallite size

of the β -SiC was 23.38 nm, and these crystals can be seen in Figure 2.19 e. It was also reported that the SiC materials exhibited crystal growth at high temperatures, and this growth was related to excess carbon content [94] Hi Nicalon type is the SiC_f which has the most excess carbons, and these carbons were able to inhibit the crystal growth. In this case, with the aid of the inhibitive effect of the excess carbons, fiber degradation was not observed in the SEM images of the fibers despite crystal growth [94].

We have experienced significant mechanical strength loss after modifying the SiC fibers when exposed to high temperatures and an ammonia atmosphere. Similar results related to the decreased thermo-mechanical stability of SiC_f at elevated temperatures were reported in the literature. [91, 94-96] Mah, *et al.*[95] investigated the tensile strength of SiC_f under different temperatures and atmospheres, presenting a decrease in tensile strength from 1230 MPa to 848 MPa when the temperature was increased to 1400 °C under Ar flow. Furthermore, when they introduced oxygen to a high-temperature environment, they reported a more significant strength regression (660 MPa), lower than the SiC fibers' tensile strength when exposed to an ammonia atmosphere. Since high temperature and air atmosphere are the commonly experienced conditions for SiC fibers in applications, our BNNT decoration causes no further degradation of SiC fibers other than what they would have been lost during its use in an application. SiC grain growth due to carbon monoxide (CO) evaporation at high temperatures was also the main reason for the loss in mechanical performance.[91] Thus, measured tensile strength for the fibers after BNNTs growth is in accord with the reported values in strength loss attributed to crystal growth during exposure to elevated temperatures.

2.3.4.2 Interfacial Shear Strength of the BNNT/SiC_f Hierarchical Structures

A microbond test was performed to investigate the effect of the BNNTs on the interfacial interactions of F/M. Several methods, such as the nano-indentation method [97], single fiber fragmentation test, and microbond tests [98] have been reported for investigating the IFSS of F/M systems quantitatively. Required expensive equipment and complex specimen preparation of nano-indentation, and the inappropriateness of the single fiber

fragmentation test for brittle samples, a microbond test system was chosen to overcome these limitations. The microbond test has been utilized for polymeric [99], glass [100] and carbonaceous single fibers [101, 102] *etc.* due to the simple sample preparation and testing equipment, as well as its low cost, and referred to as an effective tool to study the mechanical behavior of the fiber-matrix interfaces in earlier studies [103, 104]. Photos and schematics of the customized microbond test setup equipped to the UTM can be seen in Figure 2.20 a, b., respectively. The most important test parameters of the distance between the blades and the embedded fiber length (microdroplet length) are denoted by w and L , respectively. To the best of our knowledge, this kind of module design is unique for such a fuzzy architecture study, and we hope to encourage similar tests to be used with similar approaches, through a straightforward deployability characteristic of most UTM equipment.

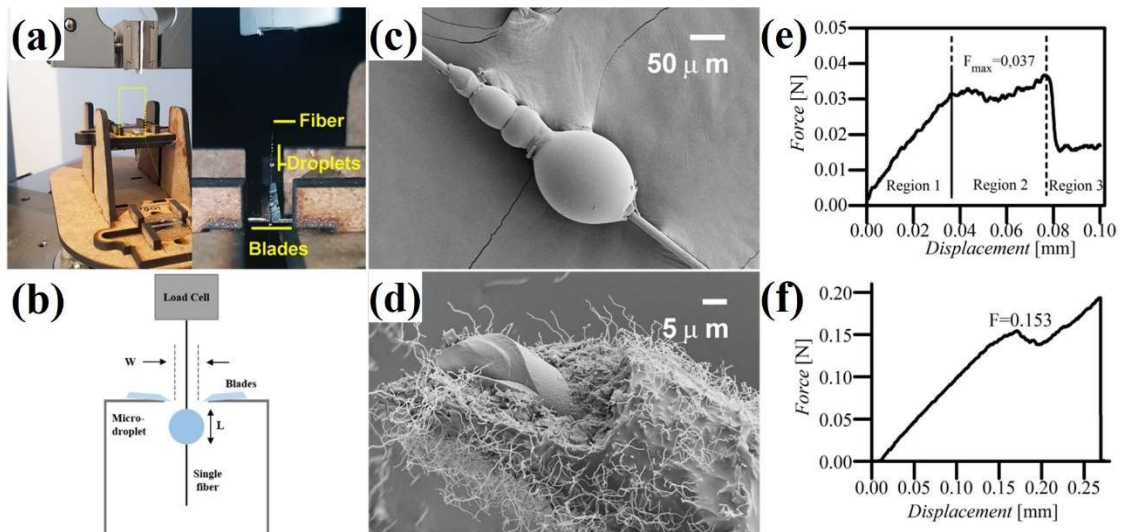


Figure 2.20 (a) Photo and (b) schematic view of the home-built microdroplet test setup, (c) SEM image of fiber with the epoxy droplet, (d) BNNT coated SiCf sample after microbond test. Load – displacement curves of (e) as-received SiCf and (f) BNNTs/SiCf.

During the microbond test, if fiber rupture was observed, the data was deemed unusable. After testing various specimens, the number of successful tests was strongly dependent on the embedded length with epoxy [105]. To obtain an interval of optimum embedded length, samples with 100 - 600 μm embedded length were tested, and it was found that the ones with 150 – 250 μm embedded length showed the highest number of successful

tests. Different interfacial shear mechanisms, such as shear debonding, microdroplet slippage, and sequential two droplets debonding [106, 107] were also observed, as also indicated in the representative SEM image showing the droplets created on the SiC fiber (Figure 2.20 c) and in the representative curve (Figure 2.20 e). In region I, debonding of the F/M interface started and was propagated until the peak force used in IFSS calculations; then droplet slippage occurred in region II with an insignificant increase in force. After full debonding, droplets started to move along the fiber axis with small resistance of frictional force, as presented in Region 3.

BNNTs/SiC_f were tested with a similar test setup to the one used for the as-received SiC_f to investigate the effect of BNNTs on the failure mode and IFSS of the F/M system. Initial tests on BNNTs/SiC_f droplets showed no resistance to slippage, indicating poor interfacial interactions between epoxy droplets and BNNTs due to the poor wettability of BNNTs, where similar findings were also reported by Zhu *et al.* [65]. In which, SiC_f/SiC composites were fabricated with BNNTs as interphase material, and the mechanical properties of the composite were investigated with and without BNNTs. They observed that hybrid BNNT composites exhibited inferior mechanical properties in terms of flexural strength than those without BNNTs, which was attributed to the high amount of porosity and voids in the interface due to the poor wettability of BNNTs. Hence, to overcome the poor wettability characteristics of BNNTs on SiC_f, plasma treatment was applied for two minutes by exposing BNNTs/SiC_f fibers to oxygen plasma at room temperature before the epoxy microdroplet formation and referred to as 2m-BNNTs/SiC_f. Such a process is expected to weaken the highly apolar nature of the BNNT surface by introducing new defects, leading to better wettability. To the best of our knowledge, such post-treatment has not been so far reported for BNNTs for the modification of a fuzzy fiber surface. During the IFSS tests on 2m-BNNTs/SiC_f, no slippage was observed, and fibers were broken, indicating the expected strong interface thus, no meaningful data could be collected. To overcome this problem, exposure time to plasma onto BNNT/SiC_f was decreased from two minutes to one minute and referred to 1m-BNNTs/SiC_f.

Since the interface in composites should be neither excessively strong nor weak, an optimum interface strength needs to be attained. The good adhesion of the epoxy matrix due to the before-mentioned oxygen plasma treatment can be seen in the fracture surface SEM image of the fiber (Figure 2.20 d). Accordingly, weak F/M bonding is preferable

for brittle materials since weak bonding allows extra energy dissipation mechanisms such as fiber pullout, debonding, and fiber bridging, increasing the material's toughness [108]. The tests on the 1m- BNNTs/SiC_f consequently yielded successful tests. During the tests, the load increased until the microdroplet started to fail. Subsequently, a load drop was observed due to the failure of the matrix, and then the load was increased again until the fiber rupture. At the time of the second load increase, the droplet fracture was hindered, and the load was carried by the fiber. The first load drop point was attained as the debonding force (Figure 2.20 f). Sato *et al.* [109] speculate that when the IFSS of the interface is too high, the interface cannot be entirely debonded before matrix failure, which is observed in this study (Figure 2.20 d) as well. Thus, we have selected to use F_{\max} before the first force drop as the pullout force. Although this approach results in lower IFFS value calculations, in practice, these IFFS values are the highest attainable IFFS values with epoxy matrix. This problem was not present in the microdroplet testing of the neat SiC fibers.

During the IFSS calculations of the SiC fibers, 15 successful sample data for neat SiC fibers and 14 successful sample data for BNNT/SiC_f were used. According to established literature 2 different methods can be used to calculate the IFSS of a sample, averaging the calculated IFSS values by using equation 2.4 or plotting force–embedded area data that intercepts the origin where the slope of the regression line gives the IFFS value [110]. In Table 2-5, IFSS values for the SiC fibers calculated using the averaging method can be seen. IFSS values of the BNNT/SiC_f were found to be 6.78 ± 0.35 MPa, an 87.8 % increase from the calculated IFSS value of 3.61 ± 0.43 of neat SiC fibers. These results are in line with the IFSS values calculated via the plotting method (Figure 2.21) where IFSS of the BNNT/SiC_f was found to be 6.63 MPa, an increase of 68.3 % compared to IFSS of neat SiC with 3.94 MPa.

Table 2-5 Calculated IFSS values of the SiC fiber samples

Sample	Sample Properties	IFSS [Nmm ⁻²]
As-SiC _f	As-received SiC _f	3.61 ± 0.43
1m-BNNT/SiC _f	1 min plasma etched BNNT/SiC _f	6.78 ± 0.35

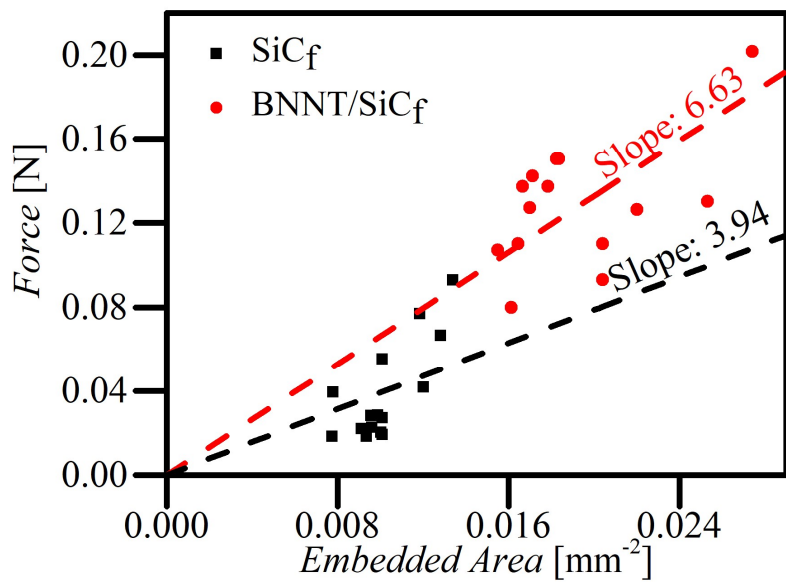


Figure 2.21 Force vs Embedded area plot for the neat SiCf and BNNT/SiCf with regression line intercepting the origin.

The IFSS values support the hypothesis of this work where we argued that “Velcro-like” interactions introduced to the surface of the fibers increase the strength of the interface interactions between the fiber and the matrix leading to enhanced IFSS values for the fiber-matrix system by preventing the fiber-fiber sliding. As can be seen from Figure 2.21, IFSS data possess some degree of scattering which can be attributed to variations of the test parameters like size and the geometry of the epoxy droplets, the surface texture of the fibers with and without BNNT growth, and contact type of the microdroplets with the blades of the test system [110, 111].

Based on the authors' knowledge, no investigations were carried out by the researchers for the IFSS of the single SiC fibers by micro bonding test. There are some studies that calculated IFSS of the single SiC fibers with different testing methods such as studies of Chai *et. al.* [97] in which they used the nano-indentation method to calculate IFSS of the single SiC fibers and reported the IFSS values around 75 MPa. However, this method and microdroplet are not comparable in the case of IFSS results because of the implementation of the test and different matrix types as they used a nano-indenter to push the SiC fiber out of the ceramic matrix as opposed to tensile testing setup. Also, Qian *et. al.* [112] reported the IFSS values for the CNT-grown carbon fibers inside an epoxy matrix using pull-out and indentation methods to test the samples. While they observed a 57 % increase

in IFSS of CNT-grown fibers through the indentation test, the IFSS values showed no change when investigated through the pull-out test which shows the strong influence of the measurement technique on the IFSS values. Another study by Harwell *et. al.* [113] investigated the bond strength of SiC coated ribbon carbon fibers inside the epoxy matrix, the same matrix material we used to create our droplets. As our research, they also reported force values scattered in a low range of 0.15 to 0.40 N, and the calculated IFSS values for the $\text{SiC}_f/\text{epoxy}$ interface were at a maximum of 12.2 MPa with a significant amount of fiber rupture observations. The microbond test to determine IFSS depends on various parameters heavily (Fiber surface texture, geometry and the size of the droplet, contact characteristic of the droplet with the blade of the testing system) and so reported IFSS values for the SiC fibers vary massively. Different IFSS values were reported for the same materials when different parametric studies were performed [114-118]; such as reported for glass fibers [117, 118] and carbon fibers [115, 116] by using microdroplet tests. It is our advice that, when one is interpreting data of the IFSS values for any system or sample, one should focus on the comparative nature of the data for the same system rather than the interlaboratory data that experienced different testing parameters.

2.4 Conclusions

F/M interface interactions of SiC_f and matrix material can be enhanced by growing “fuzzy fiber” BNNTs on the surface of such fibers via simple catalyst decoration followed by the GVT-BOCVD method at a relatively low temperature as 1200 °C, compared to earlier studies in the literature. As-grown BNNTs show full coverage of the SiC_f surface, with a bamboo-like morphology and a 20 to 150 nm tube diameter. It was found that BNNT fuzzy fiber caused no further damage to heat-treated SiC_f and fibers preserved their structural integrity. A microdroplet test showed that “fuzzy fiber” architecture in the BNNTs/ SiC_f increased the IFSS by at least 87.8 %, only limited by the strength of the epoxy matrix. It is suggested that this “fuzzy fiber” coating enhances the interfacial interactions with two mechanisms: (1) Increased fiber surface area, (2) interlocking of the

BNNTs in a “Velcro-like” fashion. Although the IFSS data reported in this research has been gathered from the epoxy/SiC fiber interface, which does not directly represent the CMC interfaces, it provides significant insight into the F/M interface between the SiC fibers and the matrix. The improved IFSS values of single SiC fibers were able to be collected quickly and easily from the epoxy droplet system, providing an effective evaluation tool before moving to CMCs. Further work will evaluate the effectiveness of the BNNT layer on the CMC materials using ceramic materials as matrix and SiC fibers. For advanced applications such as those demanded in the aerospace industry, enhanced fiber-matrix interaction for ceramic matrix composites can be achieved by engineering such hierarchical architectures on SiC fibers. The results of this chapter was published at Composite Science and Technology [119].

2.5 Acknowledgments

The authors would like to acknowledge the Safran Herakles company for funding this project. The authors would like to thank the National Research Center on Membrane Technologies and ITU universal Textile Design Center for their support. The authors would also like to thank Melike Mercan Yıldızhan and Deniz Ürk for their help in this research. Authors Deniz Köken and Ayşemin Top contributed equally to this work.

Chapter 3 H-BN NANO/MICROSTRUCTURE REINFORCED NORYL COMPOSITES AS INSULATING DIELECTRIC MATERIALS

3.1 Introduction

The steady stream of advancements in every aspect of technology and its integration into everyday life has been an indisputable fact. Nowadays, complex and time-consuming tasks are being completed by cheap and readily available devices such as cellphones (smartphones), personal computers, and smartwatches. However, these systems also require high memory capacity and high processing speeds. The “Moore’s Law”, which suggests that RAM chips need to have increased capacity by a factor of four every three years, identifies one of the most important topics that need further research, the miniaturization of electronic devices [120].

Integrated circuits (IC) that consists of layers of transmitters connected via wiring and electrically conductive wiring that feeds the IC and transmit data. The wiring inside the IC can be divided into two distinct groups; (1) Local wiring which connects the neighboring transistors and (2) global wiring which connects the far away transistors [121]. As the miniaturization of the electronic devices is achieved, the wiring density inside the device increases, eventually leading to new challenges.

One of the fields that require constant miniaturization is wireless communication. Terrestrial and satellite communications have an irreplaceable role in today's society in

the form of software radios to GPS to environmental monitoring [122]. Furthermore, as the role of mobile phones in everyday life increases, the need for material research and development becomes more critical. In particular, the packaging materials used in these devices should have low dielectric constant and loss, high thermal conductivity, good processibility, and lightweight [123].

Miniaturization of the integrated circuits also gives rise to a relatively recent challenge. As the dimensions of the device decreases, the effective distance between electrically conductive interconnect lines gets smaller and smaller. Miniaturazation leads to unwanted interaction between the conductive lines resulting in increased capacitive effects and crosstalk. [120]. As far as sub-micron devices are concerned, resistance times capacitance (RC) delay time is rapidly increasing and becoming a limiting factor in the advancement of the technology. Although this phenomenon is negligible in large-scale circuits, as the device dimensions decrease (Figure 3.1), interconnect capacitance becomes a major problem [124].

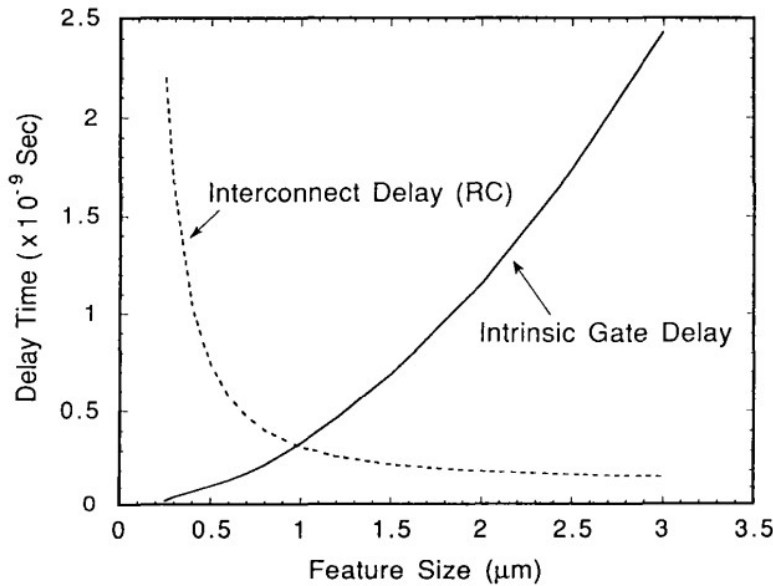


Figure 3.1 Evolution of interconnect delay and intrinsic gate delay versus feature size [124].

Degradation of the RC delay points out one of the limiting factors in IC design, the loss of signal speed due to RC delay. To estimate the interconnected RC delay employing a first-order model, Equations 3.1-3.3 demonstrate the effect of metal lines, interconnect metal's resistance, and the insulating material [125].

$$R = \frac{2\rho L}{PT} \quad (\text{Equation 3.1})$$

$$C = 2(C_L + C_V) = 2\epsilon\epsilon_0\left(\frac{2LT}{P} + \frac{LP}{2T}\right) \quad (\text{Equation 3.2})$$

$$RC = 2\rho\epsilon\epsilon_0\left(\frac{4L^2}{P^2} + \frac{L^2}{T^2}\right) \quad (\text{Equation 3.3})$$

Equation 2.3 where ρ is the specific resistance of the conductor, ϵ is the dielectric constant of the insulating material, ϵ_0 is the dielectric constant of the vacuum, L is the length of the conductive material, P is the distance between the conductive lines, T is the signal delay time, R is the resistance and the C is the capacitance highlights the 3 possible methods to reduce RC delay to achieve faster signal speed in IC. (1) Changing the layout of the IC to increase P becomes even more challenging when we consider our end goal as to miniaturize the IC circuits which lead to increased density of conductive lines, (2) engineering the specific resistance of the interconnect metal such as pure copper instead of commonly used Al(Cu) [126], and (3) decreasing the dielectric constant of the insulating material.

The relative dielectric constant consists of two parts as a complex number, permittivity ϵ'_r and the dielectric loss ϵ''_r as shown in the equation below:

$$\epsilon_r = \epsilon'_r + i\epsilon''_r \quad (\text{Equation 3.4})$$

In the complex permittivity equation, penetration of the wave is shown with ϵ'_r and materials ability to store energy is shown with ϵ''_r [127]. Both permittivity and loss are frequency-dependent parameters which are described in the Debye Equation;

$$\frac{\epsilon_r - 1}{\epsilon_r + 2} = \frac{N}{3\epsilon_0} (\alpha_e + \alpha_d + \frac{\mu^2}{3kT}) \quad (\text{Equation 3.5})$$

Where α_e represents the electronic polarization, α_d represents the distortion polarization and lastly $\frac{\mu^2}{3kT}$ represents the orientation polarization with μ showing the orientation polarization. The frequency dependence of the dielectric properties can be better seen in Figure 3.2 where each polarization dominates the system at specific frequencies.

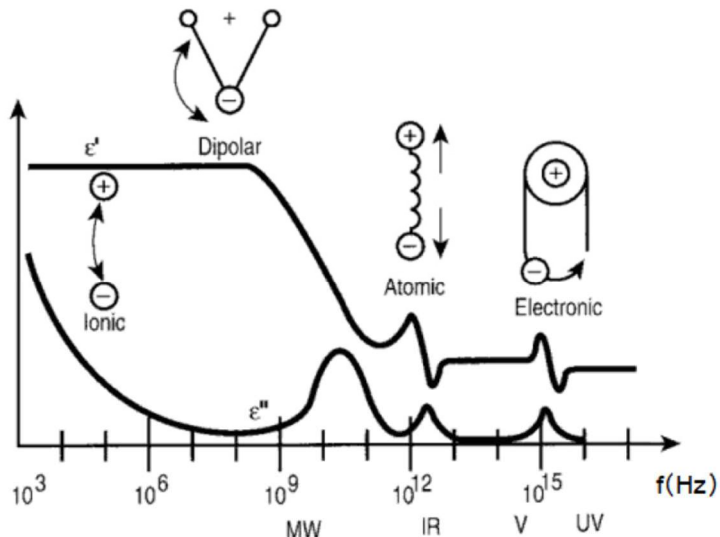


Figure 3.2 Dependence of permittivity and loss to frequency [128].

During the interaction of the dielectric material with the microwave, dielectric losses lead to heating. This loss can be the result of electronic polarization, dipolar polarization, ionic polarization, and interface polarization. Electronic polarization arises from dipole moment change under electric field with the shift of electron cloud in respect to positive nuclei. Orientation (dipolar) polarization on the other hand comes from the alignment of the randomly distributed molecules with permanent dipole moments under the applied electric field. Phase difference originating from dipoles not orientating fast enough to fluctuating electric field causes molecules to collide resulting in energy dissipation which can be observed as heat release. Ionic polarization arises from the displacement of positively and negatively charged atoms inside the lattice. This displacement induces a net dipole moment change. Finally, interfacial polarization, accumulation of the free charges in the interface inside the material causes net dipole moment change [127].

As mentioned earlier, to achieve high signal propagating speed, the design of low dielectric constant (with low dielectric loss) materials is critical. Starting in the 90s, various organic films with low k have been researched and evaluated to be integrated into the devices, but all of the efforts failed [129]. Among the first to gain attention in the search for low dielectric materials were diamond-like carbon (DLC) and fluorinated DLC (FDLC). Diamond-like carbon can be defined as amorphous carbon material containing various amounts of hydrogen (50 % to 1 %) [130]. These materials were first investigated as potential low- k insulating materials by the IBM research division. IBM showed that

the dielectric constant of the DLC can be engineered in the range of 2.7 and 3.4 by changing the deposition parameters of the plasma-assisted chemical vapor deposition however they also reported that only films with k values higher than 3.3 was suitable for to be integrated into IC due to their thermal stability at 400 °C. FLDC films with dielectric constant 2.7 on the other hand showed similar thermal stability at 400 °C compared to DLC with $k>3.3$ and showed promise to be used as interconnect material [131]. However, the delamination problem due to the reaction between the F and Ta liner prevented their integration. Further modifications to the PECVD process made by Grill *et al.* [132] showed that DLC can be a viable option after annealing it at 400 °C.

Following the research of DLC, a new hybrid material was proposed as a low- k interconnect material. PECVD-deposited SiCOH was developed with a dielectric constant lower than 2.8 with satisfying mechanical properties was developed by IBM [133]. SiCOH showed good thermal stability, mechanical properties, and hydrophobic character and was easy to implement as interconnect material therefore, SiCOH was adapted as commercial interconnect material by IBM (Figure 3.3).

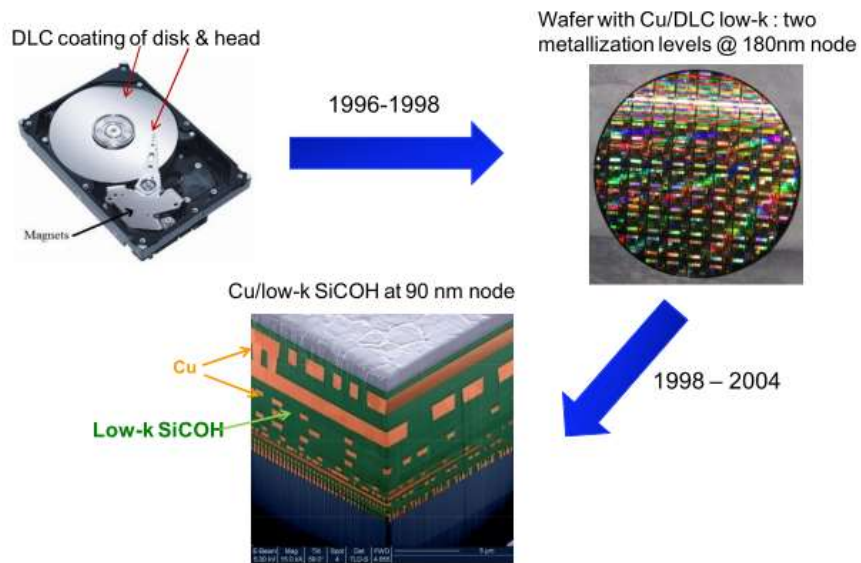


Figure 3.3 Roadmap of integration of DLC to SiCOH interconnect materials [129].

Although commercialization of the inorganic materials has been achieved, the disadvantages of these materials encouraged researchers to search for better alternatives. The intrinsic high dielectric constant, unfavorable thermal properties (thermal expansion

coefficient), and challenging machining of the inorganic materials led researchers to consider more favorable organic alternatives [134].

In addition to the low dielectric constant requirement of the intermetal insulators, the thermal stability of the material also plays a critical role. The construction of the integrated circuits requires annealing of the copper metal wires up to 400 °C – 450 °C for up to 1 hour. This means that any insulator intermetal material should also be able to withstand this annealing process [120]. Furthermore, the thermal conductivity of the insulating material should also be sufficient enough to provide adequate heat dissipation [135]. Insulating material with low thermal conductivity can lead to the formation of local hot spots, disturbing the dielectric properties as well as shortening the lifespan of the device [136].

Polymer-based materials possess excellent dielectric properties, ease of processing, and low cost, making them favorable as a packaging material [123]. Lately, there have been several polymers evaluated to be used as interconnect material; Polyimides [137-139], Poly(phenylquinoxaline)s [140], Polytetrafluoroethylene [141, 142], and many more [120]. However, these polymers suffer from low thermal conductivity, a huge challenge that must be overcome for them to be used in packaging applications [143]. To overcome the thermal conductivity bottleneck of the polymer dielectrics, several oxide and nitride ceramic fillers have been suggested in the literature.

SiO_2 is a readily available, widely used, and cost-effective material that is already commonly used in electronic devices. Several forms of silica have been utilized for thermal conductive composite production over the years [143]. The low dielectric constant and the electrical conductivity of the silica make them an ideal candidate for a packaging material however, Ling *et al.* [144] showed that the relative lower thermal conductivity of the silica limits their use in packaging applications. Their results highlighted this problem with composites reinforced with SiO_2 showing the worst thermal conductivity out of BN, alumina, and diamond (Figure 3.4).

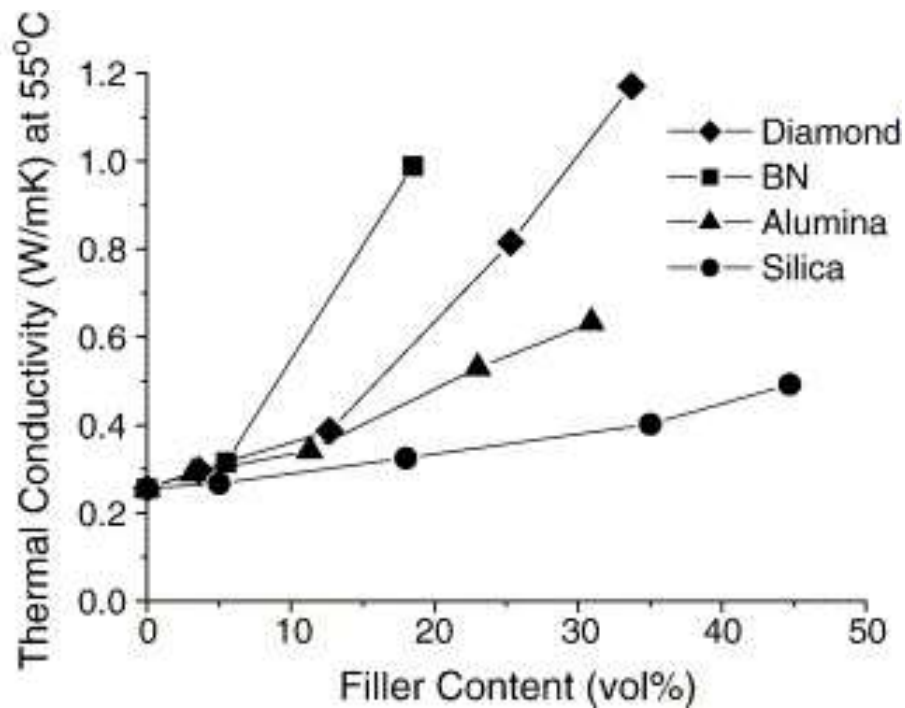


Figure 3.4 Thermal conductivities of the as-prepared composites at 55 °C show the bad performance of the silica fillers [144].

Another commonly used additive in dielectric polymer composites is alumina (Al_2O_3). Although alumina possesses high thermal conductivity and favorable electrical properties, the main drawback of using alumina in dielectric polymer composites is the high dielectric constant ($\epsilon_r = 9$) [145]. Zha *et al.* showed that Al_2O_3 fibers (AF) and graphene nanoplatelets (GNP) can enhance the thermal conductivity of the epoxy resin composites considerably ($1.62 \text{ Wm}^{-1}\text{K}^{-1}$ for 2 % GNP + 50 % Afs (v/v %)), however, the dielectric constant of the composites remained fairly high with 6 – 8 [146]. The drawback of a high dielectric constant exists with the use of Aluminum nitride (AlN) as well. Zhou *et al.* [147] reported enhanced thermal conductivity for the epoxy/AlN composites as high as $1.87 \text{ Wm}^{-1}\text{K}^{-1}$ when 0.7 % volume fraction of AlN was added to the epoxy matrix, however, composite's dielectric constant remained fairly high with $\epsilon_r = 4.4$ and dielectric loss of 0.017 at 1 MHz.

Hexagonal boron nitride (h-BN) is a structurally graphite-like, lamellar-structure ceramic [148]. h-BN is a wide band-gap semiconductor (5.97 eV [149]) with high thermal stability (stable up to 1000°C in the air [150]) and conductivity ($400 \text{ Wm}^{-1}\text{K}^{-1}$ [151]) and superior mechanical properties [152]. The most critical property of the h-BN concerning its use in

electronic packaging applications is its dielectric properties. h-BN possesses a relatively low dielectric constant (3.9) [153] and a low dielectric loss of 10^{-4} [154].

h-BN has been widely used as filler in order to enhance the thermal conductivity of the polymers. Zhang *et al.* reported enhanced thermal conductivity of the epoxy composite when reinforced with Ag-BN nacre-like structure with $23.1 \text{ Wm}^{-1}\text{K}^{-1}$ [155]. A more comparative study done on the h-BN structures and their effect on the anisotropic thermal diffusivity in regards to size, aggregation, orientation, and polymer chain rigidity of polyimide has been investigated by Tanimoto *et al.* [156]. They found that large h-BN flakes showed high anisotropy compared to small flakes and aggregated h-BN due to the inability to orientate during film casting (Figure 3.5).

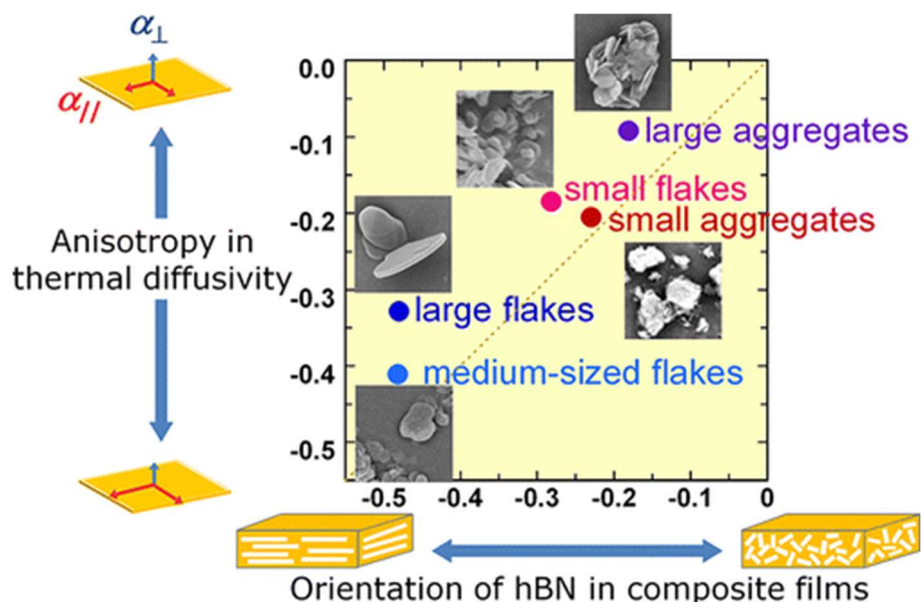


Figure 3.5 Effect of orientation of the h-BN filler on the anisotropic thermal diffusivity of the PI films [156].

Following the promising thermal enhancing capabilities of the h-BN materials, several research groups incorporate them inside the polymer matrix to investigate their dielectric potentials. Ge *et al.* used h-BN and h-BN@SiO₂ inside the polyphenylene ether resin to evaluate it as an insulation layer in copper-clad laminates [157]. Their results show that both h-BN and SiO₂ surface-modified h-BN fillers enhance the thermal conductivity of the polymer matrix ($1.08 \text{ Wm}^{-1}\text{K}^{-1}$ and $0.639 \text{ Wm}^{-1}\text{K}^{-1}$ maximum values respectively). Even more importantly for our interest, the addition of the h-BN fillers showed a slight

decrease in the relative permittivity of the CCLs at 5 GHz frequency, followed by an increase according to the “rule of mixtures”, and after critical loading, the ratio showed further decrease due to formation of voids. The dielectric loss of the CCLs stayed very low for both composites. Ternary composites of the h-BN were also evaluated. The ternary composites prepared by polymer/graphite/BN mixture showed decreased dielectric constant and loss, which is attributed to the hindrance of the electric leakage conductance by the h-BN [158]. One of the most interesting results was published by *Zhi et al.* [123]. The group functionalized the BNNT surfaces via polyhedral oligosilsesquioxane and showed that thermal conductivity of the epoxy composite was enhanced by 698 % and for % 20 weight fraction and 1360 % for 30 % weight fraction. More surprisingly, the composites showed lower dielectric constant and lower dielectric loss when compared to neat epoxy (Figure 3.6). They theorized that the decrease of both dielectric properties is the result of decreased electrical conductivity and the chain mobility hindrance due to BNNT addition. Their results are the first reported dielectric constant and loss reduction with the addition of the ceramic filler.

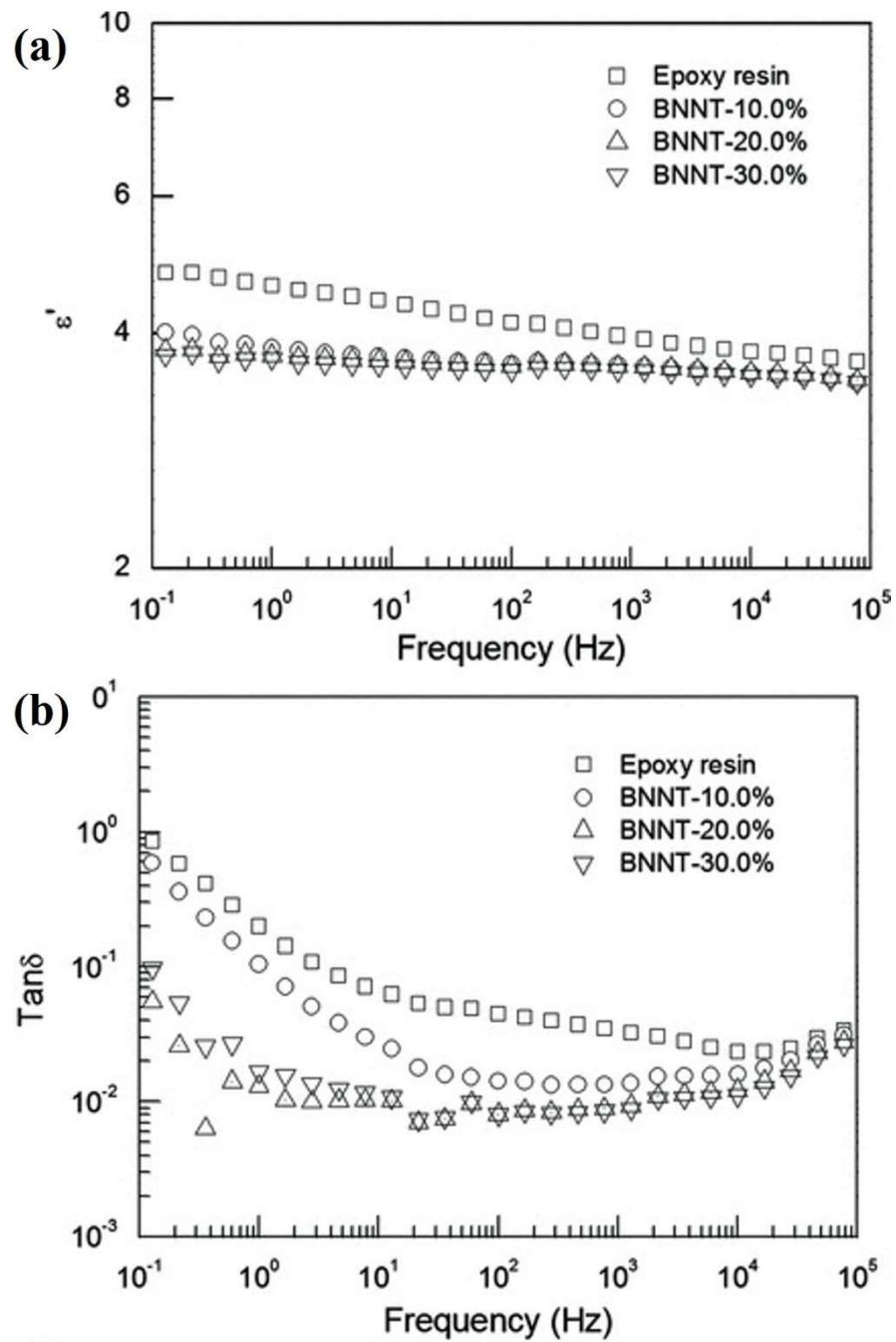
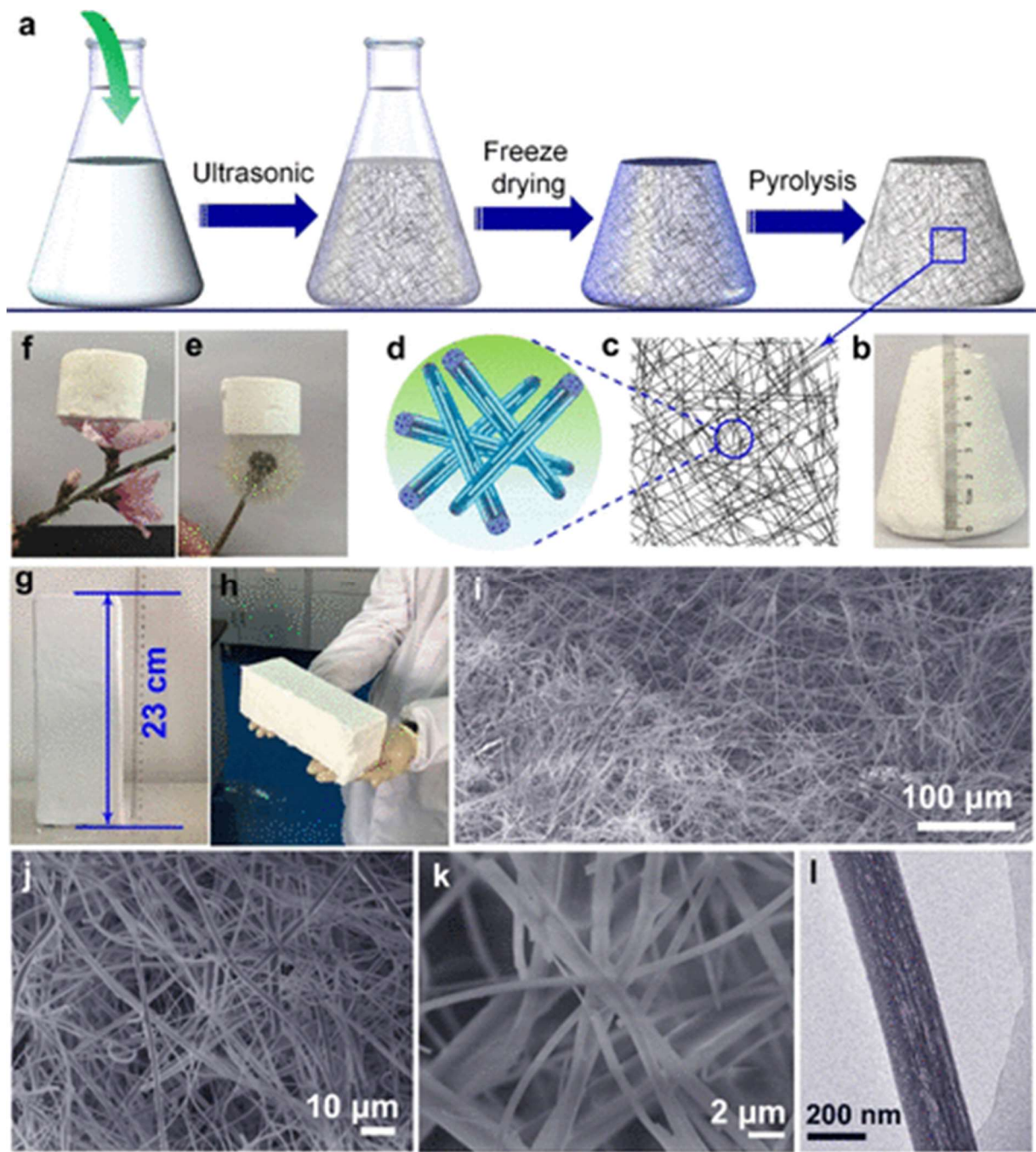


Figure 3.6 Change of (a) dielectric constant and (a) dielectric loss with the frequency and the BNNT filler amount [123].

The thermal conductivity of polymer composites can be further enhanced by the use of networking fillers since they allow phonon conduction on the pathways they form inside the network [159]. Even the non-high-thermal conductive fibers, when combined with h-BN, provided enhanced thermal conductivity to polymer composites. Xia *et al.* reported a 73.2 % increase of thermal conductivity when h-BN was used in combination with kenaf

fibers compared to without it and using even less h-BN filler amount (36.8 % less). They speculated that the increase of the thermal conductivity of the composite is due to kenaf fibers creating a network that connected the h-BN, allowing them to interconnect with each other [159]. BNNTs also showed promising thermal conductivity enhancement when combined with the polymer matrix. The addition of a 5 % volume ratio of BNNT inside the polyvinyl alcohol with orientation showed thermal conductivity values as high as $0.54 \text{ Wm}^{-1}\text{K}^{-1}$ [160].

Considering the positive effect of the high aspect ratio BN fillers, the impact of the BN micro/nanofibers becomes an intriguing topic. BN micro/nanofibers possess low density, large specific surface area, rich pore structure, good thermal stability and conductivity, and favorable mechanical properties [160-162]. Various synthesis techniques for these microfiber structures have been proposed in the literature. Komatsu *et al.* [162] synthesized boron nitride microfibers (BN-MF) via plasma-assisted laser chemical deposition method where they reported BN-MF with diameters around 1 micrometer. Lin *et al.* [163] reported the synthesis of BN-MF from the simple melamine and boric acid mixture inside deionized water to produce $\text{M.2B}(\text{C}_3\text{N}_6\text{H}_6 \cdot 2\text{H}_2\text{O})$ which was cooled down with the help of liquid nitrogen followed by the pyrolysis at $1000 - 1300 \text{ }^{\circ}\text{C}$ under nitrogen atmosphere. The same group also reported the synthesis of porous BN-MF as ultralight multifunctional foams in which they only changed the pyrolysis atmosphere from nitrogen to ammonia (Figure 3.7) [161].



As explained earlier, the miniaturization of electronic devices is currently bottlenecked by insufficient insulating materials with low dielectric constant and dielectric loss. Although polymer materials are flexible, cheap, easy to produce, and possesses low

dielectric constant and dielectric loss, their low thermal conductivity is a considerable challenge to incorporate as an interconnect material. Several ceramic fillers have been proposed for the enhancement of the thermal conductivity of these polymers and h-BN structures are one of the most promising candidates. The literature has extensive information on the thermal conductivity enhancement of the polymers via h-BN reinforcement however a comparative study is still required to shed a light on the effect of the h-BN filler morphology on the dielectric properties of the polymer. Especially, fiber structures have been shown to enhance the thermal conductivity of polymer composites considerably. However, the evaluation of the dielectric properties of these composites is still unknown.

Herein we report the synthesis of BN-MF via simple pyrolysis method followed by the reinforcement of NORYL™ SA9000 (denoted as Noryl so forth) resin with the as-synthesized microfibers as well as h-BN micro and nanoparticles (BN-MP and BN-NP, respectively). Noryl is a poly (2,6-dimethyl phenylene oxide)(PPO) hydrophobic polymer with high thermal conductivity and low dielectric loss which makes them ideal candidates to be used as an insulator dielectric material inside electronic devices [164]. Enhancing the dielectric properties of the Noryl is a critical step for it to be commonly used in electronic device applications. Decreasing the dielectric loss and the dielectric constant of the Noryl resin coupled with its inherent good thermal conductivity makes Noryl a very promising candidate as an insulating resin.

As-synthesized BN-MF were characterized via SEM for morphological evaluation, FTIR, and RAMAN for the compositional and structural analysis. As prepared composite film morphologies were investigated with SEM, their dielectric properties were evaluated at 10 GHz using split post dielectric resonator, their T_g values were calculated using DSC and DMA, and their young modulus values were measured using DMA. The results showed that the addition of h-BN decreased both the dielectric constant and the dielectric loss of the composites at 10 GHz, as well as increased their T_g considerably. DMA analysis showed that the mechanical properties of the composite films were unaffected with the addition of the h-BN filler. The most drastic dielectric loss reduction was observed when BN-MF was added into the polymer matrix, the reasons of which will be discussed in detail later. Obtaining low dielectric constant, low dielectric loss,

mechanically robust, thermally conductive resin can allow further miniaturization of the electronic devices and advancement of the technology thereof.

3.2 Experimental

3.2.1 Techniques and Methods Used

For the fabrication of BN/Norly composites, the following equipment and chemicals were used;

Boric acid (H_3BO_3 , 99.5 % purity, Tekkim), Melamine ($C_3H_6N_6$, 99 % purity, Sigma Aldrich), Boron nitride (powder, $\sim 1 \mu m$, 98 % purity, Sigma Aldrich), Boron nitride (nanopowder, $< 150 nm$, 99 % purity, Sigma Aldrich), Xylenes (ACS reagent, $> 98.5 \%$ xylenes + ethylbenzene basis, Sigma Aldrich), NORYLTM (telechelic PPO oligomers with phenyl methacrylate end groups, SABIC), Tert butyl cumyl peroxide (EFOX T801, Akpa Kimya) Protherm ASP 11/70/250 split furnace, Mazerustar Kurabo planetary mixer/ deaerator, SCANVAC/ Coolsafe 100 – 4 Pro, Nyxinyu 3-zone tube furnace, 0 – 1 slpm Alicat flowmeter.

For the characterization of the samples, we have utilized;

The morphology of the samples was characterized with Thermo Scientific Zeiss LEO Supra 35VP FESEM and Cressington Sputter Coater 108 auto, Ultra High-Resolution Transmission Electron Microscopy (TEM)(JEM-200CFEG UHR-TEM CS corrected equipped with Garanti Quantum GIF) the chemical composition of the samples were evaluated by iS10 FTIR with ATR accessory, Renishaw inVia Reflex Raman Microscopy, and Spectrometer (532 nm laser unite), Electron Energy Loss Spectroscopy (EELS) and the dielectric analysis of the samples was carried out with QWED Split Post Dielectric Resonator at 10 GHz, TA Instruments Q2000 Differential Scanning

Calorimeter (DSC), and Mettler Toledo DMA1 dynamic mechanical analyzer, Micromeritics 3Flex BET.

3.2.2 Synthesis of Boron Nitride Microfibers

In a typical synthesis run, 4.64 g of boric acid and 3.15 g of melamine were dissolved inside 250 mL deionized water in a two-neck bottle. When the complete dissolution of the reactants was achieved, the solution was heated to 85 °C under a nitrogen atmosphere with constant magnetic stirring and was kept at that temperature for four hours. After four hours, the solution was transferred to 50 mL falcon tubes with each of them filled up to 15 mL. The solution was then quickly frozen using liquid nitrogen. After no more liquid remained, the frozen samples were placed into a freeze drier for 48 hours (The freeze-drying time depended on the amount of total precursor placed inside the drying chamber). Precursor material was collected after the end of the drying.

Precursor material was placed into the alumina boat (~ 200 mg of precursor) (Figure 3.8. a) which was then covered with silicone substrates to prevent precursors from leaving the boat (Figure 3.8. b). The alumina boat was then placed at the “sweet spot” of the furnace (Figure 3.8. c, d). The furnace was then purged with 1000 scmm nitrogen flow to get rid of any oxygen. Following the purging, the furnace was further heated up to 1100 °C with a heating rate of 5 °C/ min and was kept there for 4 hours under constant nitrogen flow (500 scmm). When the pyrolysis process was finished, the furnace was allowed to cool down to room temperature with 300 scmm nitrogen flow (Table 3-1). During the pyrolysis, the precursor decomposed and degassed CO₂, NH₃, and CO gases, leaving behind the BN-MF structure. The final white, low-density product was collected from the alumina boat (Figure 3.8. e) for further characterization. The overall reactions taking place during the BN-MF synthesis was discussed in the Results and Discussion part.

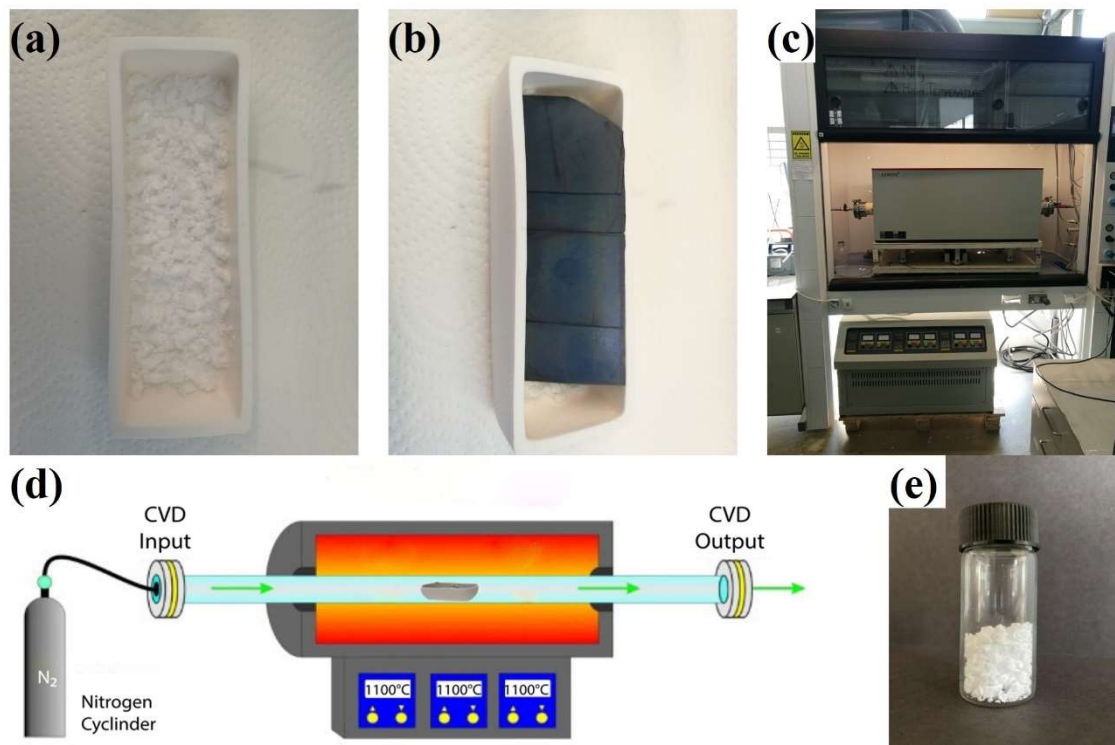


Figure 3.8 (a) The precursor placed inside the alumina boat, (b) alumina boat covered with silica substrates to prevent precursor loss, (c) 3-zone tube furnace used for the pyrolysis, (d) schematic of the pyrolysis step, (e) final BN-MF white product.

Table 3-1 Pyrolysis conditions.

Step	Temperature °C	Time Minutes	Nitrogen Flow Sccm
Purging	30	10	1000
Heating	1100	214	500
Pyrolysis	1100	240	500
Cooling	30	600+	300

3.2.3 Fabrication of BN/Noryl Composites

The preparation of the composites was carried out using the simple solution casting method. For the purpose of this research three different BN fillers (BN-MP, BN-NP, and

BN-MF) were added to the Noryl polymer matrix in three different loadings (0.5 %, 1 %, and 1.5 % (w/w %)). In a typical fabrication process, an appropriate amount of BN filler was dispersed inside 3 g of xylenes by 30 minutes of magnetic stirring followed by 5 minutes of sonication. When a homogenous dispersion was achieved, 2 g of noryl monomer was added to the dispersion and magnetically stirred for 30 minutes at room temperature. When all of the monomer agglomerates were dispersed, 0.02 (0.1 % of noryl amount) was added as a curing agent. After the addition of the cross-linker, the dispersion was deaerated for 5 minutes to get rid of any air bubbles that might exist inside the dispersion.

The dispersion was then cast into a 3 cm x 3 cm square aluminum mold with a thickness of 0.1 cm. The curing of the composites was achieved using a tube furnace to ensure an inert atmosphere during the curing process. First, the composites were heated to 70 °C and kept there for twelve hours to degas the samples, followed by curing of the polymers by slow heating of the furnace to 180 °C with a heating rate of +0.2 °C/min. The composites were kept at this temperature for two hours followed by heating to 200 °C and hold at that temperature for two hours, another heating to 220 °C, and another hold for two. After the curing was finished, the samples were allowed to cool down to room temperature and were collected from aluminum molds (Table 3-2). All of the curing processes were carried under an inert nitrogen atmosphere.

Table 3-2 Curing conditions of the BN/Noryl composites

Step	Time Minutes	Temperature °C	Nitrogen Flow Sccm
Degas Ramp	20	70	300
Degassing	720	70	300
Curing Ramp I	480	180	300
Curing I	120	180	300
Curing Ramp II	20	200	300
Curing II	120	200	300
Curing Ramp III	20	220	300
Curing III	120	220	300
Cooling	240	30	-

The slow heating rate of the curing ramp I is critical to achieving good quality composites without any air bubbles. The slow heating rate allows gentle evaporation of the xylenes solvent, preventing gasses from getting trapped inside the polymer matrix. Furthermore,

we had noticed that, when there was no constant nitrogen flow during the degassing and curing process, the final products got riddled with air bubbles, essentially rendering the sample unusable. Due to these observations, we believe that the use of tube furnaces with constant nitrogen flow is crucial to attaining good quality composites.

3.3 Results and Discussion

3.3.1 Synthesis of BN-MF from M.2B precursor

The schematic of a BN microfiber run shown in Figure 3.9 outlines the general procedure of the BN-MF synthesis. There are two important steps taking place during the synthesis of the microfibers. (1) The BN fibers inherit their morphology from the M. 2B fibers, meaning the rapid cooling of the fibers plays a critical role, and (2) Evaluation of the release gasses during the pyrolysis process and their respective temperatures.

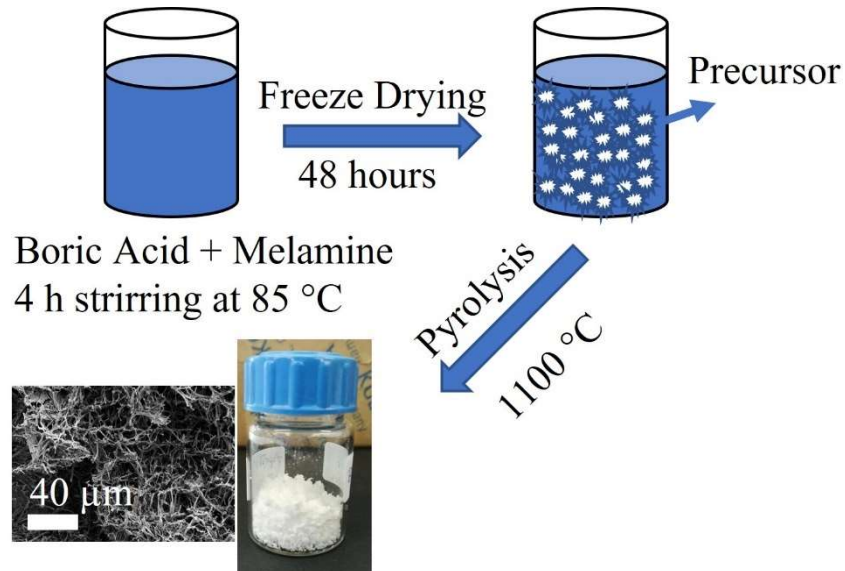


Figure 3.9 The experimental flow of the BN-MF synthesis showing all three processes.

The SEM images of the precursor collected after the freeze-drying for 48 hours show the rod-like morphology of the precursor fibers. The lower magnification image of the precursor provided in Figure 3.10 a shows the M. 2B fibers with rod-like morphology have a diameter around $\sim 2 - 3 \mu\text{m}$. The cross-section of the precursor shows that M. 2B fibers have polygonal cross-sections (Figure 3.10. b).

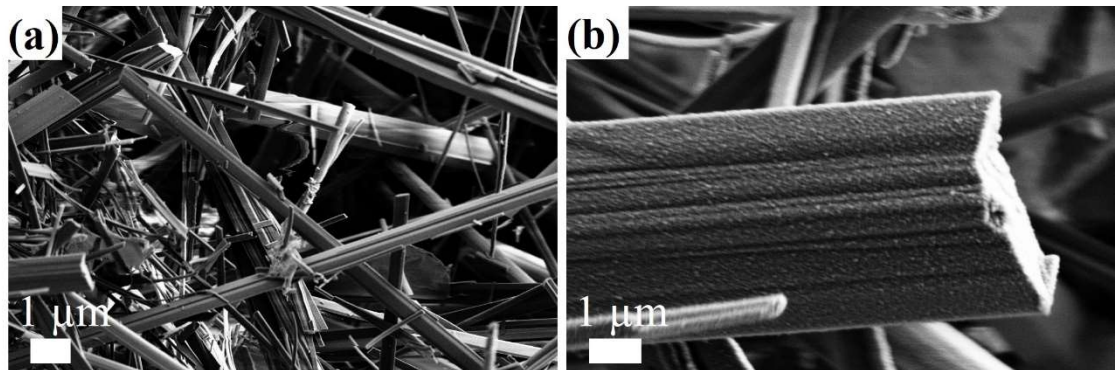


Figure 3.10 (a) Low magnification SEM image of the M. 2B precursors and (b) cross-section of the single M.2B precursor fiber.

The SEM images of the precursors are confirmed by the literature as similar structures have been reported for the synthesis of BN-MF from M. 2B precursors. Wu *et al.* reported the same morphology for the precursor they synthesized using the similar synthesis route and explained that the straight rod-like morphology of the precursor fibers arises from the inability to withstand flexural stress due to oriented hydrogen bonding in the precursor fibers [165]. Their precursor fibers also possessed $\sim 2 - 5 \mu\text{m}$ diameter like ours.

After the pyrolysis of the M. 2B precursors under a nitrogen atmosphere, the networked BN-MF structures were obtained. The low magnification SEM images show the highly networked nature of the fibers (Figure 3.11 a.). The higher magnification SEM images showed that after pyrolysis the diameter of the fibers reduced to $\sim 0.5 - 1 \mu\text{m}$. The rod shape of the fibers inherited from the precursor is still present in the SEM images which supports the theory that the morphology of the final product highly depends on the morphology of the M. 2B precursor (Figure 3.11 b.). Furthermore, the curved appearance of the fibers, in contrast to the straight rod morphology of the precursor, indicates the disappearance of the oriented hydrogen bonding of the structure. This supports the expectation of the decomposition of the C, O, and H containing compounds which are abundant inside the M. 2B precursor structure.

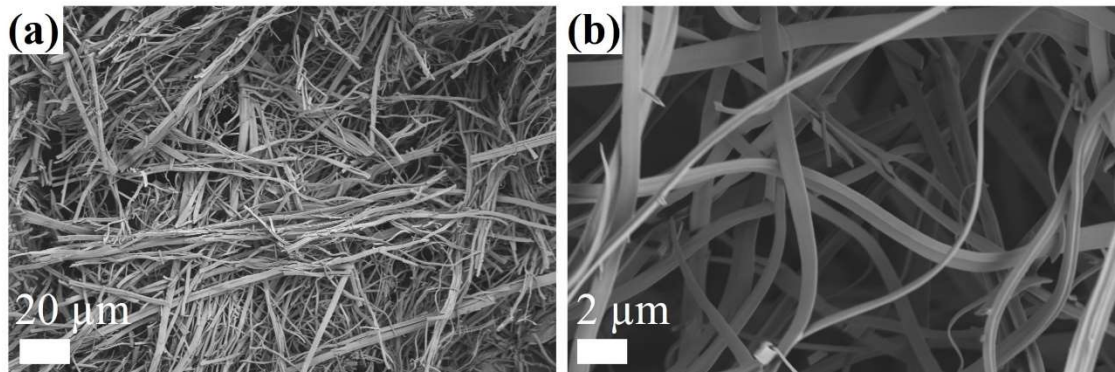


Figure 3.11 (a) Low magnification SEM image of the BN-MF and (b) high magnification SEM image of the BN-MF showing the decreased fiber diameter.

The structure of the as-synthesized fibers was further analyzed by TEM and EELS. Figure 3.12 a. shows a single BNMF with a diameter of 355 nm. The brighter spots on the TEM image represent the many pores present inside the fiber structure. A higher magnification image (Figure 3.12 b.) shows the BN layers inside the fiber with polycrystalline form and an interwall distance of 0.34 nm (Figure 3.12 d.) which is consistent with the h-BN stacking [161]. The inset of Figure 3.12 b. shows the selected area electron diffraction pattern of the fibers with characteristic diffraction rings present [161]. The brighter contrast that can be seen inside the fibers in Figure 3.12 c. suggests that there is a porous channel running through the fiber structure. This porous structure is expected since, during the pyrolysis process, the products that desorb out from the precursor leave a pore behind it. Finally, the EELS (Figure 3.12 e.) shows that BN-MF consist of B and N atoms with characteristic peaks present at 188 and 401 keV for boron k-edge and nitrogen k-edge respectively.

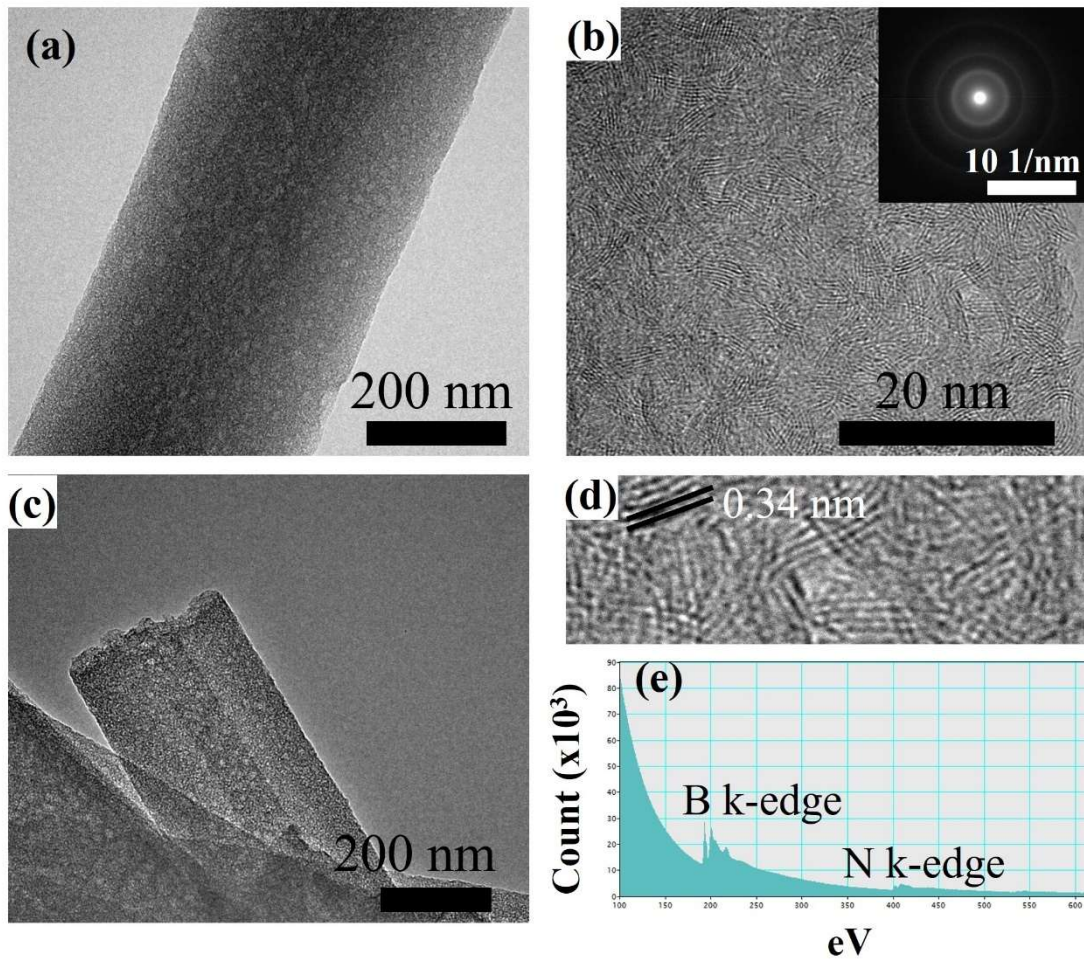


Figure 3.12 (a) TEM image of a single BNMF showing the porous structure of the fibers, (b) polycrystalline structure of the BNMFs with stacked BN layers, inset showing the SAED. (c) Tip of the BNMF with porous channels running inside the fibers, (d) interwall distance of BN layers, (e) EELS plot of the fibers showing the characteristic B and N K-edge.

Following the successful synthesis of BN-MF from M. 2B precursors, we have investigated the effect of the pyrolysis temperature on the quality of the final BN-MF product. Figure 3.13 shows the SEM images of the pyrolysis products collected after 1000 °C, 1100 °C, 1200 °C, and 1300 °C.

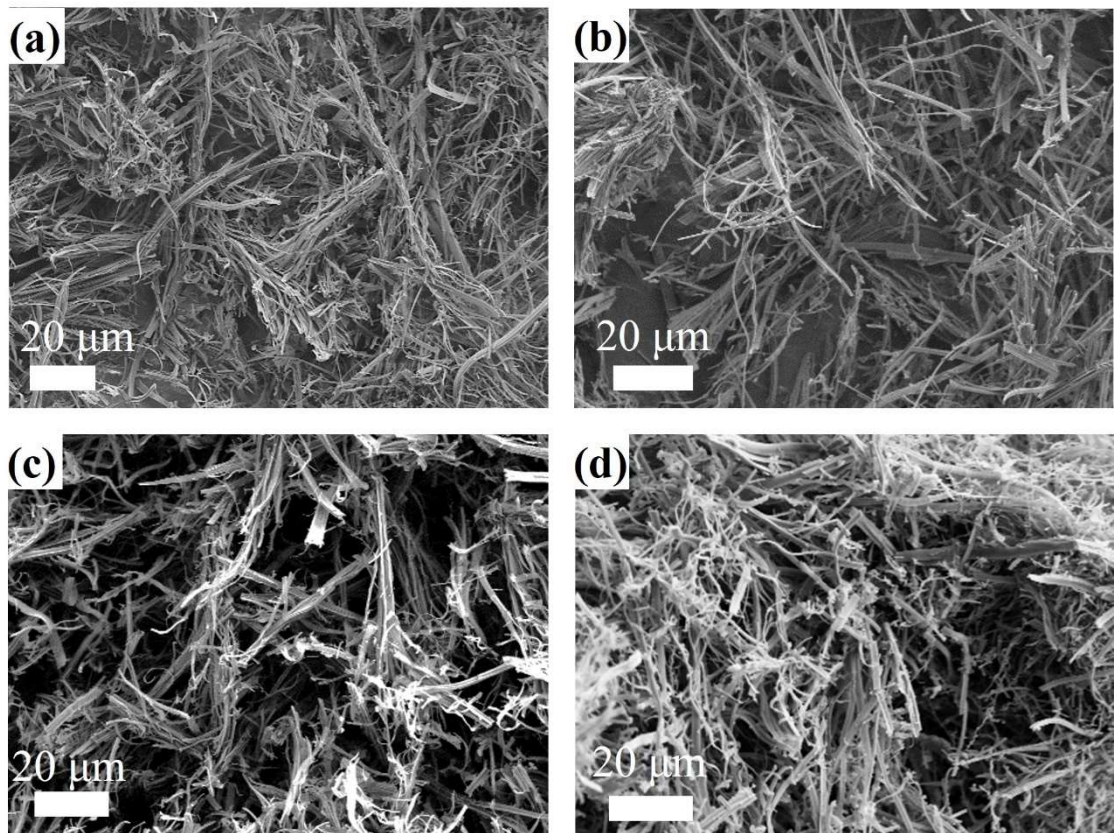


Figure 3.13 SEM images of the BN-MF with pyrolysis temperature of (a) 1000 °C, (b) 1100 °C, (c) 1200 °C, and (d) 1300 °C

The pyrolysis temperature was selected to be 1000 °C, the formation of individual fibers was inefficient, and the fibers were collected as single bundles as opposed to individual fibers. Figure 3.13. a show the non-separated fibers at the final product, suggesting insufficient pyrolysis temperature. Increasing temperature to 1100 °C results in the successful formation of the BN fibers as well as good separation of the fibers from the main mass (Figure 3.13. b). Further temperature increase resulted in unexpected branching of the BN-MFs, which we suspect might be due to decomposition of the BN phase during the pyrolysis (Figure 3.13 c, d). Although SEM images do not provide enough information to select optimum pyrolysis temperature, SEM characterization showed us that for the formation of the BN-MFs, the lowest temperature is 1100 °C.

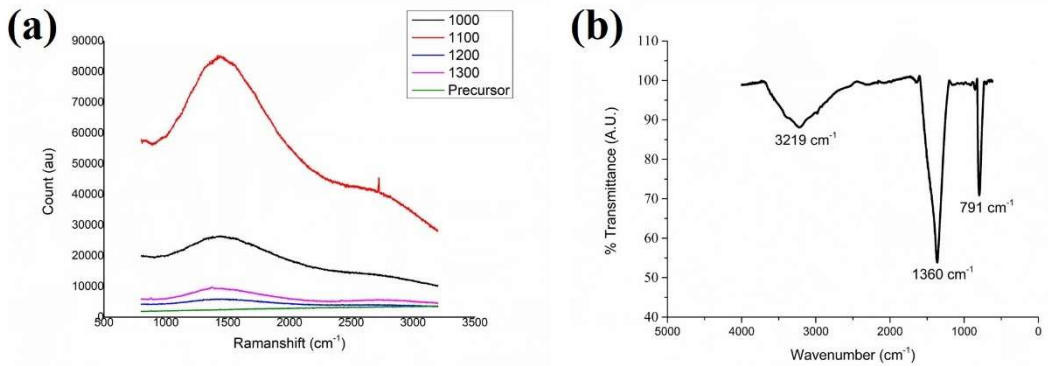


Figure 3.14 (a) RAMAN spectrum of BN-MF pyrolyzed at different temperatures, (b) FTIR spectrum of BN-MF pyrolyzed at 1100 °C.

Following the SEM analysis, we have used RAMAN and FTIR to confirm the chemical structure of the as-synthesized BN-MF. Raman analysis showed a broad peak at 1400 cm⁻¹, which is attributed to the counter-phase B-N E_{2g} vibration mode of the h-BN structure (Figure 3.14. a). However, there is a shift in the RAMAN peak from 1370 cm⁻¹ which can be attributed to weak interlayer interactions between the h-BN. The effect of the pyrolysis temperature on the final structure of the BN-MFs can be seen more clearly from the RAMAN spectrums. Before the pyrolysis process, the precursor shows no h-BN peaks. This can be attributed to the lack of B-N bonding inside the structure. However, as the pyrolysis is completed, the h-BN peak becomes visible. As suspected from the SEM images which showed branching of the fibers as well as deformation of the fiber morphology, the h-BN peak is barely noticeable in the RAMAN spectrum when the pyrolysis temperature was selected to be 1200 °C or 1300 °C. Furthermore, when the pyrolysis temperature was selected to be 1000 °C, the h-BN peak is not as apparent as the h-BN peak from 1100 °C pyrolysis temperature. As a result of RAMAN spectrums, we have selected 1100 °C as the optimum BN-MF pyrolysis temperature.

FTIR spectrum of the BN-MFs pyrolyzed at 1100 °C (Figure 3.14 b.) shows the characteristic peaks of the h-BN structures. The peaks at 1360 cm⁻¹, 791 cm⁻¹, and 3219 cm⁻¹ can be attributed to B-N, B-N-B, and B-NH₂ stretching vibration modes respectively [163]. The existence of the B-NH₂ peak can be due to impurity leftovers from the precursor.

Table 3-3 Reactions during the transformation of precursor to BN-MF reported by Wu *et al.* [165]

Reactions	Temperature Range (°C)
Dehydration of H_3BO_3 to release H_2O	150 – 200
Sublimation of $\text{C}_3\text{N}_6\text{H}_6$	200 -300
Condensation of $\text{C}_3\text{N}_6\text{H}_6$ to release NH_3	300 – 600
The reaction of carbon and oxygen to remove CO_2	500 – 700
Decomposition of -C-N to release HCN	500 – 700
Nitridation of boron oxide by NH_3 to release H_2O	700 -900

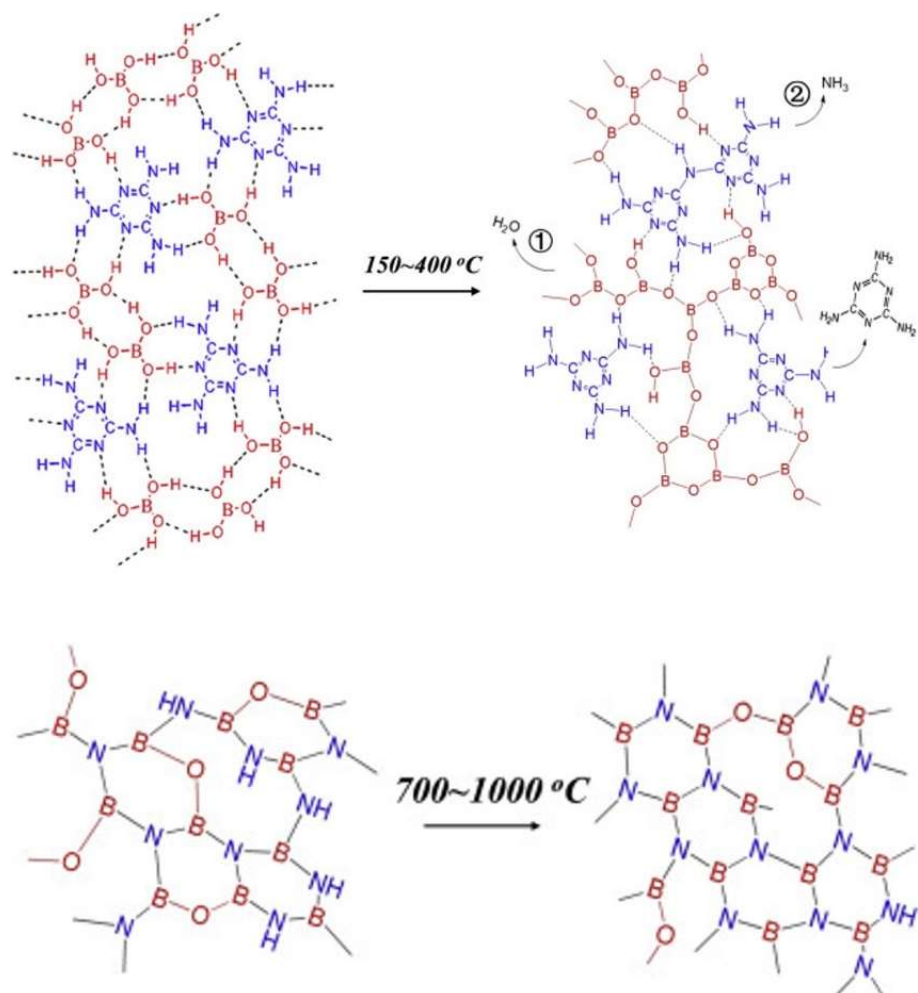


Figure 3.15 Molecular diagram of the precursor to BN-MF transformation during pyrolysis [165].

Wu *et al.* showed that six different reactions take place during the transformation of the B. 2M to BN-MF [165]. They provided theorized reactions (Table 3-3) as well as the diagram depicting the evolution of the supermolecule to BN-MF according to their results

(Figure 3.15). RAMAN and FTIR results of our as-synthesized BN-MFs correspond to theorized pyrolysis reactions as well as confirming the successful synthesis of the BN-MFs.

3.3.2 BN/Noryl Composite Fabrication

Following the successful synthesis of BN-MFs, we have reinforced the noryl resin with as-synthesized BN-MF, BN-NP, and BN-MP with various weight percentages. The characterization of the films is divided into; morphological investigation via SEM, determination of the glass transition temperatures for polymer composites via DSC and DMA, and lastly dielectric properties via split post dielectric resonator at 10 GHz at room conditions.

3.3.2.1 SEM analysis of the Composites

First, we have analyzed the BN-NP and BN-MP to determine the structures of the fillers. We have evaluated their morphology via SEM images and their structural composition via FTIR analysis. The SEM images showed that both BN-MP and BN-NP have a platelet morphology with a diameter of BN-MP in the $\sim 1 - 3 \mu\text{m}$ and BN-NP in the 80 to 600 nm (Figure 3.16 a, b). The FTIR analysis of the particles also shows the characteristic h-BN vibrations with B-N stretching vibration at 1312 cm^{-1} and B-N-B stretching vibration at 780 cm^{-1} for BN-MP, B-N stretching vibration 1305 cm^{-1} , and B-N-B stretching vibration at 760 cm^{-1} for BN-NP (Figure 3.16 c-d.) [165].

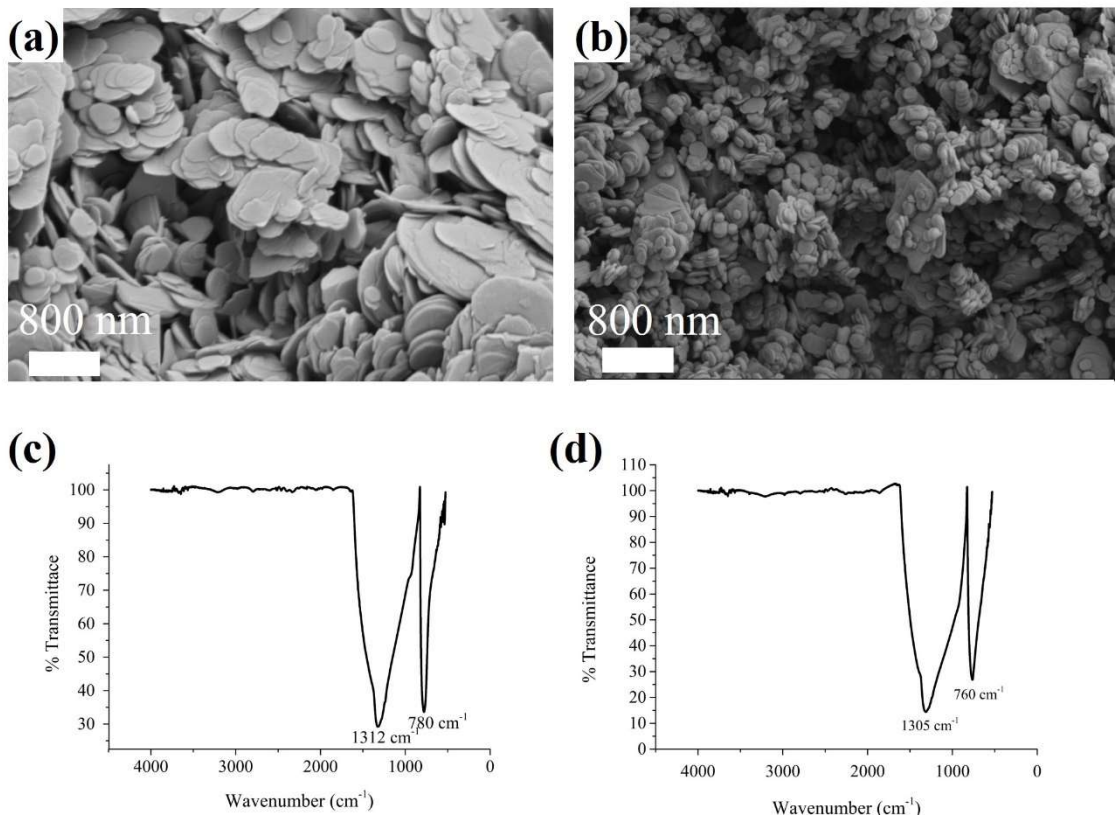


Figure 3.16 SEM images of (a) BN-MP, (b) BN-NP and FTIR spectrums of (c) BN-MP and (d) BN-NP

We have also performed BET analysis for h-BN fillers we have used in our composites. The specific surface area of the filers was investigated using N_2 adsorption and desorption isotherms at 77K. The results of the BET analysis show that (Figure 3.17), out of all three fillers, BN-MF possesses the highest specific surface area with $30.7590\text{ m}^2/\text{g}$ compared to BN-MP with $9.7205\text{ m}^2/\text{g}$ and BN-NP with $15.2537\text{ m}^2/\text{g}$. The isotherm of the BN-MF is a type IV isotherm with an H4 hysteresis loop which is consistent with what has been reported by the literature [163]. As expected, the nanoparticles show a higher specific area compared to microparticles but are lower than BN-MF. In comparison to what has been reported by the literature [161, 163], the specific surface area of the fibers is one order of magnitude smaller. The reason for this needs further information on the structure of the BN-MFs since the diameter and the morphology of the fibers appear to be fairly similar to previously mentioned studies, providing no explanation for the difference in specific surface area. Moreover, as the relative pressure approaches ~ 1 , the N_2 absorption of the h-BN fillers increases, suggesting macroporous structure, which is

also evident in the SEM images of the Fibers and the micro/nanoparticles (Figure 3.11 a. and Figure 3.16 a,b.).

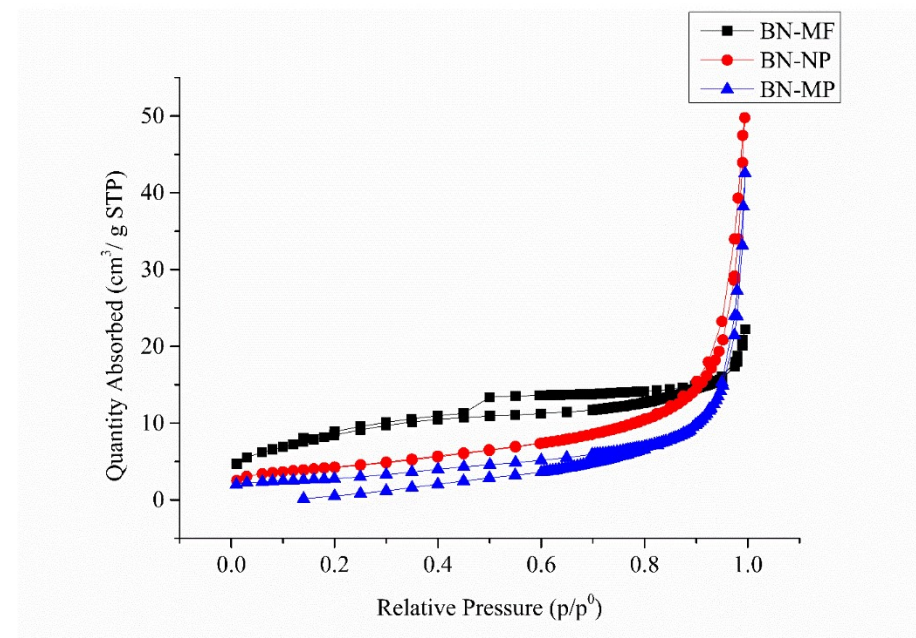


Figure 3.17 Isotherm linear plots of the h-BN fillers.

Cross-section fraction surface SEM images of the as-prepared composites with 1.5 w. % filler ratio of BN-MP, BN-NP, and BN-MF were compared to neat noryl resin is shown in Figure 3.18. The surface of the neat noryl appears to be free- of void due to good crosslinking (Figure 3.18 a.). The fracture surface of the BN-MP reinforced noryl however, shows the formation of the voids in the fracture surface which can be attributed to weak interface interaction between the BN filler and the noryl matrix (Figure 3.18 b.). There seems to be no agglomeration of the BN-MP inside the polymer matrix, indicating good dispersion of the filler material inside the polymer matrix. When the filler was selected to be BN-NP, we have observed the agglomeration of the BN-NP inside the noryl matrix (Figure 3.18 c.). Due to the high surface energy of the BN-NP fillers, unmodified (surface catalyzed) BN-NP can lead to agglomeration which might be the reason we observe agglomerated BNs in our BN-NP composites [166]. The effect of this agglomeration on the dielectric properties of the composite will be discussed in a later section. Finally, SEM images of the BN-MF reinforced composite (Figure 3.18 d) show the good distribution of the BN-MFs inside the polymer matrix. The BN-MFs can be seen as rods inside the polymer matrix. The apparent pull-out of the fibers from the polymer

matrix points to weak surface interaction between the fiber reinforcement and the polymer matrix, which causes debonding of the fillers during the fraction of the composite.

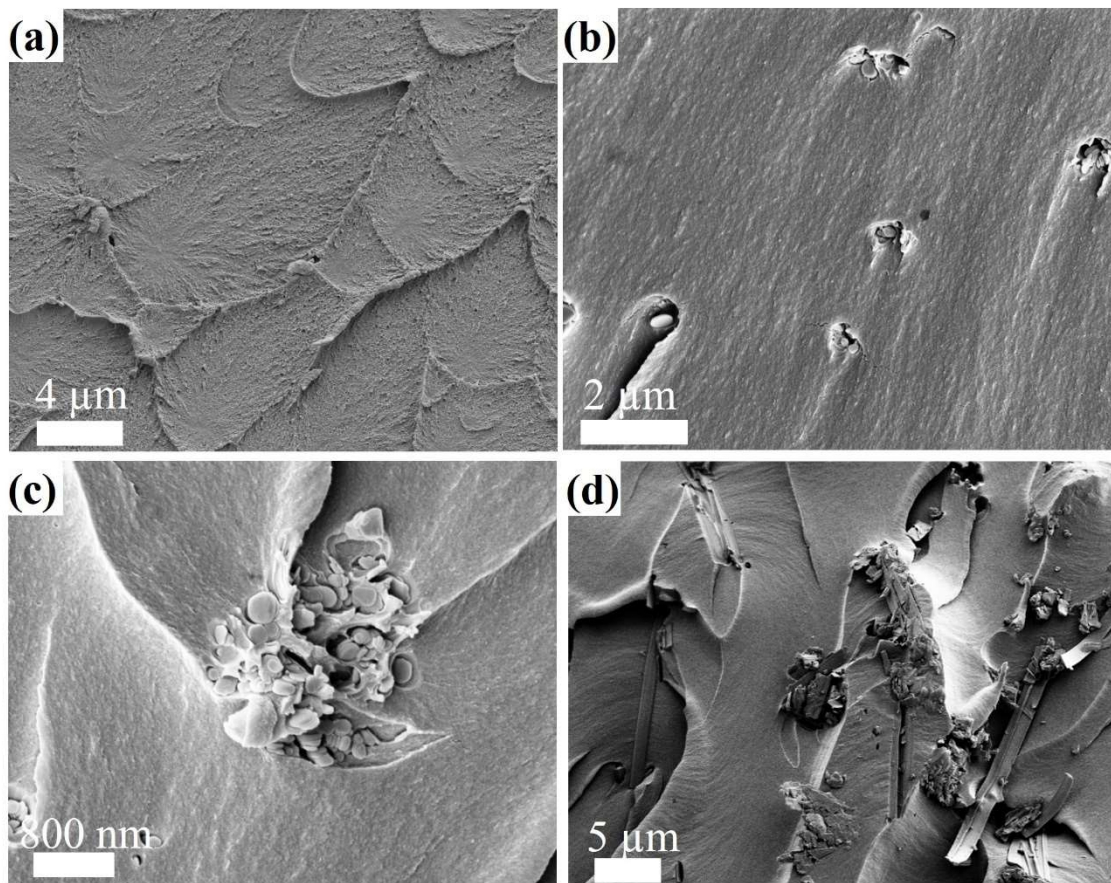


Figure 3.18 SEM images of the (a) neat noryl resin, (b) BN-MP, (c) BN-NP, (d) BN-MF with 1.5 w % for all fillers.

3.3.2.2 Determination of Glass Transition Temperatures of the BN/Noryl Composites

Determination of the glass transition temperature (T_g) of polymer composites is critical to evaluate their potential in various applications. Above the T_g , polymers lose almost all of their mechanical properties and can no longer be defined as engineering materials. To this end, we have evaluated the T_g of our composites and compared it to neat noryl resin.

First, we have analyzed our samples via DSC analysis in the temperature range of 30 – 300 °C followed by a second confirmation with the DMA analysis, again performed in the temperature range of 30 - 300 °C.

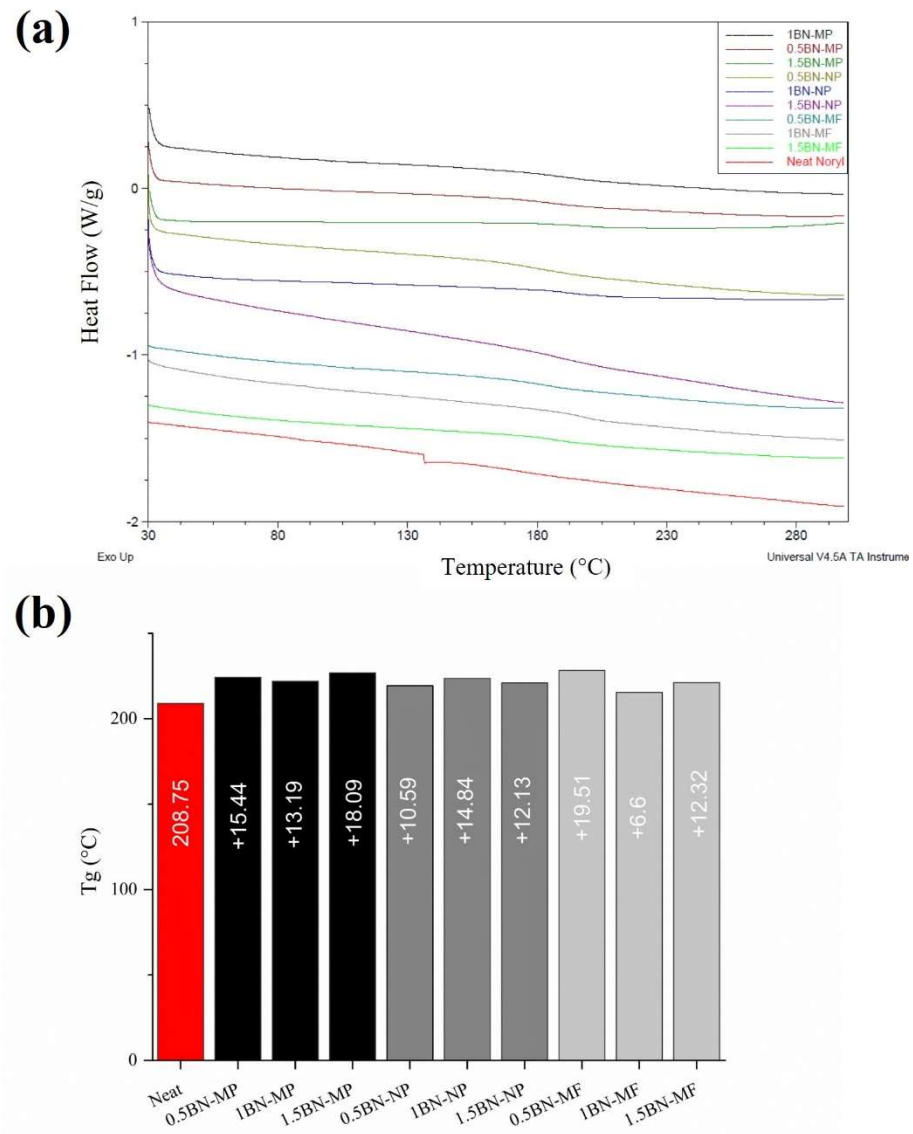


Figure 3.19 (a) DSC curves of 2nd heating cycles of the composites, (b) T_g of the BN/noryl composites.

DSC results showed that the addition of the h-BN into the noryl matrix increased the glass transition temperature of the composites considerably (Figure 3.19 a.). Micron-sized filler BN-MP and BN-MF especially increased the T_g of the composites with +15.44 °C and +19.51 °C for 0.5BN-MP and 0.5BN-MF respectively. Although there has been no research done on the effect of the BN filler on the T_g of the noryl resin, there have been

several studies showing that the addition of BNNT [123], boron nitride spheres [167], and other ceramic particles [168] increased the glass transition temperature of the polymers. The addition of the h-BN fillers restricts the movement of the polymer chains, thus decreasing the mobility of the polymer. This, in turn increases the T_g of the composites considerably. Researchers also suggested that increasing the filler volume might interfere with the curing process, leading to decreased T_g with higher loading amounts.

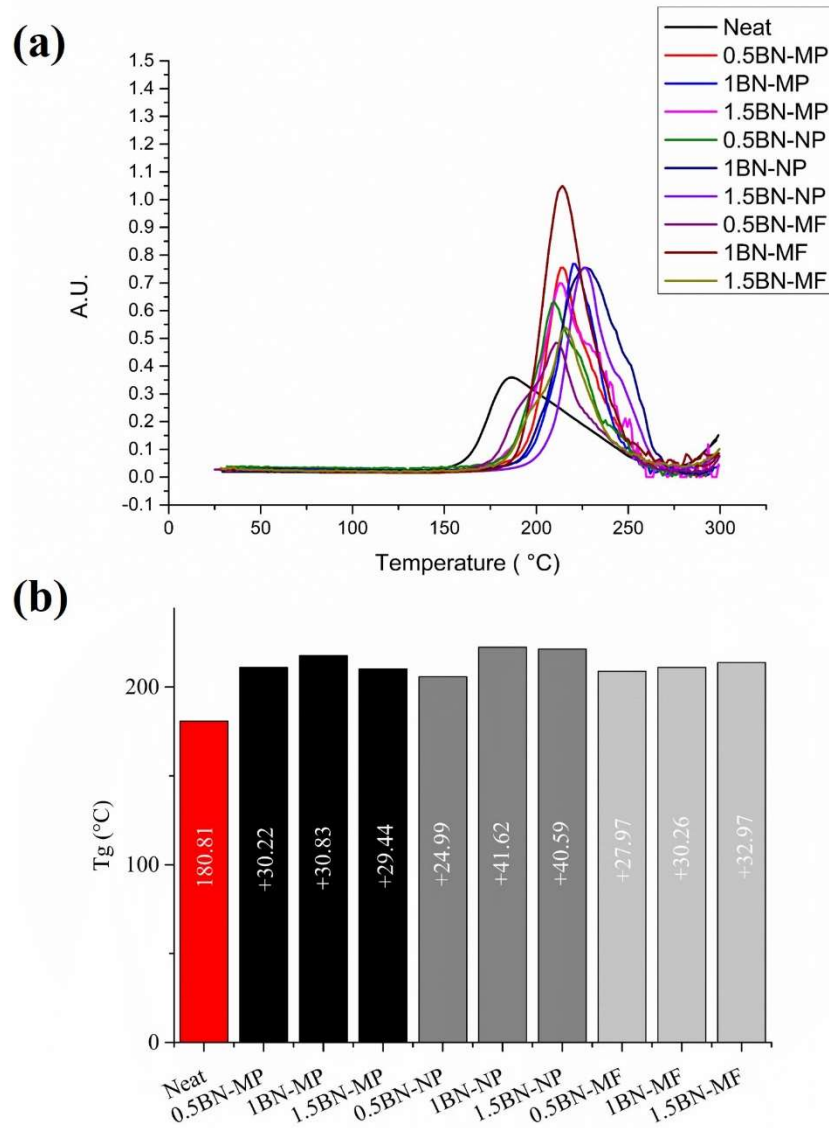


Figure 3.20 (a) Loss factor $\tan(\delta)$ plot of the BN/Noryl composites, (b) T_g of the composites with different filler morphology and filler amount.

DMA analysis of the composites also yielded similar results to what we observed from DSC analysis (Figure 3.20 a.). We have calculated the T_g of each composite sample by looking at the temperature at which the loss factor $\tan(\delta)$ plot peaked. The results

showed that (Figure 3.20 b.) addition of the h-BN fillers increased the T_g of the composites considerably (+25 to +41.62 °C), as also indicated from DSC analysis. Thermal analysis results indicate that the addition of the BN-filler increased the glass transition temperature of the noryl polymer independent of filler ratio or the filler morphology. We theorize that the locking of the chains and the hindrance of the polymer chain movements is the main reason we have observed T_g increase.

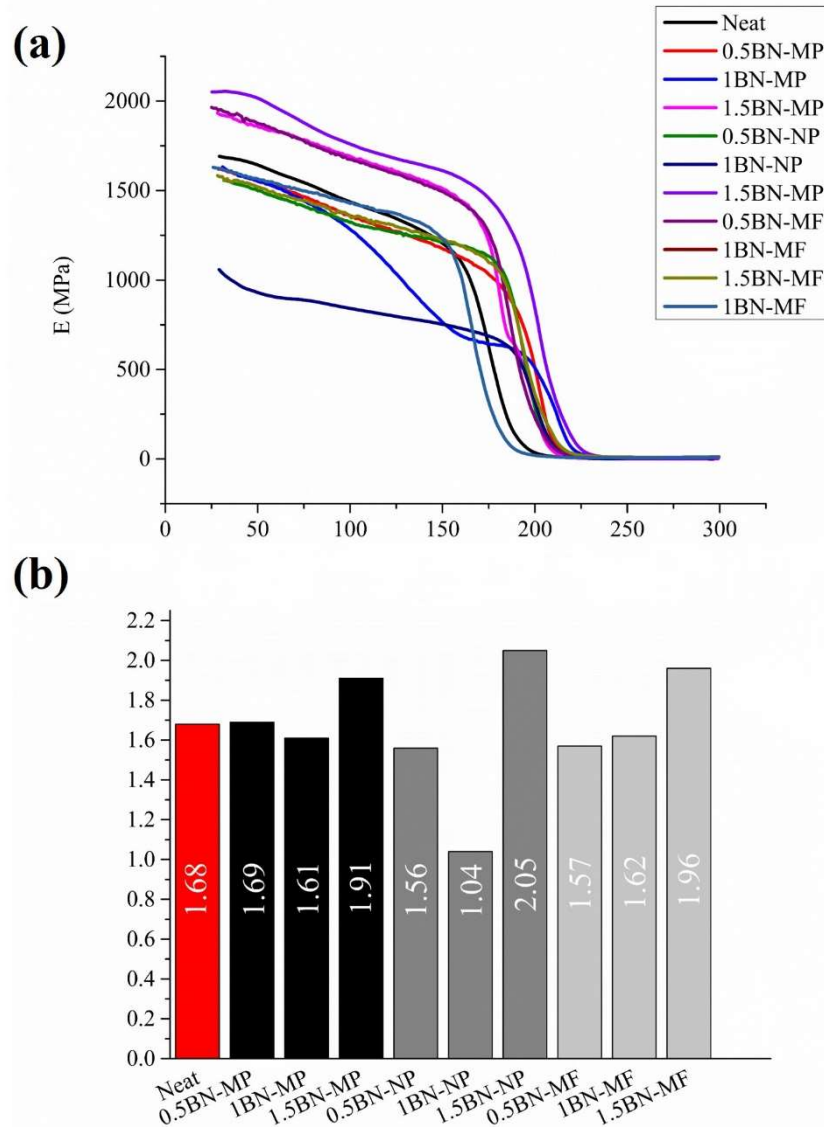


Figure 3.21 (a) E (modulus) vs temperature plot of the composites, (b) Calculated E (modulus) values of the composites.

During the DMA characterization, we have also analyzed the young modulus of the composites as well. The plot of the E modulus versus the temperature of the composites

showed that the mechanical properties of the composites are virtually unchanged compared to the neat noryl resin (Figure 3.21 a.). The young modulus of the composites varies between 1.57 MPa to 2.05 MPa, and when compared with the young modulus of the neat noryl resin (1.68) shows no significant increase or decrease. As expected, the highest modulus values were achieved when the filler amount was selected to be 1.5 % with 1.91 MPa, 2.05 MPa, and 1.96 MPa for BN-MP, BN-NP, and BN-MF respectively. In line with the reported research on the effect of nanoparticles on the mechanical properties of the polymer composites [169], BN-NP with their high aspect ratio enhanced the young modulus of the composite to its highest value.

We believe that the formation of the voids due to bad interface interactions between the BN filler and the polymer matrix, the expected young modulus enhancements have not been observed in our samples. It is known that the existence of the voids inside the matrix in composites decreases the young modulus of the composites considerably [170] thus lacking any mechanical improvement due to the addition of the h-BN filler can be explained by the negative effect of the voids inside the polymer matrix.

3.3.2.3 Dielectric Properties of BN/Noryl Composites

The dielectric properties of the as-fabricated composites were evaluated in the 10 GHz range in room conditions. We have elected to use 10 GHz due to its wide use in wireless communication applications. The results of the dielectric testing are tabulated below in Table 3-4.

Table 3-4 Dielectric properties of the as-fabricated composites at 10 GHz.

Sample Code	Dk	Df
Neat Noryl	2.625	5.37 E-03
0.5 BN-MP	2.006	2.93 E-03
1 BN-MP	1.944	2.78 E-03
1.5 BN-MP	2.06	2.83 E-03
0.5 BN-NP	2.3	3.6 E-03
1 BN-NP	2.37	3.4 E-03
1.5 BN-NP	2.23	3.5 E-03
0.5 BN-MF	2.43	3.07 E-03
1 BN-MF	2.44	2.5 E-03
1.5 BN-MF	2.22	2.37 E-03

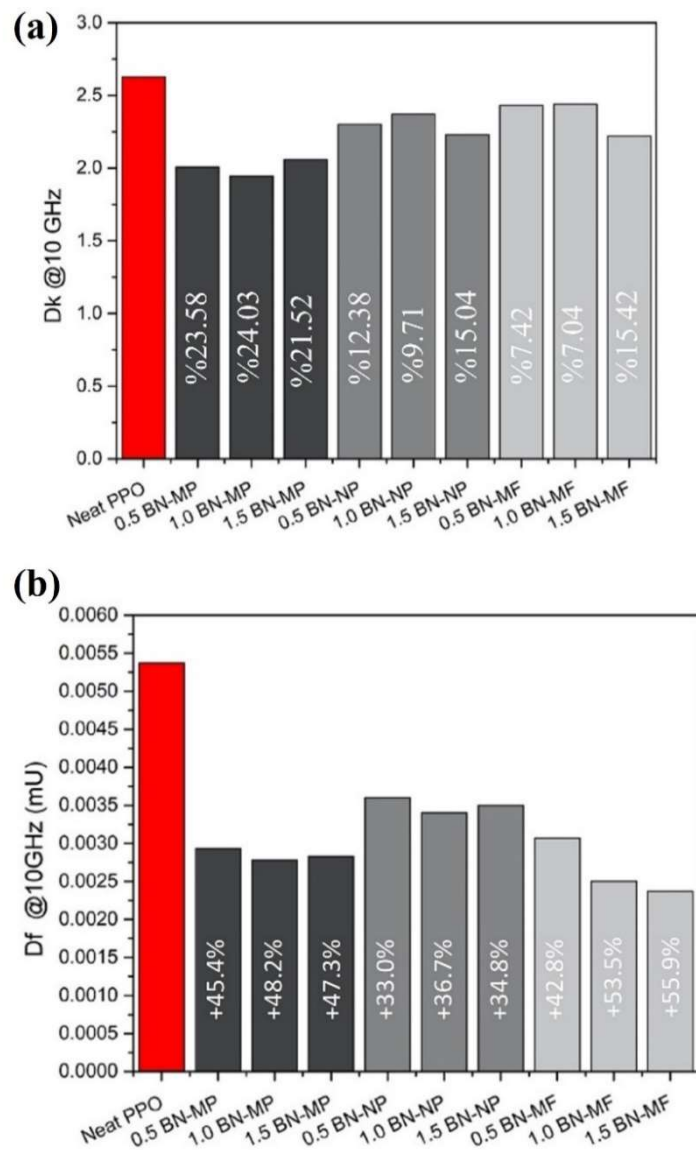


Figure 3.22 Change of dielectric properties of the composites in respect to filler ratio.

As shown in Figure 3.22, the addition of h-BN fillers inside the noryl matrix decreased the dielectric constant of the composites. The lowest Dk value was measured as 1.944 for the 1.5 BN-MP composites and the highest measured value was 2.44 for the 1 BN-MF composites, both of which are lower than the measured Dk of the neat noryl with 2.625. Typically, the dielectric constant of the composite is expected to be increased when ceramic fillers are incorporated inside the polymer matrix to the logarithmic rule of the mixture (Equation 3.7). Interestingly, our results show a lowering of the dielectric constant with the addition of the h-BN fillers. According to previous research reported, this effect can be explained with several reasons and their combination thereof.

$$\log \varepsilon_c = Y_1 \log \varepsilon_1 + Y_2 \log \varepsilon_2 \quad (\text{Equation 3.7})$$

In the rule of mixtures, ε_c , ε_1 , and ε_2 shows the dielectric constant of the composite, the dielectric constant of the noryl resin, and the dielectric constant of the h-BN filler respectively. Y_1 and Y_2 represent the volume fraction of the components. Considering that h-BN has a dielectric constant of 4 and noryl has a dielectric constant of 2.625, the expected value of the composite dielectric constant should be between these two values.

One of the reasons we have observed a lower dielectric constant than the theoretical value can be the low dielectric constant of the h-BN and especially, BN-MFs. It has been reported that BN-MF structures can have dielectric loss as low as 2.4 [171] contributing to the lowering of the noryl dielectric constant. However, even with this low Dk value, the dielectric constant of the polymers is still lower than the theoretical Dk value. The dielectric constant of our as-synthesized fibers can be even smaller than the previously reported Dk values. The TEM images we have shared in Figure 3.12 show that pores are present inside the microstructure of the BNMFs, which can lead to even further reduction of the dielectric constant of the BNMFs. This phenomenon also explains why the BNMFs performed the best out of all three h-BN fillers.

Another explanation for the decreased dielectric constant of the composites can be the formation of the voids inside the polymer matrix due to filler addition. Although there are no visible pores or voids inside the polymer matrix to the naked eye, the previously shown SEM images (Figure 3.18) indicate that the addition of the h-BN filler introduces pores into the polymer matrix. Decreased dielectric constant due to voids are also reported in the literature such as polystyrene/boron nitride nanocomposites experience lower Dk

values than neat polystyrene (PS) polymer. However both PS and BN possess higher dielectric constant than the measured dielectric constant of the composite [172]. Authors explain that the lower Dk result from formation of voids with air inside the matrix that possesses lower Dk values. They speculated that, as the filler ratio increased, the volume fraction of the void also increased leading to a reduced dielectric constant for the composites. The same phenomena were also observed when BNNTs were used as reinforcing material inside the epoxy matrix. The dielectric constant of the BNNT/epoxy composite was measured to be 8.62 at 1 MHz, whereas the theoretical values suggested 9.27 and 9.01 (Maxwell – Garnett approximation and logarithmic mixing rule respectively) [173]. The researcher suggested that the formation of the voids can be the cause behind the deviation from the theoretical model. Moreover, the intrinsic porous structure of the BNMFs can also contribute to the effect of voids inside the composite material.

In low frequencies, the interfacial polarization between the filler and the polymer can result in lower dielectric constants for the composites. Accumulation of the space charges at the interface results in interface polarization which decreases the dielectric constant of the composite. However, at high frequencies like our case (10 GHz) the probability of space charge accumulation decreases significantly [174]. Furthermore, due to large time lags of the space charges, the drifting of these charges at high frequencies becomes more unlikely. This eliminates the interfacial polarization as one of the possible explanations for the apparent lower Dk values. However, Singha *et al.* [174] argue that the addition of the fillers restricts the movement of the polymer segments and chains and thus restricts the mobility of the dipolar groups. This restriction results in a lower dielectric constant for the composites. Our glass transition temperature measurements also support this theory, since as the polymer chain mobility is hindered, the T_g of the polymer is also expected to increase which is true for our case. However, dielectric measurements carried out at 10 GHz for BaTiO₃ reinforced polymers [175] showed that at high frequencies the mobility of the dipolar groups lags to contribute to the dielectric constant of the composite and the intrinsic properties of the filler material become the dominant force in the dielectric constant of the composite.

The results show that the formation of the voids, the low dielectric constant of the h-BN, and the chain mobility hindrance of the filler material all contribute to the lowering of the

D_k of the composites to some degree. Further experimental design is required to determine the precise weight of these effects and tailoring the composites' dielectric constant.

Similar to the dielectric constant, the dielectric loss of the composites also showed a drastic decrease when h-BN fillers were added (Figure 3.22 b). The dielectric loss of the composite decreased by 55.9 % for the 1.5 BN-MF, 36.7 % for 1 BN-NP, and 47.3 % for 1.5 BN-MP. Results showed that micro additives decreased the dielectric loss of the composites the most whereas nanofillers showed a less pronounced decrease in the dielectric loss of the composites. This can be explained by the apparent agglomeration of the BN-NPs as shown in SEM images.

The literature suggests possible explanations for observed dielectric loss of the composites. When POS-BNNT were added to epoxy composites, the dielectric loss of the epoxy composites also experienced a decrease [123]. Authors theorized that the addition of the BNNT caused the electrical conductivity of the composites to decrease, leading to reduced charge carrier density for the composites leading to lower dielectric loss values. Furthermore, they speculated that good dispersion of the BNNTs introduced more interfaces resulting in inhibition of the charge carrier density. BET results of the fillers shared previously also support this theory since BN-MF with the highest specific surface area also shows the lowest dielectric loss within the composite samples. However, although BN-NP has the second-highest specific surface area, the aggregation of these fillers reduces the number of interfaces they can create inside the polymer matrix, thus inhibiting the decrease of the dielectric loss further. The same theory was also supported by other researchers [174].

Another point of view was provided by Ahn *et al.* [154]. They also reported a decreased dielectric loss for their BN/ Polyvinyl Butyral composites. They theorized that lower dielectric loss of the air inside the formed voids caused the decrease of the electric loss of the composites. It also can be speculated for our composites since they also possess air voids inside the polymer matrix and the intrinsic porous structure of the BNMFs leading to the lowest dielectric loss values for the composites.

Lastly, the extremely low intrinsic dielectric loss of the h-BN can lead to a decreased dielectric loss for the composites as theorized with the logarithmic rule of mixtures similar to what has been proposed in the dielectric constant of the composites.

Our results show similar results to what has been reported in the literature regarding both dielectric constant and dielectric loss. The formation of the voids due to h-BN filling decrease both the dielectric constant and the dielectric loss of the composites which is in line with the SEM and the dielectric characterizations of our composites. However, there are possibly more mechanisms in play that equilibrate with each other to determine the final dielectric properties of the composite. Further research of these parameters, such as determination of the porosity percentage, determination of the electrical conductivities of the composites, and evaluation of the dielectric properties of the composites in a wider range of frequencies can shed a brighter light on the dielectric properties of these composites.

3.4 Conclusions

We have presented the synthesis of BN-MFs from melamine and boric acid. The temperature optimization of the pyrolysis temperature showed that 1100 °C is the optimum pyrolysis temperature for the synthesizing high-quality BN-MFs. The synthesized fibers have a porous structure and 0.5 – 1 μm in diameter with FTIR and RAMAN spectrums confirming the B-N bonding of the structure. Fabrication of the h-BN/Noryl composites was also achieved via a simple solution casting method. The as-fabricated composites experience higher T_g values compared to neat noryl resin suggesting immobilizing of the polymer chains. The young modulus results suggest that composites suffer no strength loss or gain due to the addition of the fillers materials and the formation of voids inside the matrix balancing the theoretical strength gain from the h-BN addition. Dielectric properties of the composites showed a surprising decrease both in dielectric constant (24.03 %) and the loss (55.9 %), cause of which has been theorized

as the intrinsic porous structure of the BNMFs and the formation of voids for the dielectric constant and decrease of electrical conductivity of the composites as well as low dielectric loss of the voids inside the matrix for the dielectric loss. Lowering of dielectric properties can allow these materials to be utilized as insulation material for ICs, increasing the signal propagating speed and preventing RC time delay of the electronic devices.

As future work, we propose to follow investigations to be realized.

- Evaluation of the new precursor materials for the synthesis of the BN-MFs can lead to lower diameter fibers and higher synthesis yield for the fibers.
- Large size samples of the composites must be fabricated to evaluate their thermal conductivity to appease their potential as dielectric insulator materials further.
- The porosity of the composites must be measured to understand the effect of voids on the dielectric properties of the composites which can allow better tailoring of the dielectric properties.
- Measuring the dielectric properties of the composites in a wider frequency range to show their dependence on the change of frequency can lead to widening their application fields from microwave wavelength.
- Engineering of the void volume fraction can allow the tailoring of the mechanical properties concerning dielectric properties resulting in more precise material fabrication depending on the application.

Chapter 4 LOW-TEMPERATURE SYNTHESIS of BORON NOTRODE NANOTUBES FROM BORON MINERALS ASSISTED by SULFUR BASED MOLECULES

4.1 Introduction

After the realization of the carbon nanotubes (CNTs) by Iijima *et al.* [176], the search for nanomaterials with extraordinary mechanical, optical, thermal, and electrical properties attracted a considerable amount of interest. Boron nitride nanotubes (BNNTs) can be described as structural analogs of CNTs in which carbon network with sp^2 and sp^3 hybridization is replaced by the alternating B and N atoms with similar hybridization behavior. They show excellent mechanical properties, such as high elastic modulus [177] and superb flexibility [178], allowing them to be used in composite applications without a high filler ratio [179-183]. Furthermore, BNNTs also possess high thermal stability [184] (<800°C in air atmosphere [185]) with accompanying thermomechanical properties [186] which makes them ideal reinforcement material for high-temperature composite applications [187-189]. The electronegativity difference between the constituent B and N gives rise to the piezoelectric effect for the BNNTs, resulting in the fabrication of tunable piezoelectric polymeric composites [190]. Finally, the high neutron absorption and scattering cross-section of the BNNT (Especially BNNT with ^{10}B isotope) can lead to the design of radiation shielding materials that can protect satellites at low-earth orbit from constant radiation barrage [191, 192].

The first synthesis of the BNNTs was reported by Chopra *et al.* [193] using an arc-discharge method to synthesize pure BN nanotubes. The arc-discharge method produced BNNTs with one or double-walled morphology but only a few studies ever expanded on the volumetric synthesis of the BNNTs via the arc-discharge method and even then BNNTs were inside the grey web-like material [194]. Following this, new methods that are derived from the CNT growth system have been reported. Ball-milling [195] in which mechanical energy of the balls are transferred to boron precursor by grinding, fracturing, and thermal shock in the presence of a catalyst that resulted in BNNTs with 20-40 nm. Improved ball milling routes with the assistance of catalyst resulted in BNNTs with diameters at 60 – 100 nm and increased yield however no mention of BNNT amount produced was mentioned in the article.[196] Carbon substitution reaction [197] by using CNTs as the template, and catalytic chemical vapor deposition (CCVD) method that utilizes borazine as boron precursor in the presence of nickel boride catalyst [198].

The highly impure end product of the ball milling technique (BN sheets, flakes, and amorphous boron) and low yield of the techniques such as laser ablation and arc discharge pushed researchers to utilize CVD to synthesize BNNTs [199]. CCVD method enables simple, low-cost, and effective growth of the BNNTs. Following the success of the CCVD growth of the BNNTs, Tang *et al.* proposed a new CVD method that does not use any transition metal as a catalyst and uses carbon-free, inorganic boron precursors [200]. In this method, B_xO_y and catalyst vapors are produced via a reaction between the amorphous boron and catalyst, which is then reduced with the ammonia to generate BN growth vapors. BOCVD method allowed the high scale production of BNNTs at the temperature range of 1100 °C – 1300 °C with vertical induction furnaces. In their work, the yield of the BNNTs strongly depends on the temperature of the synthesis where if the temperature is low, the yield is in the order of milligrams whereas as the temperature increases the tube diameter also increases along with the yield. The need for a specialized furnace to fabricate the BNNTs via the BOCVD method and the high parameter sensitivity required for the synthesis [201] pushed researchers to find a novel system. Lee *et al.* [67] designed a growth vapor trapping CVD (GVT-BOCVD) method, which utilizes a commonly used tube furnace in combination with a one-end closed quartz test tube to synthesize BNNTs at 1200°C with obtained BNNTs showed diameters around 50nm (Figure 4.1). The yield for the synthesis is around 200 mg at 1500 °C and the authors suggested that an increase in reaction temperature can lead to a higher yield.

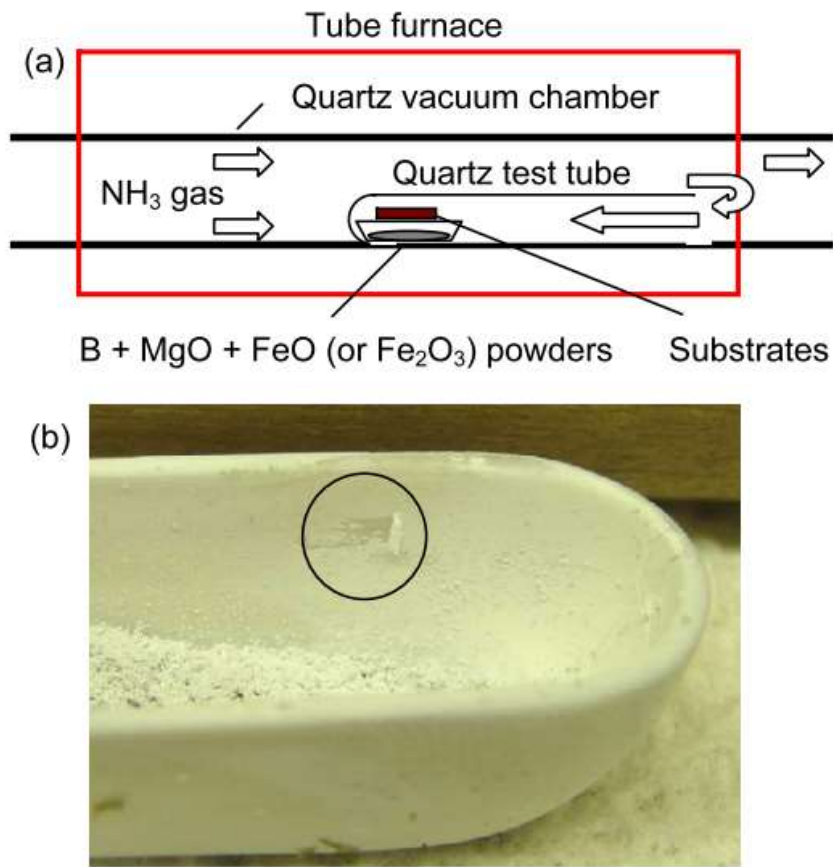


Figure 4.1 (a) Schematic of the experimental setup used by Lee et al. and (b) BNNT deposition on the walls of the alumina boat [67].

GVT-BOCVD method uses the theory of nucleation as the fundamental starting point. Researchers suggested a link between the nucleation of nanotubes and crystal growth.[70, 202, 203] This theory suggests that nucleation probability depends on equation one given below (Equation 4.1).

$$P_N = B \exp \left(- \frac{\pi \sigma^2}{k^2 T^2 \ln \alpha} \right) \quad (\text{Equation 4.1})$$

In this equation, P_N shows the whiskers nucleation probability, B is a constant, σ corresponds to surface energy of the catalyst, k is the Boltzmann constant, α is p/p_0 , (p is the partial pressure of growth vapors, p_0 is the partial pressure of the condensed phase at the equilibrium) supersaturation ratio and T is the temperature.

This equation defines three critical properties of the nanotube formation. First, P_N is proportional to $\exp\left(\frac{1}{T^2}\right)$ and indicates that when the growth temperature increases, the

probability of nanotube nucleation also increases. This can explain high BNNT yield in high-temperature synthesis. Second, the surface energy of the catalyst also affects the probability of nucleation for nanotubes. In BNNT synthesis, σ refers to the surface energy of the metal catalyst used (Fe_2O_3 in this study). The effectiveness of Fe_2O_3 catalysts can be linked to their surface energy. Lastly but most importantly, the nucleation theory states that supersaturation α and P_N are also directly proportional to each other. Supersaturation is directly dependent on the partial pressures of the growth vapors. As the partial pressures of the growth vapors increases, supersaturation also increases resulting in a higher probability of nucleation. In the growth vapor trapping-BOCVD method, using both one end-closed quartz test tube and Si wafers to cover alumina boat traps growth vapors, thus increasing their partial pressures. The increased partial pressure of growth vapors increases the supersaturation, which in turn increases the probability of nucleation. Increasing the supersaturation might also be used to decrease the temperature of growth. As explained before, high-temperature results in higher nucleation probability; however, keeping every other parameter constant and selecting a relatively low temperature with high supersaturation can also result in a high probability of nucleation, as stated in the equation. Of course, temperature also affects the partial pressure of the growth vapors since it directly affects the formation of the growth vapors. However, it can be suggested that, with constant growth temperature and constant surface energy, increasing the partial pressures of the growth vapors increases the probability of nucleation of nanotubes.

Although the synthesis methods mentioned earlier were successful in BNNT synthesis, their drawbacks, such as cost, scalability, hazardous nature, and complex fabrication process, prevented BNNTs from being viable filler material for industrial-scale applications. Even the CCVD method, the most used method for the fabrication of BNNTs, failed to elevate BNNTs to a position like CNTs where everyday applications can be enhanced.

The cost of the BNNT synthesis process mainly arises from the energy consumption, equipment, and precursors used. The CVD, as mentioned above systems synthesize BNNTs in temperatures between 1100°C to 1700°C [67, 200, 201, 204] which increases the cost of the synthesis considerably. Furthermore, increased temperature requires furnaces or reaction chambers specifically designed to withstand high temperatures or abrasive environments for scaling up from laboratory to industrial scales, which is costly

and complex. Efforts to lower the synthesis temperature resulted in the plasma-assisted chemical vapor deposition systems (PECVD) [205-207] that rely on plasma to energize BN growth vapors to increase the BN growth rate. Despite the lower temperature of these methods, the need for plasma also increases the cost of the method and hinders its scalability. Our limited market research to purchase BNNTs showed that the price of the BNNTs could vary, starting from 700\$ (unpurified) per gram to as high as 2400\$ per gram depending on the quality of the BNNTs. We believe that utilization of the BNNTs in various fields and applications can never be achieved if the cost of the BNNTs outweighs their usefulness.

As mentioned earlier, the first CCVD synthesis of the BNNTs was achieved by using borazine and ammonia borane precursors [198, 204, 208, 209]. However, these chemicals are highly hazardous to both humans as well as to the environment. In recent years, research efforts are directed towards green energy and production; the use of these chemicals for the synthesis of BNNTs is fundamentally hindering the future and the scalability of the material. Lately, the focus of the boron precursor has mainly been on the amorphous boron powder, which is also utilized in the GVT-BOCVD method as well as the BOCVD method. However, the cost of the analytical grade amorphous boron powder and the required production and purification process encourage the search for new boron precursors.

New synthesis techniques capable of producing large amounts of BNNTs have also been investigated. Pressurized vapor/condenser (PVC) method in which hot boron vapor (over 4000 °C) is condensed onto cooled metal wire where nitrogen gas nitrides the boron droplets. The technique yields BNNTs in the order of grams (120 mg/h) with a single or a couple of walls [210]. Fathalizadeh *et al.* introduced a high temperature, extended pressure inductively-coupled plasma system (EPIC) which is capable of producing BNNTs with a 35 g/h production rate [211]. This system is very similar to the synthesis technique developed by Kim *et al.* [212] in which they reported a production rate of 20 g/h with the difference being the use of hydrogen gas as a catalyst and the use of h-BN as a precursor (Figure 4.2). All of the methods mentioned above provide a high production rate for the synthesis of BNNTs however they also require high temperatures coupled with complex systems such as plasma torches and pressured reaction chambers.

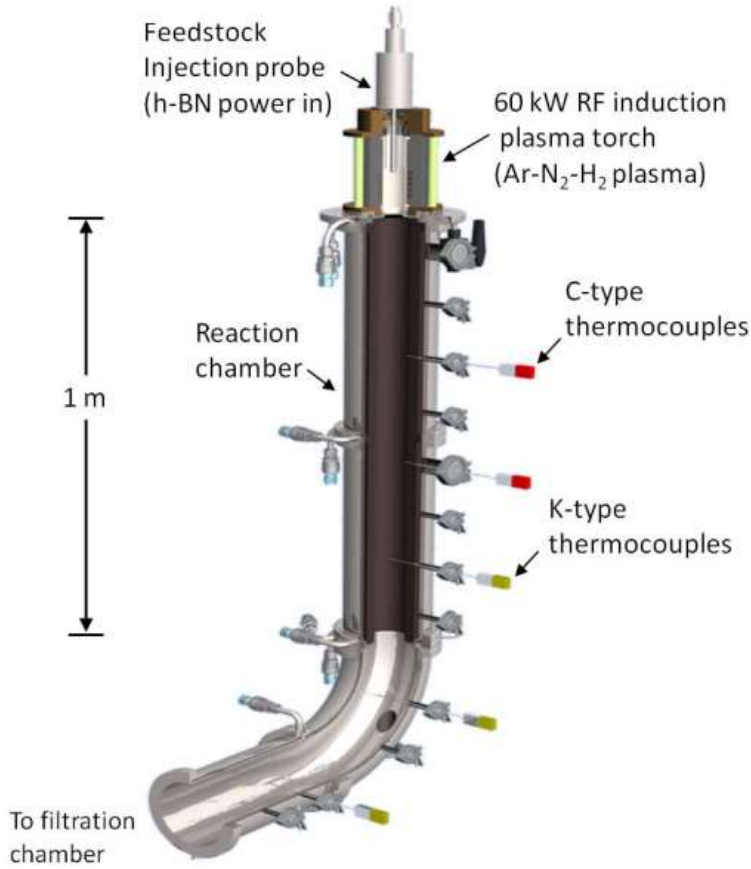


Figure 4.2 Schematic of induction plasma processing system designed by Kim et al. [212] excluding the filtration chamber.

The main decider in the BNNT synthesis depends upon the selection between the yield of the synthesis or the ease of production. As mentioned earlier, the high yield can be achieved via high temperature (GVT-BOCVD) or the use of complex systems (such as plasma-assisted chemical vapor deposition, arc-discharge, EPIC, *etc*) but the cost of the system also increases considerably.

There are quite a few syntheses strategies in the literature for the synthesis of BN nanostructures. Among these limited strategies, the use of different reactants, precursors and catalyst combinations have been reported for several CVD techniques as mentioned above. Besides, the use of sulfur compounds as a precursor has also been investigated; moreover, few details have been disclosed on the types of molecules used, reaction mechanisms, and effects on the final BN structures. A very high yield and good quality BN structures have been synthesized with the use of sulfur-containing molecules after the

decomposition of sulfur precursor molecules, and the deposition of intermediate products formed after deposition on the catalyst, followed by the reaction of boron with nitrogen on the catalyst containing sulfur [213]. Silva *et al.* showed the potential of FeS/Fe₂O₃ catalyst for the synthesis of boron nitride nanostructure synthesis. They proposed that the presence of sulfur prevents iron particles from growing and stay at satisfying dimensions [214]. Further investigations on the catalyst and BN synthesis investigating the effect of sulfur-containing molecules are noteworthy, and some of the these-molecules were explored here.

In this study, we propose a low-temperature BNNT synthesis that uses Colemanite, one of the widely used boron compounds with the chemical formula Ca₂B₆O_{11.5}H₂O having a B₂O₃ content of 40-50 %, as a boron precursor. Colemanite offers a safer, cheaper, and more environmentally friendly alternative as a boron precursor in BNNT synthesis via the GVT-BOCVD method. Kalay *et al.* [215] already showed that synthesis of BNNTs from Colemanite is possible at 1280°C by the CVD method. However, their method relies on high temperatures to synthesize BNNTs. In our work, we have shown that BNNTs can be synthesized at temperatures as low as 1050 °C with the assistance of sulfur-based molecules. This organic molecule allows a more efficient reduction of B₂O₃ to BN growth vapor, resulting in lower synthesis temperature for the BNNT synthesis. Low temperature allowed us to use inexpensive and straightforward furnaces to synthesize BNNTs and reduce the cost of energy. Moreover, we have also investigated Ulexite as well Etidot-67 boron minerals as a potential boron precursor. To the authors' knowledge, the use of colemanite as a BNNT precursor has only been used by Kalay *et al.* [215] without the assistance of any sulfur-containing molecules. Furthermore, evaluation of Ulexite and Etidot-67 minerals as boron precursors are unique to this study.

Following the successful synthesis of BNNTs, we have also shown a method to engineer the surfaces of the BNNTs with (Polytetrafluoroethylene) PTFE coating by using closed batch-initiated vapor deposition (CB-iCVD).

Theoretical and experimental studies on the boron nitride nanotubes (BNNTs) showed that they possess high piezoelectric coefficients in addition to their high radiation shielding, high mechanical strength, high chemical, and thermal stability even in elevated temperatures[216-218]. Lately, Kang *et al.* [219] reported a piezoelectric constant of $d_{33} = -4.71 \text{ pm/V}$ after orientation of BNNTs via stretching which is 460 % more compared to

the piezoelectric constant of neat polyimide. The same group also showed that the piezoelectric response is due to the presence of the piezoelectric response of BNNTs since stretched neat-PI showed no increase in piezoelectric constant. Furthermore, the group designed an actuator consisting of a CNT electrode layer and BNNT buckypaper layer that showed an extraordinary electroactive response. The same group also showed that the addition of BNNTs can also increase the piezoelectric constant of polyurethane in a similar study[220].

One of the most important factors determining the efficiency of the filler material on the final properties of the composites is the interface interactions between the filler material and the matrix [221]. In order to fully take advantage of the piezoelectric properties of the BNNTs, good interface interaction between polymer matrix is essential. Insufficient interface interactions can lead to piezoelectric and dielectric properties lower than theoretically expected. Yao *et al.* [221] showed that chelation of the interface can lead to a super-high piezoelectric coefficient, three times higher than traditional PZT-PVDF composites. Similarly, Zhang *et al.* [222] demonstrated increased piezoelectric performance when the surface of the BNNTs was functionalized chemically.

Moreover, the mechanical properties of the composites also heavily depend on the interface interactions between the matrix and the filler. Stronger interface interaction between BNNT and the polymer matrix can lead to superior load transfer capacity even without any surface modifications as shown with the comparison of BNNT-Epoxy and BNNT-PMMA composites [223]. The stronger interfacial strength of the epoxy-BNNT interfaces allowed better load transfer than the BNNT-PMMA composites with lower interfacial strength.

One of the drawbacks of the BNNTs is their inability to be dispersed inside an aqueous dispersion due to their strong van der Waals bonding and hydrophobicity resulting in agglomeration problems [224]. This inability to be dispersed in aqueous media prevents their further use as reinforcement material in composite materials. Functionalization of the BNNT surfaces has been proposed by the literature to overcome this problem mainly via covalent functionalization such as linking of stearoyl chloride chains [225], amine groups [226, 227], hydroxyl groups [228], and polyhedral oligosilsesquioxane (POSS) [123]. Another method that has been utilized is the non-covalent functionalization of the BNNTs in which BNNTs can interact with polymers via μ - μ stacking. Taking advantage

of this property, researchers have wrapped PmPV [229](poly[m-phenylenevinylene-co-(2,5-dioctoxy-p-phenylenevinylene)], glycol-chitosan [230], PEI (polyethyleneimine) [231, 232] and PLL (poly-l-lysine) [233].

Lately, a new method to functionalize nanostructures has been proposed by the literature. Initiated chemical vapor deposition (iCVD) is a solvent and radical free, in situ polymerization method that enables conformal polymer coating of the substrates as well as nanostructures at low temperatures [234]. Several research groups have used iCVD to improve the functionality of the nanostructures such as the creation of superhydrophobic surface by coating vertically aligned CNTs with PTFE [235], deposition of epoxy on the multi-walled carbon nanotubes (MWCNTs) to allow transferring of the functionalized MWCNTs [236].

In this study, we have evaluated a new possible non-covalent functionalization of the BNNTs via CB-iCVD. Our aim was to provide proof of concept that, a matrix polymer can be deposited on the surface of the BNNTs before loading it into the polymer matrix to provide better interface interactions and prevent agglomerations. To this end, we have collaborated with Ince research group to conformally coat our as-synthesized BNNTs with PTFE. Our results showed that CB-iCVD can be utilized to conformally coat the surface of the BNNTs to provide functionalability to them.

4.2 Experimental

4.2.1 Chemicals and Equipment Used

Colemanite ($\text{Ca}_2\text{B}_6.5\text{H}_2\text{O}$)($\sim 45\text{ }\mu\text{m}$) was provided by Eti Mine Works General Management (Turkey), Iron (III) oxide (nanosize), and thiophene was purchased from Sigma-Aldrich, ammonia gas (5.0)was bought from Linde Gas A.Ş. Reactions were carried out using PFT 15/50/450 Protherm tube furnace, 0-1 slpm Alicat flowmeter, 0-

500 sccm Alicat flowmeter with corrosive gas resistance. L-cystine ($C_5H_{12}N_2O_4S_2$, 99+, MW: 240.30) and L-Methionine ($C_5H_{11}NO_2S$, 99+, MW: 149.21) were purchased from CHEM-IMPEX International and used without further purification.

For the characterization of the as-synthesized products we have utilized, Jeolden JEM-200CFEG UHR-TEM CS corrected equipped with Garanti Quantum GIF, Thermo Scientific iS10 FTIR with ATR accessory, Renishaw inVia Reflex Raman Microscopy, and Spectrometer (532 nm laser unite), Zeiss LEO Supra 35VP FESEM, Cressington Sputter Coater, 108 auto.

4.2.2 Synthesis of BNNTs via GVT-BOCVD method

In a typical synthesis, Fe_2O_3 catalyst and unprocessed Colemanite were mixed with a vortex mixer with a weight ratio of 12:1 (Colemanite: Fe_2O_3). After the homogeneous mixture was achieved, 2 mL of thiophene was added to catalyst/colemanite followed by secondary vortex mixture to ensure liquid thiophene was sufficiently distributed inside the solid mixture. The prepared mixture is then transferred to an alumina boat and covered with silicon substrates (Figure 4.3 a.). Alumina boat is then placed at the closed end of the quartz test tube (45 cm length, 36 mm diameter) that is placed on the stable zone of the tube furnace (Figure 4.3 b.)

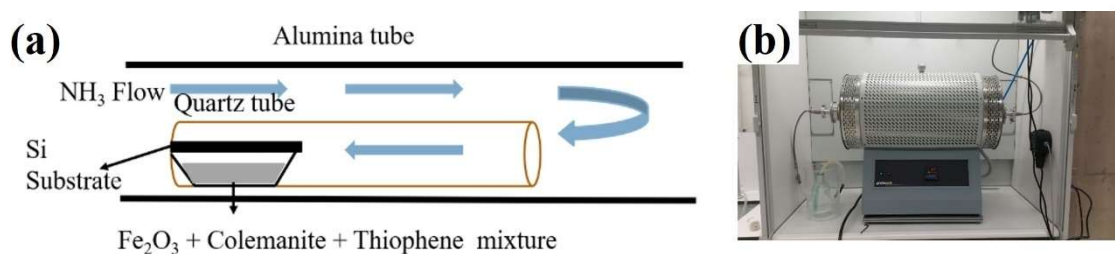


Figure 4.3 (a) The schematic representation of the reaction chamber for the BNNT synthesis. (b) Furnace system used in the BNNT synthesis.

The synthesis started with the vigorous purging step to get rid of any oxygen gas inside the furnace. The system was vacuumed to 0.5 mbar, followed by 1000 sccm Ar flow. This

step was repeated two times for each synthesis process. Following the purging step, the system was heated to 1050 °C with a heating rate of 5 °C/min under an ammonia atmosphere and kept at this temperature for two hours. When the desired reaction time had been achieved, ammonia flow was replaced by Argon flow immediately to ensure excellent control of the reaction time. One of the critical parameters in this process is the control of the cooling rate of the system. If the furnace is allowed to cool down to room temperature naturally, we have observed glassy compounds trapping both the BNNT product and the Si wafers inside it. This trapping behavior is expected since Colemanite is also commonly used in glass fabrication processes. The furnace was cooled down in a controlled manner with a - 2 °C/min cooling rate to avoid a possible glass formation. A white powder was collected mainly on the silicon substrate's surface and the alumina boat's walls. No further purification step was conducted on the BNNTs collected on the surface of the silicon substrate.

4.2.3 CB-iCVD Deposition of PTFE on the Surface of the As-synthesized BNNTs.

Deposition of the PTFE films on the surfaces of the BNNTs was achieved using CB-iCVD with hexafluoropropylene as the monomer and perfluorobutane sulfonyl flouride as the initiator.

In an iCVD deposition process, both the initiator and the monomers are fed into a reaction chamber in a vapor phase. The initiators are then activated into radical species by a filament heated around 150 °C to 300 °C. These radical species then react with the condensed monomers on the substrate to start free radical polymerization of the intended film coating [237]. Unfortunately, this method has a high precursor consumption and low throughput drawbacks making it less desirable for large-scale applications [238]. The alternative approach that our collaboration group, CB-iCVD, has reported offers a cost-effective alternative to CF-iCVD which can be used to deposit PTFE on nano-size substrates.

As opposed to continuous-flow iCVD (CF-iCVD), the CB-iCVD both the monomer and initiator are trapped inside the reaction chamber instead of constantly flowing into it. This allows precursors to be kept inside the chamber through the total deposition time, decreasing the number of unreacted precursors. The deposition system consists of a baffle plate, heated filaments, a sample stage, a vacuum, and a quartz window to observe the process (Figure 4.4).

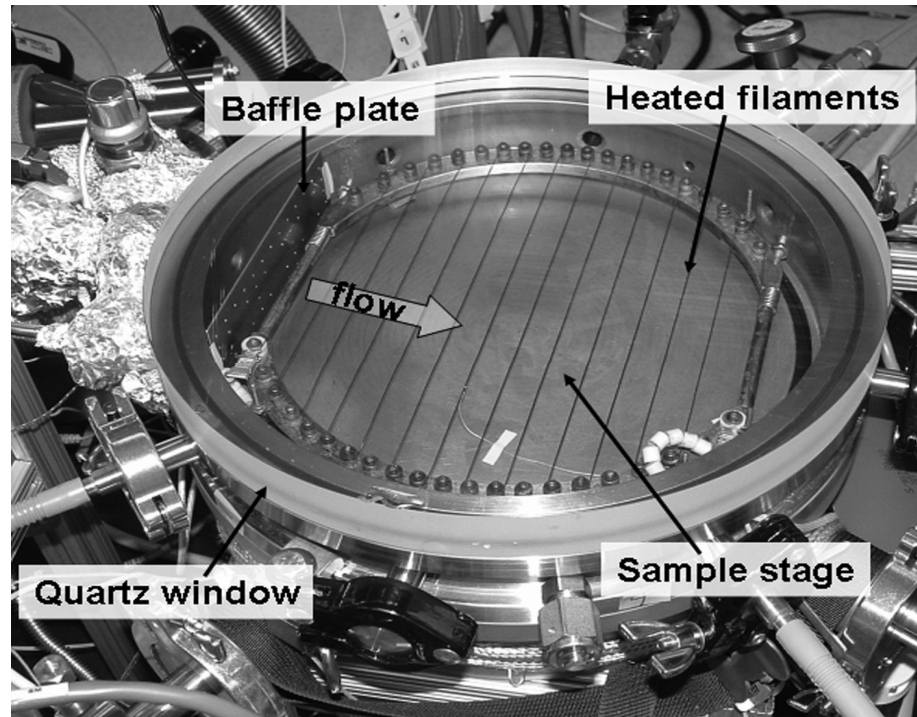


Figure 4.4 Photograph of the CB-iCVD setup we have used for the deposition of the PTFE.

The kinetics of the iCVD process was evaluated by Lau *et al.* [239] where they showed the kinetics of the polymerization in eight steps. They reported that first the initiator molecule is thermally decomposed due to heat from filaments into primary radicals, followed by the absorption of the primary radicals and monomers to the cold substrate. The primary radical then initiates the polymerization by reacting with the monomer. As the monomer absorption to the substrate continues, the polymerization propagates. Finally, the polymer propagation is terminated via recombination, coupling, or disproportionation.

During the coating of the BNNTs, we have selected the optimized deposition parameters reported in the literature by our collaborative group [238]. In summary, we have

evacuated the reaction chamber until we have reached 5 mTorr. Following this, we have fed the monomer into the reaction chamber until we have reached 1 Torr, followed by the introduction of the initiator until the pressure reached 3 Torr. When the monomer and initiator feeding was completed, we have closed the exhaust to prevent any unreacted precursors from escaping the chamber. The filament was then heated to 300 °C and the polymerization was allowed to continue for two minutes. The polymerization was terminated by opening the exhaust valves to allow unreacted precursors to leave the reaction chamber. The same process was repeated 3 times to achieve optimum conformal coating on the BNNTs.

4.3 Results and Discussion

Our research group has previously investigated the potential of boron minerals such as Etidot-67 and Ulexite as boron precursors in BNNT synthesis. Kalay *et al.* [215] have reported the synthesis of BNNTs by Colemanite earlier with a high-temperature CVD process. In this approach, we have extended our research to boron precursors such as Ulexite and Etidot-67 with the same catalyst ratio fixed to 12:1 at 1280 °C and 120 minutes of reaction time as a starting point [232].

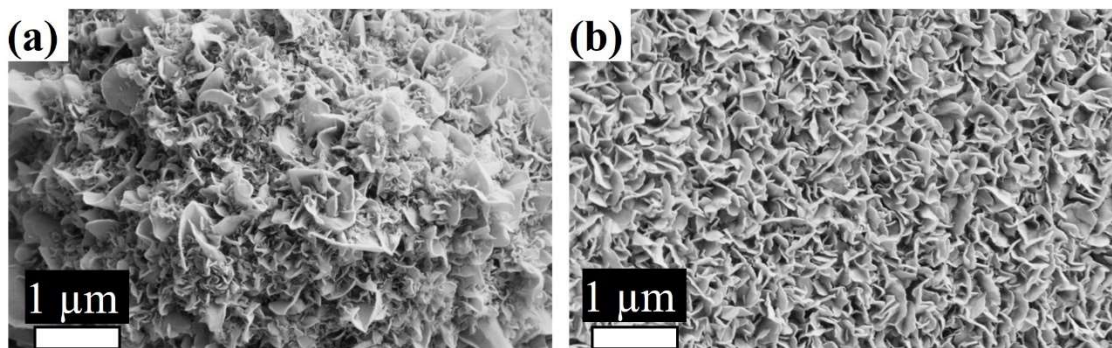


Figure 4.5 SEM images of the synthesis products when (a) Ulexite and (b) Etidot-67 was used as boron precursors.

Although, SEM image of white product collected from the walls of the alumina boat after the BNNT synthesis from Ulexite (Figure 4.5. a) shows no BNNT formation, BN-catalyst clusters similar to the initial phase for the BNNT synthesis were observed, which was similar to products reported earlier [215]. BNNTs synthesized from Etidot-67 also presented similar structures at SEM images (Figure 4.5 b), where BN-Fe initial phase clusters are present without any BNNT formation. Although no BNNT formation was achieved on these syntheses, the existence of the initial phase motivated us to further work on the BNNT synthesis from boron minerals. To this end, we have investigated possible molecules that can enhance the efficiency of the synthesis. The main goal of this research was to evaluate the potential of boron minerals as boron precursors and determine the lowest possible synthesis temperature to explore its potential to be used for the large-scale BNNT synthesis process with the assistance of sulfur-containing compounds. Further studies have been focused on decreasing BNNT growth temperature 1200 °C and below, still initially focusing on Colemanite as a boron precursor in the presence of sulfur-based compounds to trigger the synthesis at lower temperatures. These studies then were extended to other boron precursors such as Ulexite and Etidot-67.

4.3.1 BNNT Synthesis from Colemanite Mineral

SEM image shown in Figure 4.6 a. indicates the successful BNNT synthesis from Colemanite at 1200°C. Each BNNT cluster appears to be originating from one starting

point, supporting the VLS theory that has been proposed for the synthesis of BNNTs via the CVD method [240]. Furthermore, VLS theory also suggests that the size of the catalyst droplet affects the tube diameter directly. This behavior could also be observed by the presence of high diameter BNNTs along with the small diameter BNNT clusters. These big BNNTs can reach a couple of micrometers in diameter, and they do not originate from the same catalyst droplet as the small diameter nanotube clusters.

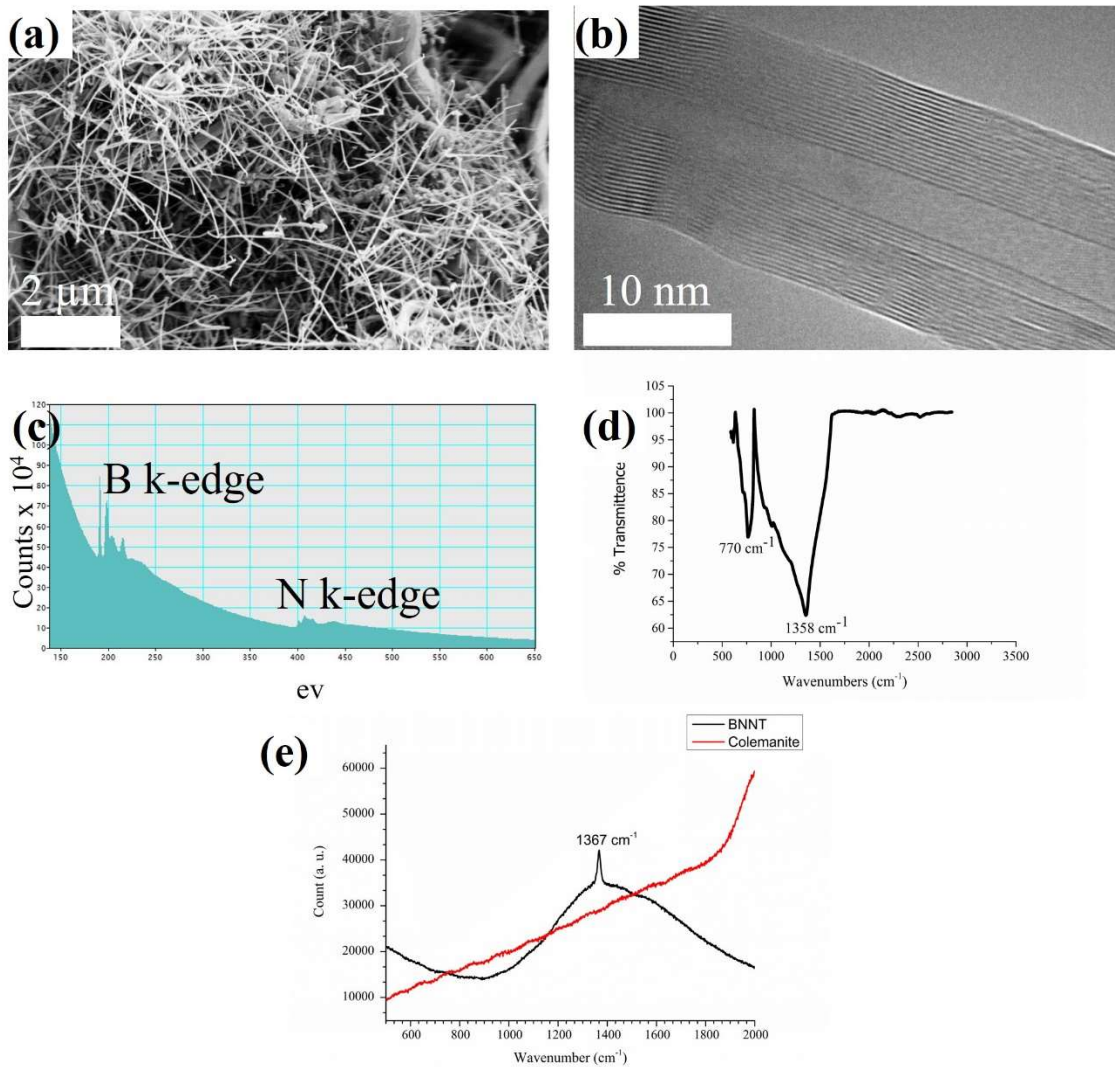


Figure 4.6 (a) SEM image of the BNNT clusters collected on the Si wafers at 1200 °C synthesis temperature. (b) TEM image of the single BNNT synthesized at 1200 °C showing hollow center and darker walls. (c) EELS of the single BNNT with distinct B and N edges, (d) FTIR spectrum of the BNNTs, (e) RAMAN spectrum of the Colemanite and BNNTs.

It was clearly depicted that the smaller diameter BNNT clusters with an average diameter of 45 ± 10 nm (calculated from 20 different BNNT diameters) are the main product of the synthesis. Unlike previously reported BNNT morphologies, these nanotubes do not show characteristic morphologies of the bamboo-like nanotubes [241-243]. The TEM image taken from BNNT synthesized at reaction temperature 1200 °C (Figure 4.6 b.) shows the characteristic tube morphology of the BNNTs. The brighter center and the parallel aligned darker fringes correspond to the hollow center of the nanotubes and the multiwall of the BNNTs, respectively. The BNNTs appear to have ~ 15 nm diameter with 6 nm walls and 2 -3 nm center diameter. The distance between walls is ~ 0.35 nm for the nanotubes, which is in line with what is reported in the literature for inter wall distance of h-BN [244]. Profile analyses indicate that BNNT is multi-walled with 12 walls.

The electron energy-loss spectroscopy (EELS) spectrum (Figure 4.6 c.) confirms the BN composition of the nanotubes with pronounced K edges of B and N at 188 and 401, respectively [244]. Furthermore, the presence of the μ^* - peak confirms the sp^2 hybridization of the B and N atoms that is expected [244]. The FTIR spectrum (Figure 4.6 d.) of the as-synthesized BNNTs shows the characteristic ~ 1358 cm^{-1} and ~ 770 cm^{-1} absorption bands, representing the plane stretching mode of h-BN and out of plane radical buckling mode of BNNTs [245]. Moreover, the longitudinal optical mode of the h-BN that corresponds to stretching of the h-BN sheets along the tangential directions can be observed at 1530 cm^{-1} as a shoulder peak [246]. Two additional peaks showed in 700 cm^{-1} and 1006 cm^{-1} can be attributed to the C-S bond in the thiophene ring [247] and Si-O-Si stretching vibrations originating from Si wafer substrate, respectively[248]. RAMAN spectrum of the BNNTs on the Si wafers (Figure 4.6 e) shows distinct h-BN E_{2g} vibration of the BN structure, further verifying the chemical structure of the tubes [249]. The broad peak on the RAMAN spectrum between 1000 cm^{-1} to 1800 cm^{-1} is caused by the thick and dense BNNT layer formation on the Si wafers and has been used to calculate BNNT layer thickness in the literature [250].

4.3.2 Temperature Optimization of the BNNT Synthesis

After the successful BNNT synthesis, we investigated the lowest possible BNNT synthesis temperature required. The catalyst ratio, reaction time, flow rate, and thiophene amount as kept constant, and only the reaction temperature was changed between the experiments. The results show that BNNTs can be synthesized at temperatures as low as 1050 °C with good quality. Although the synthesis temperature was the lowest, the diameter of the BNNTs remained similar, with 62 ± 20 nm. Increasing the reaction temperature to 1100 °C resulted in larger nanotubes with diameters 94 ± 30 nm (Figure 4.7 b.), a trend not followed when the synthesis temperature was further increased to 1150 °C. Figure 4.7 c. shows the synthesis product synthesized at 1150 °C, where the diameter of the BNNTs again drops down to 45 ± 25 nm. We believe that the delicate balance between BN vapor generation and catalyst droplet formation resulted in higher diameter BNNTs for 1100 °C. However, after increasing the temperature to 1150 °C and above, the number of catalyst droplets and the BN vapor concentration equilibrates to produce lower diameter BNNTs. The most striking difference between synthesis temperatures can be seen clearly by comparing BNNTs synthesized at 1050 °C (Figure 4.7 a) and 1200 °C (Figure 4.7 d.). As the synthesis temperature increases, the density of the BNNT bundle also increases considerably. Although the diameter and the morphologies of the BNNTs stay similar, the denser BNNT cluster is present at 1200 °C synthesis. We theorize that the BNNT bundle density increases when the temperature is increased from 1050°C to 1200 °C due to more efficient BN vapor production reactions that increase the amount of BN growth vapors diffusing into the catalyst droplet.

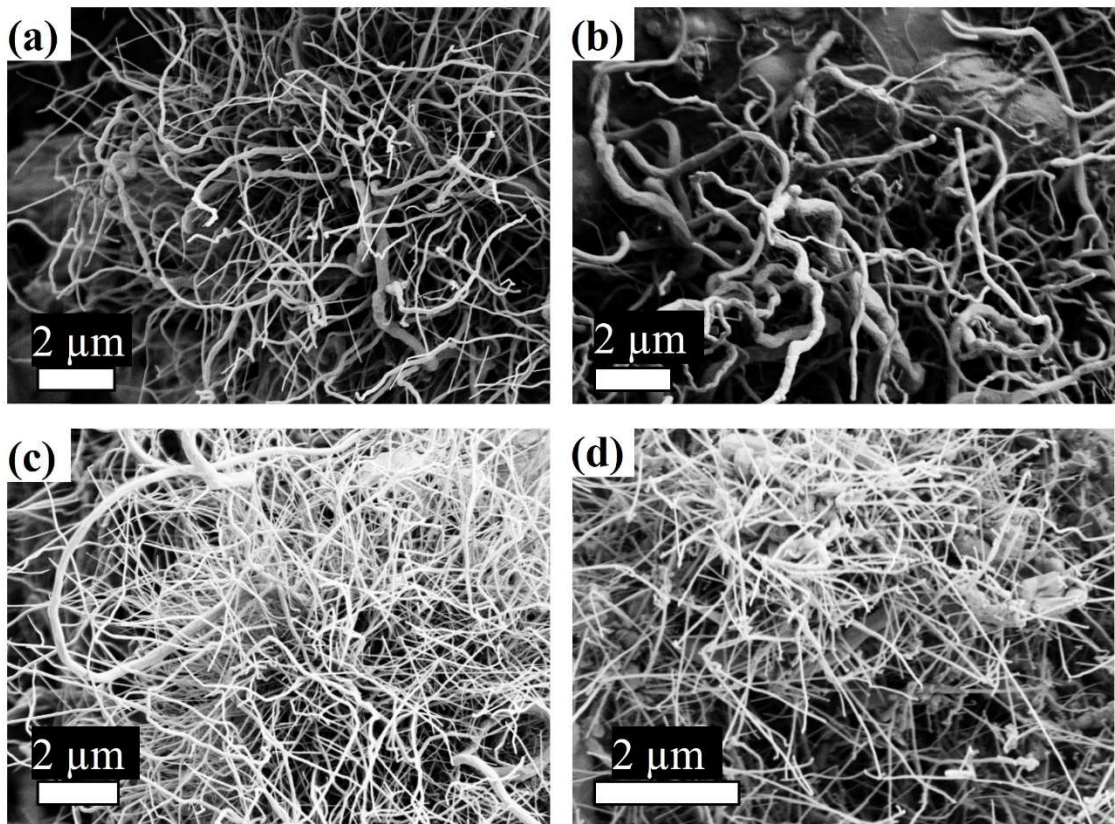


Figure 4.7 SEM images of the BNNTs synthesized at (a) 1050 °C, (b) 1100 °C, (c) 1150 °C, and (d) 1200 °C.

Although the yield of the BNNT synthesis drops, the cost and the potential scalability of both synthesis routes should also be considered. According to the heat equation,

$$Q = m \cdot C_p \cdot (T_2 - T_1) \quad (\text{Equation 4.2})$$

where Q represents the amount of heat required to increase the temperature of the (m) amount of material with (C_p) thermal capacity from initial temperature (T_1) to final temperature (T_2), 20 % more heat is required to achieve 1200 °C than 1050 °C. Furthermore, Stefan Boltzmann's law states that the total radiant heat power emitted from the surface of a material increases with the fourth power of the temperature of the material [251]. It can be inferred from the law that as the temperature of the furnace increases, the amount of heat loss from openings and inefficient insulation will become more significant with the power of 4. On a laboratory scale, this does not result in meaningful energy consumption; however, if large-scale production of the BNNTs is considered, the energy

loss due to blackbody radiation would be one of the challenges that need to be addressed. Moreover, the design and the quality of insulation differ significantly for high-temperature furnaces such as tube furnaces to lower-temperature furnaces such as split furnaces. The type of the furnace carries significant importance when it comes to the scalability and research of the BNNTs. The proposed synthesis method can be applied to furnaces readily available for CNT research with minimal modification, whereas higher temperature synthesis methods require specialized furnaces for the BNNT synthesis [67, 199, 208].

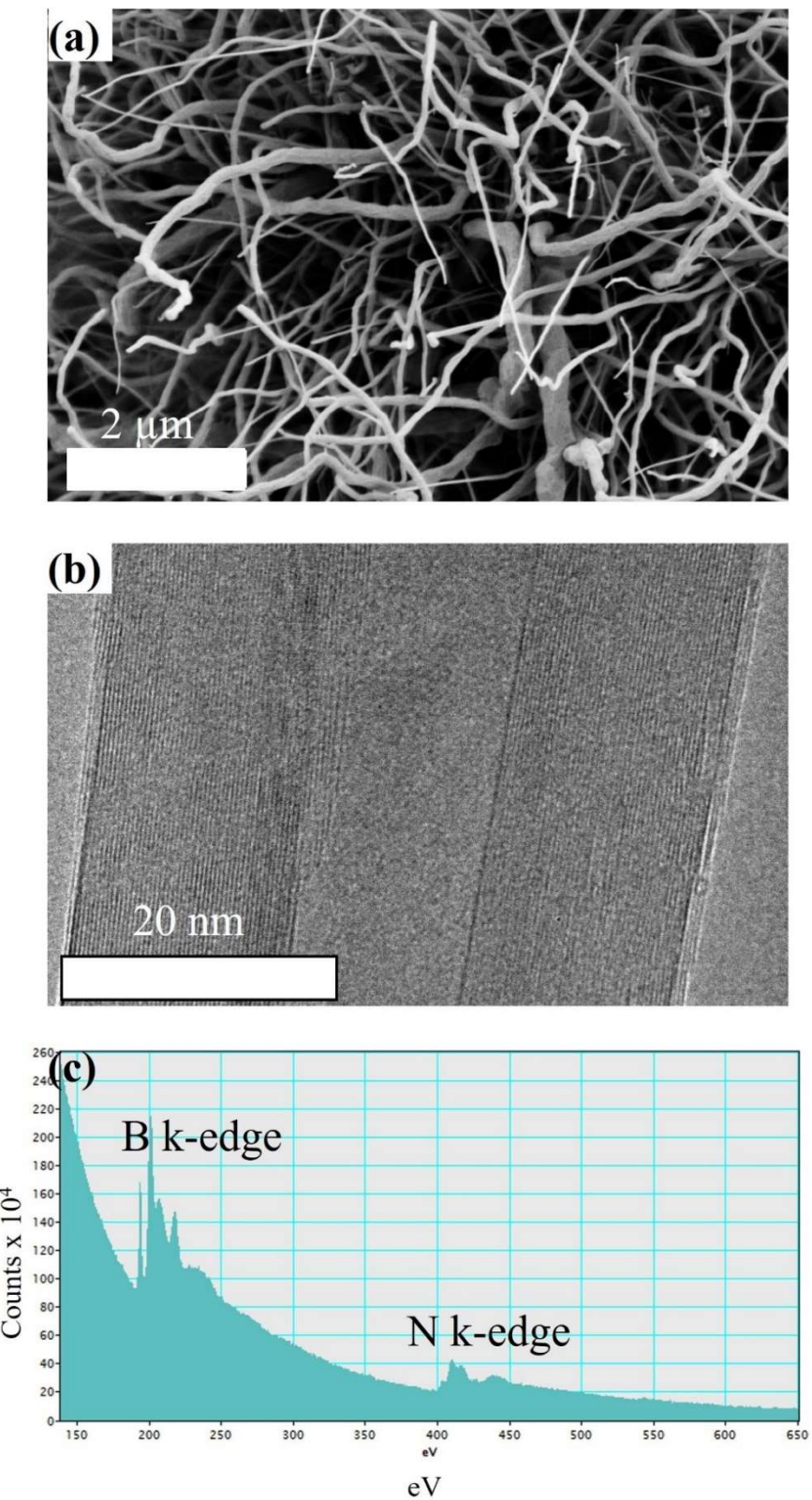


Figure 4.8 (a) SEM image of the BNNTs synthesized at 1050 °C, (b) TEM image of single BNNT with a hollow center, (c) EELS of the BNNT showing the characteristic B and N edges.

Further characterization of the BNNTs synthesized at 1050 °C were conducted to confirm tube morphology and compare the quality of the BNNTs to those synthesized at 1200 °C. SEM image of the BNNTs (Figure 4.8 a.) shows similar tube morphology to 1200 °C with tube diameter in the range of 50-100 nm. As encountered at 1200 °C synthesis temperature, these nanotubes are also clustered and appear to be originating from one central point in accordance with VLS theory. TEM image (Figure 4.8 b.) of the single BNNT has a hollow center and dark fringes, an indicator of the tube morphology for the BNNTs. The tube diameter was measured to be ~45nm with 15 nm wall thickness and 12 nm hollow center diameter. The distance between the walls was measured to be the same as 1200 °C (~0.35 nm), similar to literature [244]. Profile analysis of the tube indicated that BNNT has 35 walls, higher than the number of walls observed at 1200 °C (12 walls). EELS data (Figure 4.8 c.) showed similar results for the BNNTs synthesized at 1050 °C, in which both B and N K-edges are present in the spectrum. The characterization results propose that lowering the temperature from 1200 °C to 1050 °C of the synthesis only led to a higher number of walls and insignificant diameter increase but caused no drastic change in the structure and quality of BNNTs. Considering these results, we believe that lowering the temperature to 1050 °C can offer more advantages in cost and scalability than the minor disadvantages such as higher wall number and lower yield.

4.3.3 The Efficiency of the S-Based Molecules

To highlight the effect of the thiophene and investigate other sulfur-based molecules, we have designed an experiment in which one synthesis was started without any thiophene addition, one was started with L-cystine, and finally, one was started with the addition of L-Methionine. Each of the syntheses was run at 1050 °C with a reaction time of 120 minutes. The sulfur molecules were added to the catalyst mixture with a molar ratio of 2:1 (S molecule/Fe₂O₃). The chemical structures of the molecules can be seen in Figure 4.9.

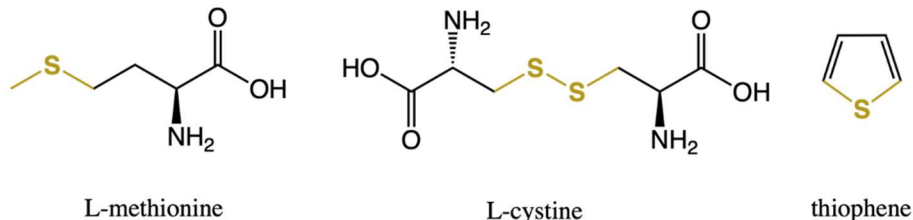


Figure 4.9 Chemical structures of the S-based molecules used in the BNNT synthesis.

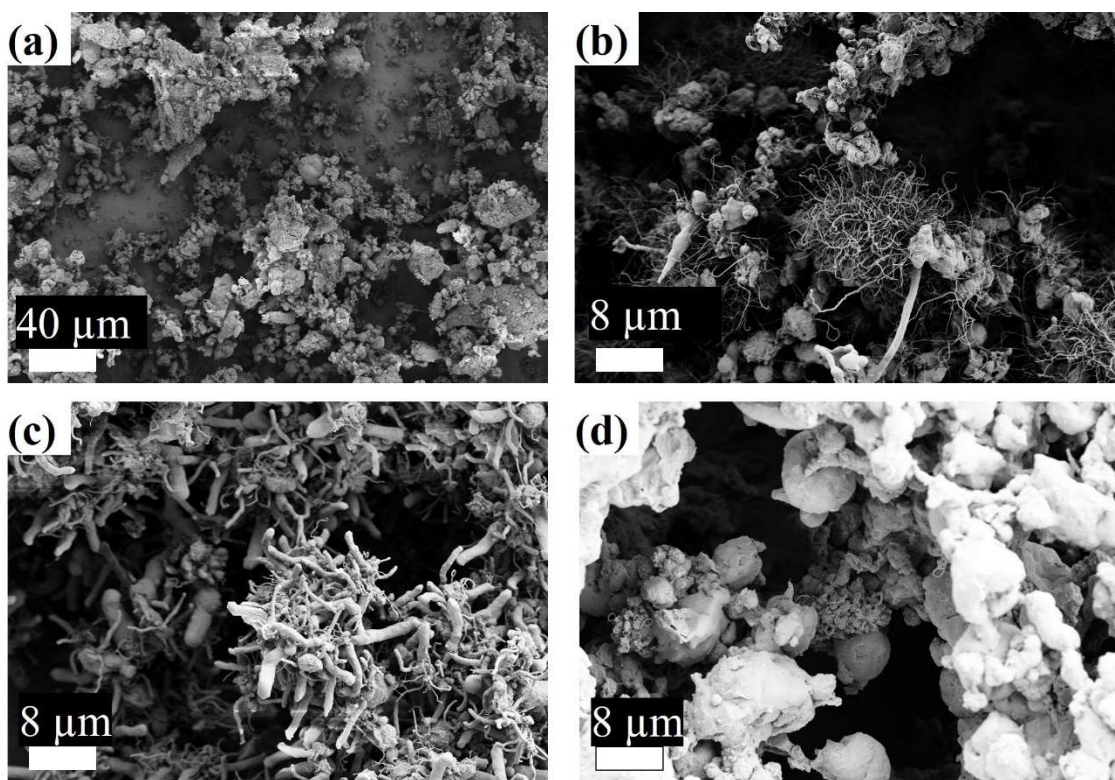


Figure 4.10 SEM images of the products synthesized (a) without any S-based molecule, with (b) thiophene, (c) L-cystine and (d) L-methionine

SEM images of each synthesis presented a different effect on the yield of the BNNT synthesis for each S molecule. When no S-based molecule was added to the catalyst mixture, no BNNT formation was observed at 1050 °C (Figure 4.10 a.). When thiophene was added to the catalyst mixture, BNNT clusters began to form, and they can be seen at the SEM image covering the surface of the Si wafer (Figure 4.10 b.). When the S-based molecule was changed to L-cystine, the formation of the BNNTs was achieved; however, the length of the BNNTs was shown to be shorter compared to thiophene-based BNNTs with large diameter BNNTs dominating the product (Figure 4.10 c.). Although small diameter BNNTs are also visible in the SEM image, further optimization of this system

is required to increase the quality of the BNNTs. Out of all S-based molecules, L-methionine performed the worst, with only the start of the BNNT formation is visible in a minimal amount; it can be considered insignificant (Figure 4.10 d.). We theorize that there can be two possible reasons behind the different effects of the different S molecules. (1) Thiophene exists in a liquid state at room temperature due to its low vapor pressure and thus can mix homogeneously with the catalyst mixture to ensure better wetting. (2) differences in decomposition chemistry of the sulfur-based compounds.

In this work, we selected two amino acids as the sulfur-based compounds, release several gaseous small molecules when they decomposed at elevated temperatures. In their article, Yablokov et al. [252] have investigated and explained thermal decomposition kinetics and byproducts of sulfur-containing amino acids, including L-methionine and L-cystine. L-methionine starts melting and decomposes gaseous molecules at 281 °C and L-cystine at 260 °C. Based on their findings, under their experimental conditions, Yablokov et al. showed that L-methionine decomposes into CO₂ (55.3 mole %), CH₃SH (41.9 mole %), H₂S (1.2 mole %) and nitrogen, ammonia, (CH₃)₂S, (CH₃)₂S₂. The primary decomposition product is CO₂, and it does not deposit onto catalyst molecules to further promote BN structure formation. Through these findings, the lowest yield and low-quality BNNTs production in the presence of L-methionine with a high amount of CO₂ as one of the decomposition products were clearly explained. CO₂ could contribute to growth vapor pressure, but it does not promote BNNT growth due to the lack of interactions with the catalyst. The second highest decomposition product is CH₃SH which is expected to interact with the minerals and deposit on them to contribute to BNNT growth.

On the contrary to L-methionine gaseous decomposition, the product composition of L-cystine is in favor of the sulfur molecules. L-cystine decomposes into H₂S (97.93 mole %), CO₂ (0.32 mole %), C₂H₅SH (0.5 mole %), thiophene (0.31 mole %), and acetonitrile (0.31 mole %), as major volatile compounds [252]. More than 99 % of the volatile decomposition compounds contain sulfur atoms. These results support our findings that a higher amount of sulfur-containing gas mixture support BNNT synthesis. We observed a low aspect ratio but a good amount of BNNT formation with L-cystine due to volatile sulfur-containing decomposition compounds.

Moreover, thiophene is a five-membered aromatic compound that contains a sulfur atom, and the thermal decomposition behavior of thiophene was studied experimentally and

theoretically [253] Vasiliou et al. have shown that unimolecular decomposition of the thiophene could follow five different reaction mechanisms. Two of these possible mechanisms are analogous to furan pyrolysis which yields, $S=C=CH_2 + HC\equiv CH$ and $CS + HC\equiv CCH_3$. Another two mechanisms are explained as unique to the thermal decomposition of thiophene, and these paths yield $HCS + HC\equiv CCH_2$ and $H_2S + CH\equiv C-C\equiv CH$ as the stable decomposition products. A fifth mechanism yields elemental S and $CH\equiv C-CH=CH_2$ is explained as unlikely due to the high energy barriers that require higher temperatures. According to the given decompositions products of the mechanism above, the most stable and energetically feasible sulfur compounds, i.e., hydrogen sulfide (H_2S), thioketene ($CH_2=C=S$), thioformyl radical (HCS), could be explained as the primary contributor to the BNNT growth at lower temperatures. However, further studies are needed to confidently demonstrate their role in the low-temperature synthesis with the assistance of sulfur-containing compounds as growth vapors.

The addition of the sulfur to the reaction atmosphere allows the formation of FeS via reaction between Fe_2O_3 with hydrogen sulfide according to the reaction provided below:



According to Reshetenko *et al.* [254] iron oxide catalyst undergoes reduction reaction and forms iron sulfide. As mentioned earlier, FeS has been theorized to retard the particle growth of the Fe particles, allowing more efficient catalyst activity for the catalyst. A similar effect is also encountered in CNT synthesis where F – FeS eutectic serves as a nucleation site for CNTs [255]. We believe that increased catalyst efficiency of the Fe_2O_3 due to the presence of FeS allows the low-temperature synthesis of the BNNTs.

4.3.4 Synthesis of BNNTs from Ulexite and Etidot-67 Minerals

Similar to Colemanite, Ulexite ($NaCaB_5O_6(OH)_6 \cdot 5H_2O$) and Etidot-67 ($Na_2B_8O_{13} \cdot 4H_2O$) boron minerals that contain a high amount of B_2O_3 in their structure. In order to evaluate

their potential as boron precursors for BNNT synthesis, we replaced Colemanite in our synthesis with each of them and characterized the resulting product. Table 4-1 shows the chemical composition of the Colemanite, Ulexite, and Etidot-67 minerals used in the BNNT synthesis.

Table 4-1. Chemical composition of the boron minerals used in this study. (*: in ppm)

Mineral	B ₂ O ₃ (%)	CaO (%)	SiO ₂ (%)	Al ₂ O ₃ (%)	SrO (%)	MgO (%)	Na ₂ O (%)	SO ₄ (%)	Fe (ppm)	Fe ₂ O ₃ (%)	Cl (ppm)	As (ppm)	Moisture (%)
Colemanite	40	26.8	5.0	0.25	1.15	2.7	0.15	0.3	-	0.04	-	25	0.3
Ulexite	37	18	3	0.1	0.6	1.6	4	0.2	-	-	-	30	0.2
Etidot-67	67	-	-	-	-	-	15	500 *	9	-	75	-	-

The synthesis conditions were chosen exactly as the BNNT synthesis from the Colemanite mineral with Colemanite replaced by the respected mineral. The synthesis was carried out at 1050 °C and 1200 °C with the Fe₂O₃ and thiophene catalyst mixture.

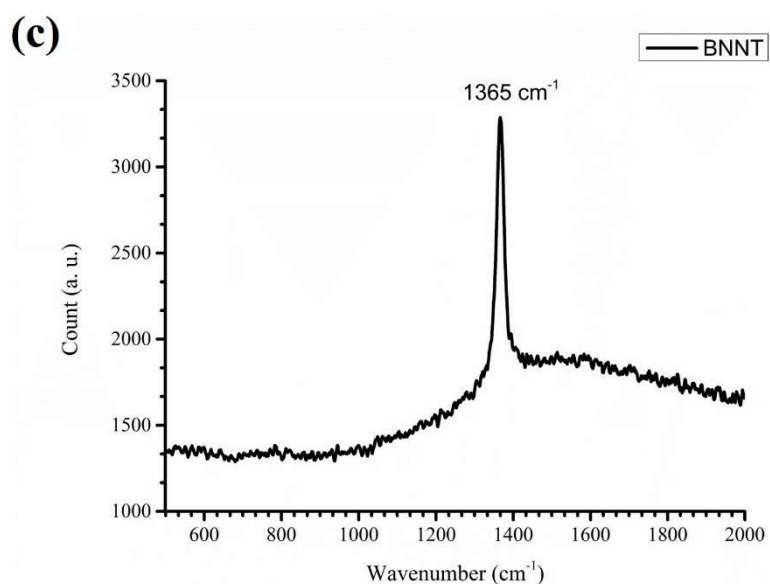
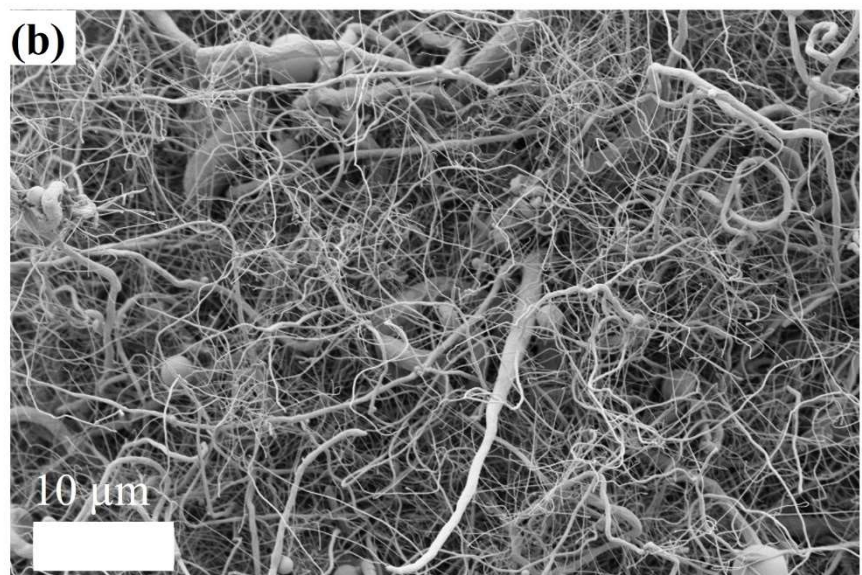
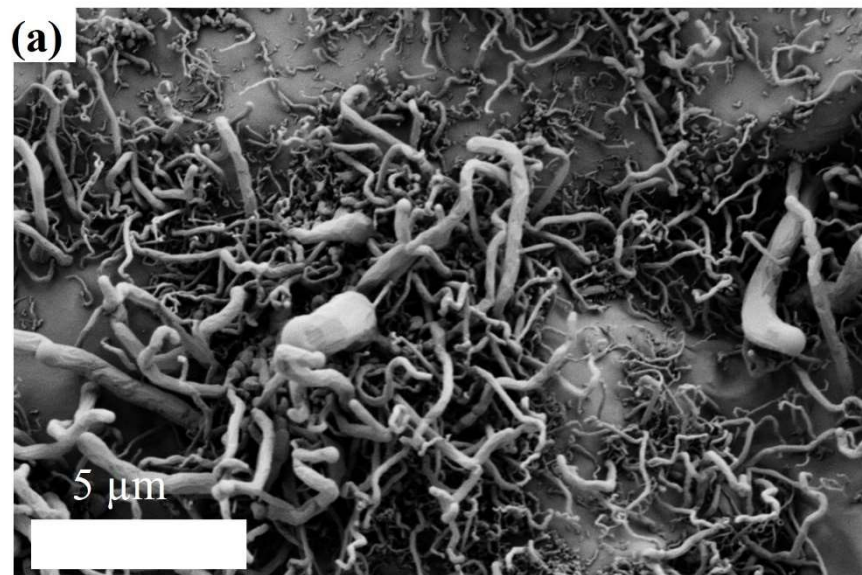


Figure 4.11 SEM images of BNNTs synthesized with Ulexite precursor at (a) 1050 °C and (b) 1200 °C. (c) RAMAN spectrum of the BNNTs.

When Ulexite was chosen as the boron precursor, BNNTs with heterogeneous diameter distribution can be collected on the silicon wafers at 1050 °C (Figure 4.11. a). Like Colemanite-based BNNTs, these BNNTs are bundled together and appear to originate from a single catalyst droplet. However, the diameter of these tubes appears to be higher (100 ± 50 nm) than their Colemanite counterparts, and the yield appears to be lower. Different calcination characteristics of the Ulexite can explain this compared to Colemanite. Şener et al. [256] showed that during calcination of the Ulexite mineral, Ulexite loses its crystal water slowly, resulting in the porous structure as opposed to Colemanite which experiences abrupt crystal water loss that leads to particle size reduction. Smaller particle size enhances the BN growth vapor production reaction, which results in higher quality BNNT growth at 1050 °C for the Colemanite compared to Ulexite. When the reaction temperature increased to 1200 °C, Ulexite became a suitable boron precursor for BNNT synthesis with a lower diameter ($\sim 80 \pm 40$ nm), and a higher yield product can be observed on the SEM images (Figure 4.11. b). This behavior can be attributed to the higher nucleation probability arising from higher temperatures. RAMAN spectrum of the BNNTs (Figure 4.11. c) also showed the characteristic h-BN peak at 1365 cm⁻¹, confirming the h-BN structure of the tubes [249].

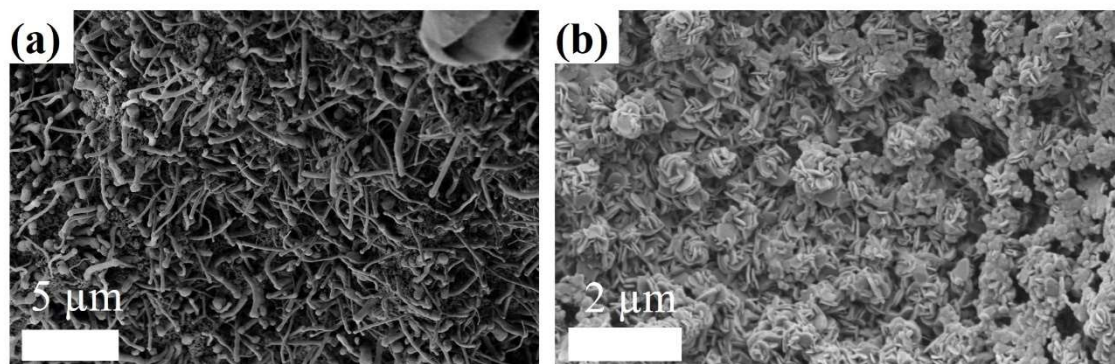


Figure 4.12 SEM images of synthesis products at (a) 1050 °C and (b) 1200 °C from Etidot-67.

Etidot-67 performed worse than both Colemanite and Ulexite as a boron precursor. SEM image taken from 1050 °C synthesis temperature (Figure 4.12 a.) shows short tube-like structures with agglomerated BNNT clusters. Although some small diameter BNNTs are

also visible, further optimization must be required to improve the BNNT synthesis from Etidot-67 mineral. Increasing the reaction temperature to 1200 °C resulted in no BNNT formation and instead showed highly crystalline compounds (Figure 4.12 b.) similar BN-catalyst phases we encountered in our earlier studies (Figure 4.5 b.). The thermal behavior and properties of the Etidot-67 are unknown, which makes it challenging for us to determine the reason behind the failure of the Etidot-67 as a boron precursor. However, the absence of any oxides in the structure of Etidot-67, as opposed to Ulexite and Colemanite, can explain the inefficiency of the mineral since we believe that these oxides also provide extra catalyst properties for the BNNT growth.

4.3.5 CB-iCVD Deposition of PTFE on the Surfaces of BNNTs

The morphological and compositional analysis of the BNNTs were conducted before and after the PTFE deposition to showcase the polymer coating of the BNNT surfaces. SEM images provided in Figure 4.13 show as-synthesized BNNTs before (Figure 4.13 a.) and after (Figure 4.13 c) the PTFE deposition via CB-iCVD. SEM images show no noticeable difference between the two samples, indicating the very low thickness of the polymer coatings. In order to confirm the presence of the PTFE, we performed an EDX analysis of the samples searching for an F atom. Figure 4.13 b. shows the EDX analysis of the non-coated BNNTs, with B, and N peak coming from the BNNTs, Si and O peaks coming from SiO_2 substrate, Pd and Au peaks coming from the conductive coating we had applied before the EDX analysis. There appears to be no F signal coming from the non-coated BNNT. As expected, the EDX spectrum of the PTFE coated BNNTs (Figure 4.13 d.) shows all the peaks encountered at non-coated BNNTs with the addition of an F peak. This led us to believe that PTFE coating was present on the surfaces of the BNNTs.

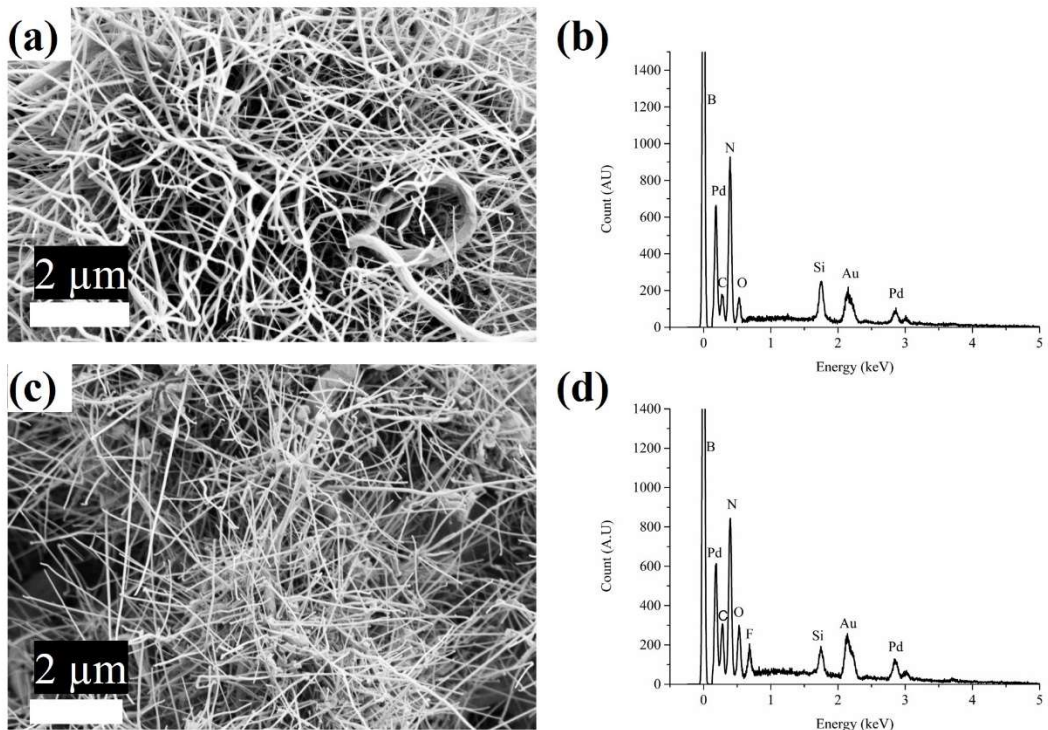


Figure 4.13 (a) SEM image of the non-coated as-synthesized BNNTs, and (b) its EDX spectrum. (c) SEM image of the PTFE coated as-synthesized BNNTs and (d) its EDX spectrum.

Due to the low resolution of the SEM images, imaging of the polymer coating was not possible. In order to better show the coating on the surface of the BNNTs, we have imaged the coated BNNT samples with TEM. TEM image of the single BNNT with PTFE coating can be seen in Figure 4.14 a. Similar to BNNT shown in Figure 4.6 b., these tubes also show hallow center (3) with parallel aligned walls (2) with the dark contrast. However, conformal amorphous film coating (1) can also be seen on the surface of the BNNTs compared to their non-coated counterparts. Furthermore, EELS analysis of the coated BNNTs also (Figure 4.14 b.) showed an additional C K-edge at 300 eV which was missing in the non-coated BNNTs EELS analysis (Figure 4.6 c.).

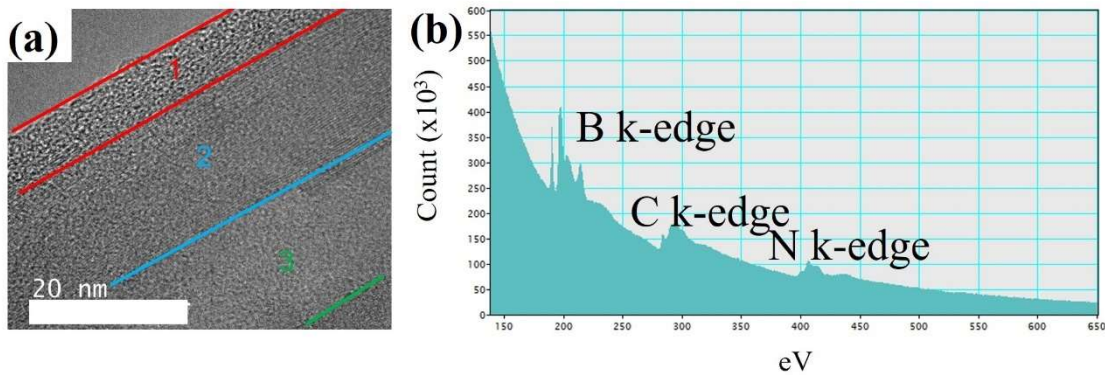


Figure 4.14 (a) TEM image of the single PTFE coated BNNT showing the (1) amorphous polymer coating, (2) parallel aligned walls, and (3) hallow tube center. (b) EELS of the single coated BNNT showing B and N K-edge from BNNT and C K-edge from polymer coating.

This result shows that it is possible to coat the surface of the as-synthesized BNNTs with PTFE polymer which can enhance the interface interactions of the filler inside the same polymer matrix. As a proof of concept, we believe that the same procedure can be further researched to coat desired polymers on the surface of the BNNTs to ensure better composite performance from BNNT/polymer composites.

4.4 Conclusions

BNNTs can be synthesized via the GVT-BOCVD method using Colemanite as a boron precursor and Fe_2O_3 catalyst with the assistance of sulfur-based molecules at a relatively low temperature of 1050 °C. The as-synthesized BNNTs are multiwalled with a 62 ± 20 nm diameter with good quality, as shown by the SEM, TEM, FTIR, and RAMAN analyses. Our results showed that the addition of thiophene allowed the synthesis of BNNTs at low temperatures by increasing the catalyst's efficiency by forming Fe-S intermediate products with iron catalyst allowing better interaction between the catalyst and the boron species. Among the sulfur-based molecules investigated in this study,

thiophene performed the best due to; its low vapor pressure, allowing it to be in a liquid state at room temperature, thus allowing better mixing with the colemanite/catalyst mixture and favorable decomposition mechanism that results in stable sulfur compounds. Our evaluation of similar boron minerals showed that Ulexite can also be used as a boron precursor at a higher synthesis temperature of 1200 °C but requires further optimization to be as viable as Colemanite. The low yield of the BNNT synthesis from colemanite at 1050 °C represents the most important roadblock to be overcome in order to elevate the proposed synthesis route to a large-scale production option. Further research on the reduction of the precursor particle size to increase catalyst-precursor interaction efficiency is planned. The simplicity of the process (both the equipment and the chemicals) encourages further research into the enhancement of the production yield of the BNNTs. Moreover, as-synthesized BNNTs can be surface modified by using the CB-iCVD method to deposit polymer coatings to their surface to provide better dispersibility in aqueous solutions as well as enhancing the interface interactions between the BNNT and the matrix by coating the BNNTs with the same polymer as the matrix polymer. However, further research is required to show if the theorized benefits are indeed achieved by the polymer coating. The manuscript of this chapter is under revision at ACS Applied Nano Materials to be published.

4.5 Acknowledgments

The authors would like to acknowledge Eti Maden İşletmeleri for kindly supplying the various boron minerals that have been used in this study. The authors would also like to extend their gratitude to Cleva W. Ow-Yang for her help during the research.

Chapter 5 CONCLUSIONS AND FUTURE WORK

This thesis study has demonstrated possible applications for boron nitride nanotubes, boron nitride microfiber, and boron nitride nano/microparticles as interface decorating layers and ceramic filler for the dielectric polymeric composites. Moreover, we have suggested a new, scalable method to synthesize BNNTs at relatively low temperatures with the assistance of S-based molecules.

In chapter 1, BNNTs were successfully decorated on the surfaces of the SiC fibers via the GVT-BOCVD method following a simple catalyzing step. Our results showed that BNNT could be grown on the SiC surfaces at 1200 °C in 1 hour with a diameter below 100 nm. This decoration process caused no further damage to SiC (thermal damage) and increased the IFSS of the single fiber by at least 87.8 %. We believe the increased specific surface area of the SiC fibers and the “velcro-like” interactions between the surface BNNT and matrix, enhanced the IFSS of the SiC fibers considerably.

We propose a further work in which, the effectiveness of the BNNT layer shall be evaluated inside a ceramic matrix as opposed to the epoxy matrix to provide better insight into CMC applications.

In chapter 2, BN-MF was synthesized via a simple precursor pyrolysis process at optimized 1100 °C. The SEM images show that fibers have 0.5 – 1 µm diameter and porous structure which was supported by the TEM imaging. Fabrication of BN/Noryl composites was also achieved and yielded composites with 24.03 % lower dielectric constant and 55.9 % dielectric loss. We argued that the porous structure of the composites, the intrinsic dielectric properties of the BN fillers, and the insulating property of the BN

allowed the decreased dielectric properties of the composites compared to neat noryl. Furthermore, the T_g of the composites also improved significantly due to inhibition of the chain movements of the matrix polymer.

As future work, we propose the evaluation of new precursors to be used in BN-MF synthesis, fabrication of large-scale composites to allow thermal and electrical analyses, determination of the porosity in the composite materials and correlation it has on the dielectric properties of the composites, and last, measurement of dielectric properties in broader range to better understand the full range of the dielectric properties.

In chapter 3, we have shown the synthesis of BNNTs from colemanite at a relatively low temperature of 1050 °C with the assistance of thiophene. We believe that, with further research, this technique can be utilized as a low-cost, novel, environmentally safe, and large-scale synthesis of BNNTs. Moreover, we have evaluated other boron minerals as an alternative to colemanite, namely Ulexite and Etidot-67, and showed their potential in BNNT synthesis. Our results showed that the selection of the S-based molecule also plays an essential part in the efficiency of the BNNT synthesis as thiophene with its low vapor pressure and stable decomposition products provided the best synthesis compared to other S-based molecules. Finally, we achieved a proof of concept for the CB-iCVD coating of the as-synthesized BNNTs with polymers with coating our BNNTs with PTFE. The TEM analysis shows the ultra-thin PTFE coating on the surface of the BNNTs which is then further confirmed with EDX and EELS.

Evaluation of the other polymers or functional groups as a surface functionalizing layer should be conducted to apply this proof of concept to various applications such as aqueous dispersion of the BNNTs, structural composites with strong interface interactions, and electroactive composites with a good interface.

REFERENCES

- [1] F.L. Alves, A. Baptista, A. Marques, Metal and ceramic matrix composites in aerospace engineering, *Advanced composite materials for aerospace engineering*, Elsevier2016, pp. 59-99.
- [2] V.T. Rathod, J.S. Kumar, A. Jain, Polymer and ceramic nanocomposites for aerospace applications, *Applied Nanoscience* 7(8) (2017) 519-548
- [3] R. Naslain, A. Guette, F. Rebillat, R. Pailler, F. Langlais, X. Bourrat, Boron-bearing species in ceramic matrix composites for long-term aerospace applications, *Journal of Solid State Chemistry* 177(2) (2004) 449-456
- [4] K.K. Chawla, Ceramic matrix composites, *Composite Materials*, Springer2019, pp. 251-296.
- [5] K. Zhang, L. Zhang, R. He, K. Wang, K. Wei, B. Zhang, Joining of Cf/SiC Ceramic Matrix Composites: A Review, *Advances in Materials Science Engineering* 2018 (2018)
- [6] M. Rosso, Ceramic and metal matrix composites: Routes and properties, *Journal of Materials Processing Technology* 175(1) (2006) 364-375. <https://doi.org/10.1016/j.jmatprotec.2005.04.038>
- [7] P. Wang, F. Liu, H. Wang, H. Li, Y. Gou, A review of third generation SiC fibers and SiCf/SiC composites, *Journal of Materials Science Technology* 35(12) (2019) 2743-2750
- [8] P. Fenici, A.F. Rebelo, R. Jones, A. Kohyama, L. Snead, Current status of SiC/SiC composites R&D, *Journal of Nuclear Materials* 258 (1998) 215-225
- [9] O. Flores, R.K. Bordia, S. Bernard, T. Uhlemann, W. Krenkel, G. Motz, Processing and characterization of large diameter ceramic SiCN monofilaments from commercial oligosilazanes, *RSC Advances* 5(129) (2015) 107001-107011
- [10] S. Yajima, K. Okamura, J. Hayashi, M. Omori, Synthesis of continuous SiC fibers with high tensile strength, *Journal of the American Ceramic Society* 59(7-8) (1976) 324-327
- [11] T. Ishikawa, Recent developments of the SiC fiber Nicalon and its composites, including properties of the SiC fiber Hi-Nicalon for ultra-high temperature, *Composites science technology* 51(2) (1994) 135-144
- [12] M. Takeda, J. Sakamoto, A. Saeki, H. Ichikawa, Mechanical and structural analysis of silicon carbide fiber Hi-Nicalon type S, *Proceedings of the 20th Annual Conference on Composites, Advanced Ceramics, Materials, and Structures—B: Ceramic Engineering and Science Proceedings*, Wiley Online Library, 1996, pp. 35-42

[13] C.H. Andersson, R. Warren, Silicon carbide fibres and their potential for use in composite materials. Part 1, Composites 15(1) (1984) 16-24.[https://doi.org/10.1016/0010-4361\(84\)90956-X](https://doi.org/10.1016/0010-4361(84)90956-X)

[14] R. Naslain, Design, preparation and properties of non-oxide CMCs for application in engines and nuclear reactors: an overview, Composites Science Technology 64(2) (2004) 155-170

[15] K. Yoshida, Development of silicon carbide fiber-reinforced silicon carbide matrix composites with high performance based on interfacial and microstructure control, Journal of the Ceramic Society of Japan 118(1374) (2010) 82-90

[16] R. Jones, D. Steiner, H. Heinisch, G. Newsome, H. Kerch, Radiation resistant ceramic matrix composites, Journal of Nuclear Materials 245(2-3) (1997) 87-107

[17] Y. Katoh, L.L. Snead, C.H. Henager Jr, A. Hasegawa, A. Kohyama, B. Riccardi, H. Hegeman, Current status and critical issues for development of SiC composites for fusion applications, Journal of Nuclear Materials 367 (2007) 659-671

[18] G.S. Corman, M.K. Brun, K.L. Luthra, SiC fiber reinforced SiC-Si matrix composites prepared by melt infiltration (MI) for gas turbine engine applications, ASME 1999 International Gas Turbine and Aeroengine Congress and Exhibition, American Society of Mechanical Engineers Digital Collection, 1999,

[19] F. Christin, Design, Fabrication and Applications of C/C, C/Si and SiC/SiC Composites, High Temperature Ceramic Matrix Composites (2001) 729-743

[20] J. Llorca, M. Elices, J. Celemin, Toughness and microstructural degradation at high temperature in SiC fiber-reinforced ceramics, Acta materialia 46(7) (1998) 2441-2453

[21] R.W. Hertzberg, Deformation and fracture mechanics of engineering materials, Journal of Materials Education 19 (1997) 227-232

[22] A.G. Evans, D.B. Marshall, The mechanical behavior of ceramic matrix composites, Proceedings of The 7th International Conference On Fracture (ICF7), Elsevier, 1989, pp. 3593-3641

[23] J. Eldridge, R. Bhatt, J. Kiser, Investigation of interfacial shear strength in SiC/Si₃N₄ composites, Ceramic Engineering and Science Proceedings, 1991, pp. 1152-1171

[24] J. King, Failure in composite materials, Metals Materials & Design 5(12) (1989) 720-726

[25] N.R. Council, Ceramic Fibers and Coatings: Advanced Materials for the Twenty-First Century, National Academies Press 1998.

[26] T.J. Clark, E.R. Prack, M.I. Haider, L.C. Sawyer, Oxidation of SiC ceramic fiber, Ceram. Engng Sci. Proc, 2009, pp. 717-31

[27] C. Henager Jr, Y. Shin, Y. Blum, L. Giannuzzi, B. Kempshall, S.J.J.o.N.M. Schwarz, Coatings and joining for SiC and SiC-composites for nuclear energy systems, 367 (2007) 1139-1143

[28] R.H. Jones, SiC/SiC Composites for advanced nuclear applications, 27th Annual Cocoa Beach Conference on Advanced Ceramics and Composites: B: Ceramic Engineering and Science Proceedings, Wiley Online Library, 2003, pp. 261-267

[29] K. Shimoda, J.-S. Park, T. Hinoki, A. Kohyama, Influence of pyrolytic carbon interface thickness on microstructure and mechanical properties of SiC/SiC composites by NITE process, Composites Science Technology 68(1) (2008) 98-105

[30] F. Rebillat, J. Lamon, R. Naslain, E. Lara-Curzio, M.K. Ferber, T.M. Besmann, Properties of multilayered interphases in SiC/SiC chemical-vapor-infiltrated composites with “weak” and “strong” interfaces, J. Am. Ceram. Soc. 81(9) (1998) 2315-2326.<https://doi.org/10.1111/j.1151-2916.1998.tb02627.x>

[31] N. Frety, M. Boussuge, Relationship between high-temperature development of fibre-matrix interfaces and the mechanical behaviour of SiC • SiC composites, Composites science technology 37(1-3) (1990) 177-189

[32] H. Li, J. Lee, M.R. Libera, W.Y. Lee, A. Kebbede, M.J. Lance, H. Wang, G.N. Morscher, Morphological Evolution and Weak Interface Development within Chemical-Vapor-Deposited Zirconia Coating Deposited on Hi-Nicalon™ Fiber, Journal of the American Ceramic Society 85(6) (2002) 1561-1568

[33] H. Li, G.N. Morscher, J. Lee, W.Y. Lee, Tensile and Stress-Rupture Behavior of SiC/SiC Minicomposite Containing Chemically Vapor Deposited Zirconia Interphase, Journal of the American Ceramic Society 87(9) (2004) 1726-1733

[34] S. Zhao, X. Zhou, J. Yu, P. Mummery, SiC/SiC composite fabricated with carbon nanotube interface layer and a novel precursor LPVCS, Fusion Engineering Design 89(2) (2014) 131-136

[35] K. König, S. Novak, A. Ivezković, K. Rade, D. Meng, A.R. Boccaccini, S.J.J.o.t.E.C.S. Kobe, Fabrication of CNT-SiC/SiC composites by electrophoretic deposition, 30(5) (2010) 1131-1137

[36] G.N. Morscher, H.M. Yun, J.A. DiCarlo, L. Thomas-Ogbuji, Effect of a boron nitride interphase that debonds between the interphase and the matrix in SiC/SiC composites, Journal of the American Ceramic Society 87(1) (2004) 104-112

[37] K. More, P. Tortorelli, H. Lin, E. Lara-Curzio, R. Lowden, P. Hou, M. McNallan, R. Oltra, E. Opila, D. Shores, Degradation Mechanisms of BN Interfaces in SiC/SiC Composites in Oxygen-and Water-Containing Environments, Proceedings of the Symposium on High Temperature Corrosion and Materials Chemistry, The Electrochemical Society, 1998, p. 382

[38] B. Yang, X. Zhou, Y. Chai, Mechanical properties of SiCf/SiC composites with PyC and the BN interface, Ceramics International 41(5) (2015) 7185-7190

[39] W. Yang, H. Araki, T. Noda, J.Y. Park, Y. Katoh, T. Hinoki, J. Yu, A. Kohyama, Hi-NicalonTM Fiber-Reinforced CVI-SiC Matrix Composites: I Effects of PyC and PyC-SiC Multilayers on the Fracture Behaviors and Flexural Properties, Materials Transactions Composites Science 43(10) (2002) 2568-2573

[40] X. Cao, X. Yin, X. Fan, L. Cheng, L. Zhang, Effect of PyC interphase thickness on mechanical behaviors of SiBC matrix modified C/SiC composites fabricated by reactive melt infiltration, Carbon 77 (2014) 886-895. <https://doi.org/10.1016/j.carbon.2014.05.092>

[41] R.R. Naslain, R.J.F. Pailler, J.L. Lamon, Single-and multilayered interphases in SiC/SiC composites exposed to severe environmental conditions: an overview, International Journal of Applied Ceramic Technology 7(3) (2010) 263-275

[42] H. Li, G.N. Morscher, J. Lee, W.Y. Lee, Tensile and Stress-Rupture Behavior of SiC/SiC Minicomposite Containing Chemically Vapor Deposited Zirconia Interphase, Journal of the American Ceramic Society 87(9) (2004) 1726-1733

[43] W.Y. Lee, E. Lara-Curzio, K.L. More, Multilayered oxide interphase concept for ceramic-matrix composites, Journal of the American Ceramic Society 81(3) (1998) 717-720

[44] A.H. Hart, R. Koizumi, J. Hamel, P.S. Owuor, Y. Ito, S. Ozden, S. Bhowmick, S.A. Syed Amanulla, T. Tsafack, K.J.A.a.m. Keyshar, interfaces, Velcro-inspired SiC fuzzy fibers for aerospace applications, 9(15) (2017) 13742-13750

[45] S. Bertrand, O. Boisron, R. Pailler, J. Lamon, R. Naslain, ETDEWEB/Search Results/(PyC/SiC){sub n} and (BN/SiC){sub n} nanoscale-multilayered interphases by pressure pulsed-CVI, (1999)

[46] F. Rebillat, J. Lamon, A. Guette, The concept of a strong interface applied to SiC/SiC composites with a BN interphase, *Acta Mater.* 48(18-19) (2000) 4609-4618.[https://doi.org/10.1016/S1359-6454\(00\)00247-0](https://doi.org/10.1016/S1359-6454(00)00247-0)

[47] S. Bertrand, R. Pailler, J. Lamon, Influence of strong fiber/coating interfaces on the mechanical behavior and lifetime of Hi-Nicalon/(PyC/SiC)n/SiC minicomposites, *J. Am. Ceram. Soc.* 84(4) (2001) 787-794.<https://doi.org/10.1111/j.1151-2916.2001.tb00742.x>

[48] S. Dong, Y. Katoh, A. Kohyama, Preparation of SiC/SiC composites by hot pressing, using Tyranno-SA fiber as reinforcement, *Journal of the American Ceramic Society Composites Science* 86(1) (2003) 26-32

[49] S. Pasquier, J. Lamon, R. Naslain, Tensile static fatigue of 2D SiC/SiC composites with multilayered (PyC-SiC)n interphases at high temperatures in oxidizing atmosphere, *Composites Part A: Applied Science and Manufacturing* 29(9) (1998) 1157-1164.[https://doi.org/10.1016/S1359-835X\(98\)00093-1](https://doi.org/10.1016/S1359-835X(98)00093-1)

[50] E.J. Garcia, B.L. Wardle, A. John Hart, N. Yamamoto, Fabrication and multifunctional properties of a hybrid laminate with aligned carbon nanotubes grown In Situ, *Compos. Sci. Technol.* 68(9) (2008) 2034-2041.<https://doi.org/10.1016/j.compscitech.2008.02.028>

[51] S.S. Wicks, R.G. de Villoria, B.L. Wardle, Interlaminar and intralaminar reinforcement of composite laminates with aligned carbon nanotubes, *Compos. Sci. Technol.* 70(1) (2010) 20-28.<https://doi.org/10.1016/j.compscitech.2009.09.001>

[52] K. Sun, J. Yu, C. Zhang, X. Zhou, In situ growth carbon nanotube reinforced SiCf/SiC composite, *Mater. Lett.* 66(1) (2012) 92-95.<https://doi.org/10.1016/j.matlet.2011.07.105>

[53] K. König, S. Novak, A. Ivezović, K. Rade, D. Meng, A.R. Boccaccini, S. Kobe, Fabrication of CNT-SiC/SiC composites by electrophoretic deposition, *J. Eur. Ceram. Soc.* 30(5) (2010) 1131-1137.<https://doi.org/10.1016/j.jeurceramsoc.2009.07.027>

[54] S. Zhao, X. Zhou, J. Yu, P. Mummery, SiC/SiC composite fabricated with carbon nanotube interface layer and a novel precursor LPVCS, *Fusion Eng. Des.* 89(2) (2014) 131-136.<https://doi.org/10.1016/j.fusengdes.2014.01.051>

[55] R.B. Mathur, S. Chatterjee, B.P. Singh, Growth of carbon nanotubes on carbon fibre substrates to produce hybrid/phenolic composites with improved mechanical properties, *Compos. Sci. Technol.* 68(7-8) (2008) 1608-1615.<https://doi.org/10.1016/j.compscitech.2008.02.020>

[56] J.L. QiuHong Zhang, Ryan Sager, Liming Dai, Jeffery Baur, Hierarchical composites of carbon nanotubes on carbon fiber: Influence of growth condition on fiber tensile properties, *Compos. Sci. Technol.* 69 (2009) 594-601.<https://doi.org/10.1016/j.compscitech.2008.12.002>

[57] X. Liu, L. Zhang, X. Yin, F. Ye, Y. Liu, L. Cheng, Flexible thin SiC fiber fabrics using carbon nanotube modification for improving electromagnetic shielding properties, *Mater. Des.* 104 (2016) 68-75.<https://doi.org/10.1016/j.matdes.2016.05.005>

[58] W. Feng, L. Zhang, Y. Liu, X. Li, L. Cheng, B. Chen, Thermal and mechanical properties of SiC/SiC-CNTs composites fabricated by CVI combined with electrophoretic deposition, *Mater. Sci. Eng., A* 626 (2015) 500-504.<https://doi.org/10.1016/j.msea.2014.12.105>

[59] K. Hata, D.N. Futaba, K. Mizuno, T. Namai, M. Yumura, S. Iijima, Water-Assisted Highly Efficient Synthesis of Impurity-Free Single-Walled Carbon Nanotubes, *Science* 306(5700) (2004) 1362-1364.<https://doi.org/10.1126/science.1104962>

[60] A.H.C. Hart, R. Koizumi, J. Hamel, P.S. Owuor, Y. Ito, S. Ozden, S. Bhowmick, S.A. Syed Amanulla, T. Tsafack, K. Keyshar, R. Mital, J. Hurst, R. Vajtai, C.S. Tiwary, P.M. Ajayan, Velcro-Inspired SiC Fuzzy Fibers for Aerospace Applications, *ACS Appl. Mater. Interfaces* 9(15) (2017) 13742-13750. <https://doi.org/10.1021/acsami.7b01378>

[61] N.G. Chopra, R. Luyken, K. Cherrey, V.H. Crespi, M.L. Cohen, S.G. Louie, A. Zettl, Boron nitride nanotubes, *Science* 269(5226) (1995) 966-967. <https://doi.org/10.1126/science.269.5226.966>

[62] D. Golberg, Y. Bando, Y. Huang, T. Terao, M. Mitome, C. Tang, C. Zhi, Boron nitride nanotubes and nanosheets, *ACS nano* 4(6) (2010) 2979-2993. <https://doi.org/10.1021/nn1006495>

[63] A. Rubio, J.L. Corkill, M.L. Cohen, Theory of graphitic boron nitride nanotubes, *Phys. Rev. B: Condens. Matter* 49(7) (1994) 5081. <https://doi.org/10.1103/PhysRevB.49.5081>

[64] J. Hurst, Boron Nitride Nanotubes Grown on Commercial Silicon Carbide Fiber Tow and Fabric, in: S. Mathur, S.S. Ray (Eds.), *Nanostructured Materials and Nanotechnology VI*, The American Ceramic Society 2013, pp. 21-29.

[65] G. Zhu, S. Dong, D. Ni, C. Xu, D. Wang, Microstructure, mechanical properties and oxidation resistance of SiCf/SiC composites incorporated with boron nitride nanotubes, *RSC Adv.* 6(86) (2016) 83482-83492. <https://doi.org/10.1039/C6RA16496J>

[66] P. Nautiyal, C. Rudolf, A. Loganathan, C. Zhang, B. Boesl, A. Agarwal, Directionally Aligned Ultra-Long Boron Nitride Nanotube Induced Strengthening of Aluminum-Based Sandwich Composite, *Adv. Eng. Mater.* 18(10) (2016) 1747-1754. <https://doi.org/10.1002/adem.201600212>

[67] C.H. Lee, J. Wang, V.K. Kayatsha, J.Y. Huang, Y.K. Yap, Effective growth of boron nitride nanotubes by thermal chemical vapor deposition, *Nanotechnology* 19(45) (2008) 455605.10.1088/0957-4484/19/45/455605

[68] C. Zhi, Y. Bando, C. Tan, D. Golberg, Effective precursor for high yield synthesis of pure BN nanotubes, *Solid State Communications* 135(1-2) (2005) 67-70

[69] C.-C. Zhuang, J. Feng, H. Xu, L. Li, X.-W. Liu, Synthesis of boron nitride nanotube films with a nanoparticle catalyst, *Chinese Chemical Letters* 27(6) (2016) 871-874

[70] S.L. Mensah, V.K. Kayastha, I.N. Ivanov, D.B. Geohegan, Y.K. Yap, Formation of single crystalline ZnO nanotubes without catalysts and templates, *Applied physics letters* 90(11) (2007) 113108

[71] D. ASTM, 3379-75: Standard test method for tensile strength and Young's modulus for high-modulus single-filament materials, American Society for Testing Materials Standards (1975)

[72] A. Khalili, K. Kromp, Statistical properties of Weibull estimators, *Journal of materials science* 26(24) (1991) 6741-6752

[73] F.W. Zok, X. Chen, C.H. Weber, Tensile strength of SiC fibers, *Journal of the American Ceramic Society* 78(7) (1995) 1965-1968

[74] Y. Liu, N. Chai, H. Qin, Z. Li, F. Ye, L. Cheng, Tensile fracture behavior and strength distribution of SiCf/SiC composites with different SiBN interface thicknesses, *Ceram. Int.* 41(1) (2015) 1609-1616. <https://doi.org/10.1016/j.ceramint.2014.09.098>

[75] Y. Long, A. Javed, Y. Zhao, Z.-k. Chen, X. Xiong, P. Xiao, Fiber/matrix interfacial shear strength of C/C composites with PyC-TaC-PyC and PyC-SiC-TaC-PyC multi-interlayers, *Ceramics International* 39(6) (2013) 6489-6496

[76] R.A. Khan, A. Parsons, I. Jones, G. Walker, C. Rudd, Interfacial properties of phosphate glass fiber/poly (caprolactone) system measured using the single fiber fragmentation test, *Composite Interfaces* 18(1) (2011) 77-90

[77] C.-H. Hsueh, Interfacial debonding and fiber pull-out stresses of fiber-reinforced composites, *Materials Science and Engineering: A* 123(1) (1990) 1-11

[78] N. Graupner, J. Rößler, G. Ziegmann, J. Müssig, Fibre/matrix adhesion of cellulose fibres in PLA, PP and MAPP: a critical review of pull-out test, microbond test and single fibre fragmentation test results, *Composites Part A: Applied Science and Manufacturing* 63 (2014) 133-148

[79] S. Nam, A.N. Netravali, Characterization of ramie fiber/soy protein concentrate (SPC) resin interface, *Journal of Adhesion Science Technology* 18(9) (2004) 1063-1076

[80] A. Straub, M. Slivka, P. Schwartz, A study of the effects of time and temperature on the fiber/matrix interface strength using the microbond test, *Composites Science and Technology* 57(8) (1997) 991-994

[81] P. Ahmad, M.U. Khandaker, Y.M. Amin, Z.R. Khan, Synthesis of boron nitride microtubes and formation of boron nitride nanosheets, *Materials Manufacturing Processes* 30(2) (2015) 184-188

[82] J. Dai, L. Xu, Z. Fang, D. Sheng, Q. Guo, Z. Ren, K. Wang, Y. Qian, A convenient catalytic approach to synthesize straight boron nitride nanotubes using synergic nitrogen source, *Chemical physics letters* 440(4-6) (2007) 253-258

[83] A.S. Nazarov, V.N. Demin, E.D. Grayfer, A.I. Bulavchenko, A.T. Arymbaeva, H.J. Shin, J.Y. Choi, V.E. Fedorov, Functionalization and Dispersion of Hexagonal Boron Nitride (h-BN) Nanosheets Treated with Inorganic Reagents, *Chemistry—An Asian Journal* 7(3) (2012) 554-560

[84] R. Arenal, F. De la Pena, O. Stephan, M. Walls, M. Tence, A. Loiseau, C. Colliex, Extending the analysis of EELS spectrum-imaging data, from elemental to bond mapping in complex nanostructures, *Ultramicroscopy* 109(1) (2008) 32-38

[85] M. Yamaguchi, D.-M. Tang, C. Zhi, Y. Bando, D. Shtansky, D. Golberg, Synthesis, structural analysis and in situ transmission electron microscopy mechanical tests on individual aluminum matrix/boron nitride nanotube nanohybrids, *Acta materialia* 60(17) (2012) 6213-6222

[86] J.-H. Choi, J. Kim, D. Seo, Y.-S. Seo, Purification of boron nitride nanotubes via polymer wrapping, *Materials Research Bulletin* 48(3) (2013) 1197-1203

[87] P. Ahmad, M.U. Khandaker, N. Muhammad, F. Rehman, G. Khan, A.S. Khan, Z. Ullah, M.A. Rehman, S. Ahmed, M. Gulzar, Magnesium diboride (MgB₂): An effective and novel precursor for the synthesis of vertically aligned BNNTs, *Materials Research Bulletin* 98 (2018) 235-239

[88] E. Buet, C. Sauder, S. Poissonnet, P. Brender, R. Gadiou, C. Vix-Guterl, Influence of chemical and physical properties of the last generation of silicon carbide fibres on the mechanical behaviour of SiC/SiC composite, *J. Eur. Ceram. Soc.* 32(3) (2012) 547-557. <https://doi.org/10.1016/j.jeurceramsoc.2011.09.023>

[89] M. Takeda, J.-i. Sakamoto, Y. Imai, H. Ichikawa, Thermal stability of the low-oxygen-content silicon carbide fiber, Hi-NicalonTM, *Composites Science and Technology* 59(6) (1999) 813-819

[90] T. Mah, N. Hecht, D. McCullum, J. Hoenigman, H. Kim, A. Katz, H. Lipsitt, Thermal stability of SiC fibres (Nicalon®), *Journal of Materials Science* 19(4) (1984) 1191-1201

[91] S. Cao, J. Wang, H. Wang, Formation mechanism of large SiC grains on SiC fiber surfaces during heat treatment, *CrystEngComm* 18(20) (2016) 3674-3682.<https://doi.org/10.1039/C6CE00427J>

[92] M. Yuan, T. Zhou, J. He, L. Chen, Formation of boron nitride coatings on silicon carbide fibers using trimethylborate vapor, *Appl. Surf. Sci.* 382 (2016) 27-33.<https://doi.org/10.1016/j.apsusc.2016.04.080>

[93] S. Guo, Y. Kagawa, Temperature dependence of tensile strength for a woven Boron-Nitride-Coated Hi-NicalonTM SiC fiber-reinforced silicon-carbide-matrix composite, *J. Am. Ceram. Soc.* 84(9) (2001) 2079-2085.<https://doi.org/10.1111/j.1151-2916.2001.tb00961.x>

[94] M. Takeda, J.-i. Sakamoto, Y. Imai, H. Ichikawa, Thermal stability of the low-oxygen-content silicon carbide fiber, Hi-Nicalon, *Compos. Sci. Technol.* 59(6) (1999) 813-819.[https://doi.org/10.1016/S0266-3538\(99\)00012-3](https://doi.org/10.1016/S0266-3538(99)00012-3)

[95] N.L.H. T. Mah, D. E. McCullum, J. R. Hoenigman, H. M. Kim, A. P. Katz, H. A. Lipsitt, Thermal stability of SiC fibres (Nicalon), *J. Mater. Sci.* (1984) 1191-1201.<https://doi.org/10.1007/BF01120029>

[96] M.W. Narayanan Janakiraman, Jörg Schuhmacher, Klaus Müller, Joachim Bill, Fritz Aldinger, Thermal Stability, Phase Evolution, and Crystallization in Si-B-C-N Ceramics Derived from a Polyborosilazane Precursor, *J. Am. Ceram. Soc.* 7 (2002) 1807-1814.<https://doi.org/10.1111/j.1151-2916.2002.tb00357.x>

[97] Y. Chai, H. Zhang, X. Zhou, Y. Zhang, Effects of silicon ion irradiation on the interface properties of SiC f /SiC composites, *Ceram. Int.* 44(2) (2018) 2165-2169.<https://doi.org/10.1016/j.ceramint.2017.10.169>

[98] J. Karger-Kocsis, H. Mahmood, A. Pegoretti, Recent advances in fiber/matrix interphase engineering for polymer composites, *Prog. Mater Sci.* 73 (2015) 1-43.<https://doi.org/10.1016/j.pmatsci.2015.02.003>

[99] M. Mohammadalipour, M. Masoomi, M. Ahmadi, S. Safi, Interfacial shear strength characterization of GMA-grafted UHMWPE fiber/epoxy/nano clay hybrid nanocomposite materials, *RSC Adv.* 6(48) (2016) 41793-41799.<https://doi.org/10.1039/C6RA05027A>

[100] B. Dastorian Jamnani, S. Hosseini, S. Rahamanian, S. Abdul Rashid, S. Keshan Balavandy, Grafting carbon nanotubes on glass fiber by dip coating technique to enhance tensile and interfacial shear strength, *J. Nanomater* 2015 (2015).<https://doi.org/10.1155/2015/149736>

[101] X. Zhang, X. Fan, C. Yan, H. Li, Y. Zhu, X. Li, L. Yu, Interfacial microstructure and properties of carbon fiber composites modified with graphene oxide, *ACS Appl. Mater. Interfaces* 4(3) (2012) 1543-52.<https://doi.org/10.1021/am201757v>

[102] X.Z. Tang, B. Yu, R.V. Hansen, X. Chen, X. Hu, J. Yang, Grafting low contents of branched polyethylenimine onto carbon fibers to effectively improve their interfacial shear strength with an epoxy matrix, *Adv. Mater. Interfaces* 2(12) (2015) 1500122.<https://doi.org/10.1002/admi.201500122>

[103] Z. Dai, F. Shi, B. Zhang, M. Li, Z. Zhang, Effect of sizing on carbon fiber surface properties and fibers/epoxy interfacial adhesion, *Appl. Surf. Sci.* 257(15) (2011) 6980-6985.<https://doi.org/10.1016/j.apsusc.2011.03.047>

[104] C. Wang, Y. Li, L. Tong, Q. Song, K. Li, J. Li, Q. Peng, X. He, R. Wang, W. Jiao, The role of grafting force and surface wettability in interfacial enhancement of carbon nanotube/carbon fiber hierarchical composites, *Carbon* 69 (2014) 239-246.<https://doi.org/10.1016/j.carbon.2013.12.020>

[105] J. Craven, R. Cripps, C. Viney, Evaluating the silk/epoxy interface by means of the microbond test, *Composites Part A* 31(7) (2000) 653-660. [https://doi.org/10.1016/S1359-835X\(00\)00042-7](https://doi.org/10.1016/S1359-835X(00)00042-7)

[106] B. Miller, P. Muri, L. Rebendfeld, A microbond Method for Determination of the Shear Strength of a Fiber/Resin Interface, *Compos. Sci. Technol.* 28 (1987) 18-32. [https://doi.org/10.1016/0266-3538\(87\)90059-5](https://doi.org/10.1016/0266-3538(87)90059-5)

[107] B.M. Umesh Gaur, Microbond Method for Determination of the Shear Strength of a Fiber/Resin Interface: Evaluation of Experimental Parameters, *Compos. Sci. Technol.* 34 (1989) 35-51. [https://doi.org/10.1016/0266-3538\(89\)90076-6](https://doi.org/10.1016/0266-3538(89)90076-6)

[108] Z.X.a.L. Li, Understanding Interfaces and Mechanical Properties of Ceramic Matrix Composites, in: I.M. Low (Ed.), *Advances in Ceramic Matrix Composites*, Woodhead Publishing Limited2014.

[109] M. Sato, E. Imai, J. Koyanagi, Y. Ishida, T. Ogasawara, Evaluation of the interfacial strength of carbon-fiber-reinforced temperature-resistant polymer composites by the micro-droplet test, *Adv. Compos. Mater* 26(5) (2017) 465-476. <https://doi.org/10.1080/09243046.2017.1284638>

[110] J. Craven, R. Cripps, C. Viney, Evaluating the silk/epoxy interface by means of the microbond test, *Composites Part A: Applied Science and Manufacturing* 31(7) (2000) 653-660

[111] M. Zu, Q. Li, Y. Zhu, M. Dey, G. Wang, W. Lu, J.M. Deitzel, J.W. Gillespie Jr, J.-H. Byun, T.-W. Chou, The effective interfacial shear strength of carbon nanotube fibers in an epoxy matrix characterized by a microdroplet test, *Carbon* 50(3) (2012) 1271-1279. <https://doi.org/10.1016/j.carbon.2011.10.047>

[112] H. Qian, A. Bismarck, E.S. Greenhalgh, G. Kalinka, M.S. Shaffer, Hierarchical composites reinforced with carbon nanotube grafted fibers: the potential assessed at the single fiber level, *Chem. Mater.* 20(5) (2008) 1862-1869. <https://doi.org/10.1021/cm702782j>

[113] M. Harwell, D. Hirt, D. Edie, N. Popovska, G. Emig, Investigation of bond strength and failure mode between SiC-coated mesophase ribbon fiber and an epoxy matrix, *Carbon* 38(8) (2000) 1111-1121. [https://doi.org/10.1016/S0008-6223\(99\)00240-7](https://doi.org/10.1016/S0008-6223(99)00240-7)

[114] M. Pitkethly, J. Favre, U. Gaur, J. Jakubowski, S. Mudrich, D. Caldwell, L. Drzal, M. Nardin, H. Wagner, L. Di Landro, A round-robin programme on interfacial test methods, *Compos. Sci. Technol.* 48(1-4) (1993) 205-214. [https://doi.org/10.1016/0266-3538\(93\)90138-7](https://doi.org/10.1016/0266-3538(93)90138-7)

[115] S.-K. Kang, D.-B. Lee, N.-S. Choi, Fiber/epoxy interfacial shear strength measured by the microdroplet test, *Compos. Sci. Technol.* 69(2) (2009) 245-251. <https://doi.org/10.1016/j.compscitech.2008.10.016>

[116] H. Wang, H. Wang, W. Li, D. Ren, Y. Yu, An improved microbond test method for determination of the interfacial shear strength between carbon fibers and epoxy resin, *Polymer Testing* 32(8) (2013) 1460-1465

[117] B. Dastorian Jamnani, S. Hosseini, S. Rahamanian, S. Abdul Rashid, S. Keshan Balavandy, Grafting carbon nanotubes on glass fiber by dip coating technique to enhance tensile and interfacial shear strength, *Journal of Nanomaterials* 2015 (2015)

[118] A. Godara, L. Gorbatikh, G. Kalinka, A. Warrier, O. Rochez, L. Mezzo, F. Luizi, A.W. Van Vuure, S.V. Lomov, I. Verpoest, Interfacial shear strength of a glass fiber/epoxy bonding in composites modified with carbon nanotubes, *Compos. Sci. Technol.* 70(9) (2010) 1346-1352. <https://doi.org/10.1016/j.compscitech.2010.04.010>

[119] D. Köken, A. Top, F. Çakmak Cebeci, F. Turgut, B. Bozali, E. Özden-Yenigün, N. Solak, H. Cebeci, An effective growth of hierarchical BNNTs/SiC fibers with enhanced interfacial properties, *Compos. Sci. Technol.* 216 (2021) 109033.<https://doi.org/10.1016/j.compscitech.2021.109033>

[120] G. Maier, Low dielectric constant polymers for microelectronics, *Prog. Polym. Sci.* 26(1) (2001) 3-65.[https://doi.org/10.1016/S0079-6700\(00\)00043-5](https://doi.org/10.1016/S0079-6700(00)00043-5)

[121] P.A. Kohl, Low-Dielectric Constant Insulators for Future Integrated Circuits and Packages, *Annual Review of Chemical and Biomolecular Engineering* 2(1) (2011) 379-401.10.1146/annurev-chembioeng-061010-114137

[122] M.T. Sebastian, Dielectric materials for wireless communication, Elsevier2010.

[123] X. Huang, C. Zhi, P. Jiang, D. Golberg, Y. Bando, T. Tanaka, Polyhedral Oligosilsesquioxane-Modified Boron Nitride Nanotube Based Epoxy Nanocomposites: An Ideal Dielectric Material with High Thermal Conductivity, *Adv. Funct. Mater.* 23(14) (2013) 1824-1831.<https://doi.org/10.1002/adfm.201201824>

[124] S.-P. Jeng, R.H. Havemann, M.-C. Chang, Process integration and manufacturability issues for high performance multilevel interconnect, *MRS Online Proceedings Library (OPL)* 337 (1994)

[125] M.T. Bohr, Interconnect scaling-the real limiter to high performance ULSI, *Proceedings of International Electron Devices Meeting*, 1995, pp. 241-244.10.1109/IEDM.1995.499187

[126] D. Miller Robert, In Search of Low-k Dielectrics, *Science* 286(5439) (1999) 421-423.10.1126/science.286.5439.421

[127] M. Gupta, E.W.W. Leong, *Microwaves and metals*, John Wiley & Sons2008.

[128] G. Giannoukos, M. Min, T. Rang, Relative complex permittivity and its dependence on frequency, *World Journal of Engineering* 14(6) (2017) 532-537.10.1108/WJE-01-2017-0007

[129] A. Grill, PECVD low and ultralow dielectric constant materials: From invention and research to products, *Journal of Vacuum Science & Technology B* 34(2) (2016) 020801.10.1116/1.4943049

[130] A. Grill, Diamond-like carbon: state of the art, *Diamond Relat. Mater.* 8(2) (1999) 428-434.[https://doi.org/10.1016/S0925-9635\(98\)00262-3](https://doi.org/10.1016/S0925-9635(98)00262-3)

[131] A. Grill, V. Patel, C. Jahnes, Novel Low k Dielectrics Based on Diamondlike Carbon Materials, *J. Electrochem. Soc.* 145(5) (1998) 1649-1653.10.1149/1.1838531

[132] A. Grill, Amorphous carbon based materials as the interconnect dielectric in ULSI chips, *Diamond Relat. Mater.* 10(2) (2001) 234-239.[https://doi.org/10.1016/S0925-9635\(00\)00473-8](https://doi.org/10.1016/S0925-9635(00)00473-8)

[133] A. Grill, L. Perraud, V. Patel, C. Jahnes, S. Cohen, Low Dielectric Constant Sicoh Films As Potential Candidates for Interconnect Dielectrics, *MRS Online Proceedings Library* 565(1) (1999) 107-116.10.1557/PROC-565-107

[134] L. Wang, C. Liu, S. Shen, M. Xu, X. Liu, Low dielectric constant polymers for high speed communication network, *Advanced Industrial and Engineering Polymer Research* 3(4) (2020) 138-148.<https://doi.org/10.1016/j.aiepr.2020.10.001>

[135] C. Pan, K. Kou, Q. Jia, Y. Zhang, G. Wu, T. Ji, Improved thermal conductivity and dielectric properties of hBN/PTFE composites via surface treatment by silane coupling agent, *Composites Part B: Engineering* 111 (2017) 83-90.<https://doi.org/10.1016/j.compositesb.2016.11.050>

[136] H. Li, L. Ren, Y. Zhou, B. Yao, Q. Wang, Recent progress in polymer dielectrics containing boron nitride nanosheets for high energy density capacitors, *High Voltage* 5(4) (2020) 365-376.<https://doi.org/10.1049/hve.2020.0076>

[137] D. Ji, T. Li, W. Hu, H. Fuchs, Recent Progress in Aromatic Polyimide Dielectrics for Organic Electronic Devices and Circuits, *Adv. Mater.* 31(15) (2019) 1806070. <https://doi.org/10.1002/adma.201806070>

[138] S. Chisca, V.E. Musteata, I. Sava, M. Bruma, Dielectric behavior of some aromatic polyimide films, *Eur. Polym. J.* 47(5) (2011) 1186-1197. <https://doi.org/10.1016/j.eurpolymj.2011.01.008>

[139] J.O. Simpson, A.K. St.Clair, Fundamental insight on developing low dielectric constant polyimides, *Thin Solid Films* 308-309 (1997) 480-485. [https://doi.org/10.1016/S0040-6090\(97\)00481-1](https://doi.org/10.1016/S0040-6090(97)00481-1)

[140] H.-j. Ni, J.-g. Liu, S.-y. Yang, Fluorinated Poly(phenylquinoxaline)s with Low Dielectric Constants and High Hydrolytic Stability: Synthesis and Characterization, *Chem. Lett.* 45(1) (2015) 75-77.10.1246/cl.150921

[141] P. Machetta, M. Lazzarino, V. Kapeliouchko, T. Poggio, G. Canil, A. Sanguineti, V. Arcella, PTFE nanoemulsions as ultralow-k dielectric materials, *Macromolecular Symposia* 179(1) (2002) 347-358. [https://doi.org/10.1002/1521-3900\(200203\)179:1<347::AID-MASY347>3.0.CO;2-C](https://doi.org/10.1002/1521-3900(200203)179:1<347::AID-MASY347>3.0.CO;2-C)

[142] J. Wang, H.K. Kim, F.G. Shi, B. Zhao, T.G. Nieh, Thickness dependence of morphology and mechanical properties of on-wafer low-k PTFE dielectric films, *Thin Solid Films* 377-378 (2000) 413-417. [https://doi.org/10.1016/S0040-6090\(00\)01434-6](https://doi.org/10.1016/S0040-6090(00)01434-6)

[143] X. Huang, P. Jiang, T. Tanaka, A review of dielectric polymer composites with high thermal conductivity, *IEEE Electrical Insulation Magazine* 27(4) (2011) 8-16.10.1109/MEI.2011.5954064

[144] W. Sun Lee, J. Yu, Comparative study of thermally conductive fillers in underfill for the electronic components, *Diamond Relat. Mater.* 14(10) (2005) 1647-1653. <https://doi.org/10.1016/j.diamond.2005.05.008>

[145] M. Kozako, Y. Okazaki, M. Hikita, T. Tanaka, Preparation and evaluation of epoxy composite insulating materials toward high thermal conductivity, 2010 10th IEEE International Conference on Solid Dielectrics, 2010, pp. 1-4.10.1109/ICSD.2010.5568250

[146] J.-W. Zha, T.-X. Zhu, Y.-H. Wu, S.-J. Wang, R.K.Y. Li, Z.-M. Dang, Tuning of thermal and dielectric properties for epoxy composites filled with electrospun alumina fibers and graphene nanoplatelets through hybridization, *Journal of Materials Chemistry C* 3(27) (2015) 7195-7202.10.1039/C5TC01552A

[147] Y. Zhou, H. Wang, L. Wang, K. Yu, Z. Lin, L. He, Y. Bai, Fabrication and characterization of aluminum nitride polymer matrix composites with high thermal conductivity and low dielectric constant for electronic packaging, *Materials Science and Engineering: B* 177(11) (2012) 892-896. <https://doi.org/10.1016/j.mseb.2012.03.056>

[148] J. Wang, F. Ma, W. Liang, M. Sun, Electrical properties and applications of graphene, hexagonal boron nitride (h-BN), and graphene/h-BN heterostructures, *Materials Today Physics* 2 (2017) 6-34. <https://doi.org/10.1016/j.mtphys.2017.07.001>

[149] C. Yu, J. Zhang, W. Tian, X. Fan, Y. Yao, Polymer composites based on hexagonal boron nitride and their application in thermally conductive composites, *RSC advances* 8(39) (2018) 21948-21967

[150] N. Kostoglou, K. Polychronopoulou, C. Rebholz, Thermal and chemical stability of hexagonal boron nitride (h-BN) nanoplatelets, *Vacuum* 112 (2015) 42-45. <https://doi.org/10.1016/j.vacuum.2014.11.009>

[151] L. Lindsay, D.A. Broido, Enhanced thermal conductivity and isotope effect in single-layer hexagonal boron nitride, *Physical Review B* 84(15) (2011) 155421.10.1103/PhysRevB.84.155421

[152] L. Boldrin, F. Scarpa, R. Chowdhury, S. Adhikari, Effective mechanical properties of hexagonal boron nitride nanosheets, *Nanotechnology* 22(50) (2011) 505702.10.1088/0957-4484/22/50/505702

[153] Z. Lin, A. McNamara, Y. Liu, K.-s. Moon, C.-P. Wong, Exfoliated hexagonal boron nitride-based polymer nanocomposite with enhanced thermal conductivity for electronic encapsulation, *Compos. Sci. Technol.* 90 (2014) 123-128. <https://doi.org/10.1016/j.compscitech.2013.10.018>

[154] H.J. Ahn, E.S. Kim, Microwave Dielectric Properties of Oriented BN/Polyvinyl Butyral Matrix Composites, *Journal of the Korean Ceramic Society* 51(1) (2014) 32-36

[155] T. Zhang, J. Sun, L. Ren, Y. Yao, M. Wang, X. Zeng, R. Sun, J.-B. Xu, C.-P. Wong, Nacre-inspired polymer composites with high thermal conductivity and enhanced mechanical strength, *Composites Part A: Applied Science and Manufacturing* 121 (2019) 92-99. <https://doi.org/10.1016/j.compositesa.2019.03.017>

[156] M. Tanimoto, T. Yamagata, K. Miyata, S. Ando, Anisotropic Thermal Diffusivity of Hexagonal Boron Nitride-Filled Polyimide Films: Effects of Filler Particle Size, Aggregation, Orientation, and Polymer Chain Rigidity, *ACS Applied Materials & Interfaces* 5(10) (2013) 4374-4382.10.1021/am400615z

[157] M. Ge, J. Zhang, C. Zhao, C. Lu, G. Du, Effect of hexagonal boron nitride on the thermal and dielectric properties of polyphenylene ether resin for high-frequency copper clad laminates, *Materials & Design* 182 (2019) 108028. <https://doi.org/10.1016/j.matdes.2019.108028>

[158] Q. Deng, X. Li, Q. Li, X. Xia, C.e. He, Y. Feng, C. Peng, Well-balanced high permittivity and low dielectric loss obtained in PVDF/graphite/BN ternary composites by depressing interfacial leakage conduction, *Microelectron. Eng.* 231 (2020) 111404. <https://doi.org/10.1016/j.mee.2020.111404>

[159] C. Xia, A.C. Garcia, S.Q. Shi, Y. Qiu, N. Warner, Y. Wu, L. Cai, H.R. Rizvi, N.A. D'Souza, X. Nie, Hybrid boron nitride-natural fiber composites for enhanced thermal conductivity, *Scientific Reports* 6(1) (2016) 34726.10.1038/srep34726

[160] T. Terao, C. Zhi, Y. Bando, M. Mitome, C. Tang, D. Golberg, Alignment of Boron Nitride Nanotubes in Polymeric Composite Films for Thermal Conductivity Improvement, *The Journal of Physical Chemistry C* 114(10) (2010) 4340-4344.10.1021/jp911431f

[161] J. Lin, X. Yuan, G. Li, Y. Huang, W. Wang, X. He, C. Yu, Y. Fang, Z. Liu, C. Tang, Self-assembly of porous boron nitride microfibers into ultralight multifunctional foams of large sizes, *ACS applied materials & interfaces* 9(51) (2017) 44732-44739

[162] S. Komatsu, D. Kazami, H. Tanaka, Y. Shimizu, Y. Moriyoshi, M. Shiratani, K. Okada, Boron nitride microfibers grown by plasma-assisted laser chemical vapor deposition without a metal catalyst, *Appl. Phys. Lett.* 88(15) (2006) 151914.10.1063/1.2188381

[163] J. Lin, L. Xu, Y. Huang, J. Li, W. Wang, C. Feng, Z. Liu, X. Xu, J. Zou, C. Tang, Ultrafine porous boron nitride nanofibers synthesized via a freeze-drying and pyrolysis process and their adsorption properties, *RSC advances* 6(2) (2016) 1253-1259

[164] C.H. Chen, Z.C. Gu, Y.L. Tsai, R.J. Jeng, C.H. Lin, Identification of the reaction mechanism between phenyl methacrylate and epoxy and its application in preparing low-dielectric epoxy thermosets with flexibility, *Polymer* 140 (2018) 225-232. <https://doi.org/10.1016/j.polymer.2018.02.045>

[165] C. Wu, B. Wang, N. Wu, C. Han, X. Zhang, S. Shen, Q. Tian, C. Qin, P. Li, Y. Wang, Molecular-scale understanding on the structure evolution from melamine

diborate supramolecule to boron nitride fibers, *Ceram. Int.* 46(1) (2020) 1083-1090. <https://doi.org/10.1016/j.ceramint.2019.09.075>

[166] J. Jung, J. Kim, Y.R. Uhm, J.-K. Jeon, S. Lee, H.M. Lee, C.K. Rhee, Preparations and thermal properties of micro- and nano-BN dispersed HDPE composites, *Thermochim. Acta* 499(1) (2010) 8-14. <https://doi.org/10.1016/j.tca.2009.10.013>

[167] H. Zhang, R. Huang, Y. Li, H. Li, Z. Wu, J. Huang, B. Yu, X. Gao, J. Li, L. Li, Optimization of Boron Nitride Sphere Loading in Epoxy: Enhanced Thermal Conductivity and Excellent Electrical Insulation, *Polymers* 11(8) (2019).10.3390/polym11081335

[168] Y. Sun, Z. Zhang, K.-S. Moon, C.P. Wong, Glass transition and relaxation behavior of epoxy nanocomposites, *J. Polym. Sci., Part B: Polym. Phys.* 42(21) (2004) 3849-3858. <https://doi.org/10.1002/polb.20251>

[169] S.C. Tjong, Structural and mechanical properties of polymer nanocomposites, *Materials Science and Engineering: R: Reports* 53(3) (2006) 73-197. <https://doi.org/10.1016/j.mser.2006.06.001>

[170] Y. Wu, R. Shrivpuri, L.J. Lee, Effect of Macro and Micro Voids on Elastic Properties of Polymer Composites, *J. Reinforced Plast. Compos.* 17(15) (1998) 1391-1402.10.1177/073168449801701507

[171] H. Fang, S.-L. Bai, C.P. Wong, Thermal, mechanical and dielectric properties of flexible BN foam and BN nanosheets reinforced polymer composites for electronic packaging application, *Composites Part A: Applied Science and Manufacturing* 100 (2017) 71-80. <https://doi.org/10.1016/j.compositesa.2017.04.018>

[172] X. Huang, S. Wang, M. Zhu, K. Yang, P. Jiang, Y. Bando, D. Golberg, C. Zhi, Thermally conductive, electrically insulating and melt-processable polystyrene/boron nitride nanocomposites prepared by in situ reversible addition fragmentation chain transfer polymerization, *Nanotechnology* 26(1) (2014) 015705

[173] C.Y. Zhi, Y. Bando, T. Terao, C. Tang, D. Golberg, Dielectric and thermal properties of epoxy/boron nitride nanotube composites, *Pure Appl. Chem.* 82(11) (2010) 2175-2183. doi:10.1351/PAC-CON-09-11-41

[174] S. Singha, M.J. Thomas, Permittivity and tan delta characteristics of epoxy nanocomposites in the frequency range of 1 MHz-1 GHz, *IEEE Transactions on Dielectrics and Electrical Insulation* 15(1) (2008) 2-11.10.1109/T-DEI.2008.4446731

[175] R. Popielarz, C.K. Chiang, R. Nozaki, J. Obrzut, Dielectric Properties of Polymer/Ferroelectric Ceramic Composites from 100 Hz to 10 GHz, *Macromolecules* 34(17) (2001) 5910-5915.10.1021/ma001576b

[176] S. Iijima, Helical microtubules of graphitic carbon, *Nature* 354(6348) (1991) 56-58. <https://doi.org/10.1038/354056a0>

[177] N.G. Chopra, A. Zettl, Measurement of the elastic modulus of a multi-wall boron nitride nanotube, *Solid State Communications* 105(5) (1998) 297-300. [https://doi.org/10.1016/S0038-1098\(97\)10125-9](https://doi.org/10.1016/S0038-1098(97)10125-9)

[178] D. Golberg, X.D. Bai, M. Mitome, C.C. Tang, C.Y. Zhi, Y. Bando, Structural peculiarities of in situ deformation of a multi-walled BN nanotube inside a high-resolution analytical transmission electron microscope, *Acta Mater.* 55(4) (2007) 1293-1298. <https://doi.org/10.1016/j.actamat.2006.09.034>

[179] M.M.H. Bhuiyan, J. Wang, L.H. Li, P. Hodgson, A. Agarwal, M. Qian, Y. Chen, Boron nitride nanotube reinforced titanium metal matrix composites with excellent high-temperature performance, *J. Mater. Res.* 32(19) (2017) 3744-3752. <https://doi.org/10.1557/jmr.2017.345>

[180] D. Lahiri, A. Hadjikhani, C. Zhang, T. Xing, L.H. Li, Y. Chen, A. Agarwal, Boron nitride nanotubes reinforced aluminum composites prepared by spark plasma sintering: Microstructure, mechanical properties and deformation behavior, *Materials Science and Engineering: A* 574 (2013) 149-156. <https://doi.org/10.1016/j.msea.2013.03.022>

[181] M.B. Jakubinek, B. Ashrafi, Y. Martinez-Rubi, J. Guan, M. Rahmat, K.S. Kim, S. Dénommée, C.T. Kingston, B. Simard, Boron nitride nanotube composites and applications, *Nanotube Superfiber Materials*, Elsevier2019, pp. 91-111.

[182] L. Li, Y. Chen, Z.H. Stachurski, Boron nitride nanotube reinforced polyurethane composites, *Progress in Natural Science: Materials International* 23(2) (2013) 170-173. <https://doi.org/10.1016/j.pnsc.2013.03.004>

[183] P. Tatarko, S. Grasso, H. Porwal, Z. Chlup, R. Saggar, I. Dlouhý, M.J. Reece, Boron nitride nanotubes as a reinforcement for brittle matrices, *Journal of the European Ceramic Society* 34(14) (2014) 3339-3349. <https://doi.org/10.1016/j.jeurceramsoc.2014.03.028>

[184] W.H. Moon, H.J. Hwang, Molecular-dynamics simulation of structure and thermal behaviour of boron nitride nanotubes, *Nanotechnology* 15(5) (2004) 431-434. <https://doi.org/10.1088/0957-4484/15/5/005>

[185] D. Golberg, Y. Bando, K. Kurashima, T. Sato, Synthesis and characterization of ropes made of BN multiwalled nanotubes, *Scripta Mater.* 44(8) (2001) 1561-1565. [https://doi.org/10.1016/S1359-6462\(01\)00724-2](https://doi.org/10.1016/S1359-6462(01)00724-2)

[186] A. Chandra, P.K. Patra, B. Bhattacharya, Thermomechanical buckling of boron nitride nanotubes using molecular dynamics, *Materials Research Express* 3(2) (2016) 025005. <https://doi.org/10.1088/2053-1591/3/2/025005>

[187] C.-c. Hung, Boron Nitride Nanotubes Grown on Commercial Silicon Carbide Fiber Tow and Fabric, *Nanostructured Materials and Nanotechnology VI* 575 (2012) 21

[188] G. Zhu, Y. Xue, J. Hu, J. Yang, H. Zhou, L. Gao, Q. Shan, S. Dong, Influence of boron nitride nanotubes on the damage evolution of SiCf/SiC composites, *Journal of the European Ceramic Society* 38(14) (2018) 4614-4622. <https://doi.org/10.1016/j.jeurceramsoc.2018.06.030>

[189] D. Köken, A. Top, F.Ç. Cebeci, F. Turgut, B. Bozali, E. Özden Yenigün, N. Solak, H. Cebeci, An Effective Growth of Hierarchical BNNTs/SiC Fibers with Enhanced Interfacial Properties, Under Review (2021)

[190] P. Snapp, C. Cho, D. Lee, M.F. Haque, S. Nam, C. Park, Tunable Piezoelectricity of Multifunctional Boron Nitride Nanotube/Poly(dimethylsiloxane) Stretchable Composites, *Advanced Materials* 32(43) (2020) 2004607. <https://doi.org/10.1002/adma.202004607>

[191] P. Ahmad, M.U. Khandaker, Y.M. Amin, G. Khan, S.M. Ramay, A. Mahmood, M. Amin, N. Muhammad, Catalytic growth of vertically aligned neutron sensitive 10 Boron nitride nanotubes, *Journal of Nanoparticle Research* 18(1) (2016) 25. <http://dx.doi.org/10.1007%2Fs11051-016-3326-0>

[192] S.A. Thibeault, J.H. Kang, G. Sauti, C. Park, C.C. Fay, G.C. King, Nanomaterials for radiation shielding, *MRS Bulletin* 40(10) (2015) 836-841. <https://doi.org/10.1557/mrs.2015.225>

[193] N.G. Chopra, R.J. Luyken, K. Cherrey, V.H. Crespi, M.L. Cohen, S.G. Louie, A. Zettl, Boron nitride nanotubes, *Science* 269(5226) (1995) 966-967. <https://doi.org/10.1126/science.269.5226.966>

[194] Y.-W. Yeh, Y. Raitses, B.E. Koel, N. Yao, Stable synthesis of few-layered boron nitride nanotubes by anodic arc discharge, *Scientific Reports* 7(1) (2017) 3075.10.1038/s41598-017-03438-w

[195] S.H. Lim, J. Luo, W. Ji, J. Lin, Synthesis of boron nitride nanotubes and its hydrogen uptake, *Catal. Today* 120(3) (2007) 346-350.<https://doi.org/10.1016/j.cattod.2006.09.016>

[196] L. Li, L.H. Li, Y. Chen, X.J. Dai, T. Xing, M. Petracic, X. Liu, Mechanically activated catalyst mixing for high-yield boron nitride nanotube growth, *Nanoscale Research Letters* 7(1) (2012) 417.10.1186/1556-276X-7-417

[197] W. Han, Y. Bando, K. Kurashima, T. Sato, Synthesis of boron nitride nanotubes from carbon nanotubes by a substitution reaction, *Appl. Phys. Lett.* 73(21) (1998) 3085-3087.<https://doi.org/10.1063/1.122680>

[198] O.R. Lourie, C.R. Jones, B.M. Bartlett, P.C. Gibbons, R.S. Ruoff, W.E. Buhro, CVD Growth of Boron Nitride Nanotubes, *Chem. Mater.* 12(7) (2000) 1808-1810.<https://doi.org/10.1021/cm000157q>

[199] J.H. Kim, T.V. Pham, J.H. Hwang, C.S. Kim, M.J. Kim, Boron nitride nanotubes: synthesis and applications, *Nano Convergence* 5(1) (2018) 17.<https://doi.org/10.1186/s40580-018-0149-y>

[200] C. Tang, Y. Bando, T. Sato, K. Kurashima, A novel precursor for synthesis of pure boron nitride nanotubes, *Chem. Commun.* (12) (2002) 1290-1291.<https://doi.org/10.1039/B202177C>

[201] C. Zhi, Y. Bando, C. Tan, D. Golberg, Effective precursor for high yield synthesis of pure BN nanotubes, *Solid State Commun.* 135(1) (2005) 67-70.<https://doi.org/10.1016/j.ssc.2005.03.062>

[202] J. Blakely, K. Jackson, Growth of crystal whiskers, *The Journal of Chemical Physics* 37(2) (1962) 428-430

[203] L. Chee Huei, W. Jiesheng, K.K. Vijaya, Y.H. Jian, Y. Yoke Khin, Effective growth of boron nitride nanotubes by thermal chemical vapor deposition, *Nanotechnology* 19(45) (2008) 455605

[204] M.J. Kim, S. Chatterjee, S.M. Kim, E.A. Stach, M.G. Bradley, M.J. Pender, L.G. Sneddon, B. Maruyama, Double-Walled Boron Nitride Nanotubes Grown by Floating Catalyst Chemical Vapor Deposition, *Nano Lett.* 8(10) (2008) 3298-3302.<https://doi.org/10.1021/nl8016835>

[205] C.-Y. Su, W.-Y. Chu, Z.-Y. Juang, K.-F. Chen, B.-M. Cheng, F.-R. Chen, K.-C. Leou, C.-H. Tsai, Large-Scale Synthesis of Boron Nitride Nanotubes with Iron-Supported Catalysts, *The Journal of Physical Chemistry C* 113(33) (2009) 14732-14738.<https://doi.org/10.1021/jp904583p>

[206] L. Guo, R.N. Singh, Selective growth of boron nitride nanotubes by plasma-enhanced chemical vapor deposition at low substrate temperature, *Nanotechnology* 19(6) (2008) 065601.<https://doi.org/10.1088/0957-4484/19/6/065601>

[207] X.Z. Wang, Q. Wu, Z. Hu, Y. Chen, Template-directed synthesis of boron nitride nanotube arrays by microwave plasma chemical reaction, *Electrochimica acta* 52(8) (2007) 2841-2844.<https://doi.org/10.1016/j.electacta.2006.08.047>

[208] S. Chatterjee, M.J. Kim, D.N. Zakharov, S.M. Kim, E.A. Stach, B. Maruyama, L.G. Sneddon, Syntheses of Boron Nitride Nanotubes from Borazine and Decaborane Molecular Precursors by Catalytic Chemical Vapor Deposition with a Floating Nickel Catalyst, *Chem. Mater.* 24(15) (2012) 2872-2879.<https://doi.org/10.1021/cm3006088>

[209] M. Liu, K. Hisama, Y. Zheng, M. Maruyama, S. Seo, A. Anisimov, T. Inoue, E.I. Kauppinen, S. Okada, S. Chiashi, Photoluminescence from Single-Walled MoS₂

Nanotubes Coaxially Grown on Boron Nitride Nanotubes, ACS Nano 15(5) (2020) 8418-8426.<https://doi.org/10.1021/acsnano.0c10586>

[210] M.W. Smith, K.C. Jordan, C. Park, J.-W. Kim, P.T. Lillehei, R. Crooks, J.S. Harrison, Very long single- and few-walled boron nitride nanotubes via the pressurized vapor/condenser method, Nanotechnology 20(50) (2009) 505604.10.1088/0957-4484/20/50/505604

[211] A. Fathalizadeh, T. Pham, W. Mickelson, A. Zettl, Scaled Synthesis of Boron Nitride Nanotubes, Nanoribbons, and Nanococoons Using Direct Feedstock Injection into an Extended-Pressure, Inductively-Coupled Thermal Plasma, Nano Lett. 14(8) (2014) 4881-4886.10.1021/nl5022915

[212] K.S. Kim, C.T. Kingston, A. Hrdina, M.B. Jakubinek, J. Guan, M. Plunkett, B. Simard, Hydrogen-Catalyzed, Pilot-Scale Production of Small-Diameter Boron Nitride Nanotubes and Their Macroscopic Assemblies, ACS Nano 8(6) (2014) 6211-6220.10.1021/nn501661p

[213] D.S. Lashmore, Tyler Bennett, Continuous boron nitride nanotube yarns and methods of production US20150033937A1, in: U.S.P.a.T. Office (Ed.) University of New Hampshire, United States, 2019,

[214] W.M. da Silva, H. Ribeiro, T.H. Ferreira, L.O. Ladeira, E.M.B. Sousa, Synthesis of boron nitride nanostructures from catalyst of iron compounds via thermal chemical vapor deposition technique, Physica E: Low-dimensional Systems and Nanostructures 89 (2017) 177-182.<https://doi.org/10.1016/j.physe.2017.01.030>

[215] S. Kalay, Z. Yilmaz, M. Culha, Synthesis of boron nitride nanotubes from unprocessed colemanite, Beilstein Journal of Nanotechnology 4 (2013) 843-851.
<https://doi.org/10.3762/bjnano.4.95>

[216] J. Miller, C. Zeitlin, F. Cucinotta, L. Heilbronn, D. Stephens, J.J.R.r. Wilson, Benchmark studies of the effectiveness of structural and internal materials as radiation shielding for the international space station, 159(3) (2003) 381-390

[217] V. Yamakov, C. Park, J.H. Kang, X. Chen, C. Ke, C.J.C.M.S. Fay, Piezoelectric and elastic properties of multiwall boron-nitride nanotubes and their fibers: A molecular dynamics study, 135 (2017) 29-42

[218] J.H. Kang, G. Sauti, C. Park, V.I. Yamakov, K.E. Wise, S.E. Lowther, C.C. Fay, S.A. Thibeault, R.G.J.A.N. Bryant, Multifunctional electroactive nanocomposites based on piezoelectric boron nitride nanotubes, 9(12) (2015) 11942-11950

[219] J.H. Kang, G. Sauti, C. Park, V.I. Yamakov, K.E. Wise, S.E. Lowther, C.C. Fay, S.A. Thibeault, R.G. Bryant, Multifunctional Electroactive Nanocomposites Based on Piezoelectric Boron Nitride Nanotubes, ACS Nano 9(12) (2015) 11942-11950.10.1021/acsnano.5b04526

[220] D. Lee, F.-G. Yuan, C. Fay, S.-H. Chu, C. Park, Piezoelectric characterization of boron nitride nanotube-polyurethane composites, Micro-and Nanotechnology Sensors, Systems, and Applications XI, International Society for Optics and Photonics, 2019, p. 1098233

[221] J. Yao, C. Xiong, L. Dong, C. Chen, Y. Lei, L. Chen, R. Li, Q. Zhu, X. Liu, Enhancement of dielectric constant and piezoelectric coefficient of ceramic-polymer composites by interface chelation, J. Mater. Chem. 19(18) (2009) 2817-2821.10.1039/B819910H

[222] J. Zhang, S. Ye, H. Liu, X. Chen, X. Chen, B. Li, W. Tang, Q. Meng, P. Ding, H. Tian, X. Li, Y. Zhang, P. Xu, J. Shao, 3D printed piezoelectric BNNTs nanocomposites with tunable interface and microarchitectures for self-powered conformal sensors, Nano Energy 77 (2020) 105300.<https://doi.org/10.1016/j.nanoen.2020.105300>

[223] X. Chen, L. Zhang, C. Park, C.C. Fay, X. Wang, C. Ke, Mechanical strength of boron nitride nanotube-polymer interfaces, *Appl. Phys. Lett.* 107(25) (2015) 253105.10.1063/1.4936755

[224] S.-H. Kang, S.-W. Jeon, S.Y. Moon, Y.-J. Yoon, T.-H. Kim, Fabrication of Noncovalently Functionalized Boron Nitride Nanotubes with High Stability and Water-Redispersibility, *The Journal of Physical Chemistry Letters* 11(11) (2020) 4511-4516.10.1021/acs.jpclett.0c01177

[225] C. Zhi, Y. Bando, C. Tang, S. Honda, K. Sato, H. Kuwahara, D. Golberg, Covalent Functionalization: Towards Soluble Multiwalled Boron Nitride Nanotubes, *Angew. Chem. Int. Ed.* 44(48) (2005) 7932-7935.<https://doi.org/10.1002/anie.200502846>

[226] T. Sainsbury, T. Ikuno, D. Okawa, D. Pacilé, J.M.J. Fréchet, A. Zettl, Self-Assembly of Gold Nanoparticles at the Surface of Amine- and Thiol-Functionalized Boron Nitride Nanotubes, *The Journal of Physical Chemistry C* 111(35) (2007) 12992-12999.10.1021/jp072958n

[227] T. Ikuno, T. Sainsbury, D. Okawa, J.M.J. Fréchet, A. Zettl, Amine-functionalized boron nitride nanotubes, *Solid State Commun.* 142(11) (2007) 643-646.<https://doi.org/10.1016/j.ssc.2007.04.010>

[228] C.Y. Zhi, Y. Bando, T. Terao, C.C. Tang, H. Kuwahara, D. Golberg, Chemically Activated Boron Nitride Nanotubes, *Chemistry – An Asian Journal* 4(10) (2009) 1536-1540.<https://doi.org/10.1002/asia.200900158>

[229] C. Zhi, Y. Bando, C. Tang, R. Xie, T. Sekiguchi, D. Golberg, Perfectly Dissolved Boron Nitride Nanotubes Due to Polymer Wrapping, *J. Am. Chem. Soc.* 127(46) (2005) 15996-15997.10.1021/ja053917c

[230] G. Ciofani, S. Danti, D. D'Alessandro, S. Moscato, A. Menciassi, Assessing cytotoxicity of boron nitride nanotubes: Interference with the MTT assay, *Biochem. Biophys. Res. Commun.* 394(2) (2010) 405-411.<https://doi.org/10.1016/j.bbrc.2010.03.035>

[231] G. Ciofani, V. Raffa, A. Menciassi, A. Cuschieri, Cytocompatibility, interactions, and uptake of polyethyleneimine-coated boron nitride nanotubes by living cells: Confirmation of their potential for biomedical applications, *Biotechnol. Bioeng.* 101(4) (2008) 850-858.<https://doi.org/10.1002/bit.21952>

[232] D. Köken, Synthesis and optimization of boron nitride nanotubes for stable aqueous dispersions, 2016,

[233] G. Ciofani, L. Ricotti, S. Danti, S. Moscato, C. Nesti, D. D'Alessandro, D. Dinucci, F. Chiellini, A. Pietrabissa, M. Petrini, A. Menciassi, Investigation of interactions between poly-L-lysine-coated boron nitride nanotubes and C2C12 cells: uptake, cytocompatibility, and differentiation, *Int J Nanomedicine* 5 (2010) 285-298.10.2147/ijn.s9879

[234] H. Sojoudi, S. Kim, H. Zhao, R.K. Annavarapu, D. Mariappan, A.J. Hart, G.H. McKinley, K.K. Gleason, Stable Wettability Control of Nanoporous Microstructures by iCVD Coating of Carbon Nanotubes, *ACS Applied Materials & Interfaces* 9(49) (2017) 43287-43299.10.1021/acsami.7b13713

[235] K.K.S. Lau, J. Bico, K.B.K. Teo, M. Chhowalla, G.A.J. Amaralunga, W.I. Milne, G.H. McKinley, K.K. Gleason, Superhydrophobic Carbon Nanotube Forests, *Nano Lett.* 3(12) (2003) 1701-1705.10.1021/nl034704t

[236] Y. Ye, Y. Mao, F. Wang, H. Lu, L. Qu, L. Dai, Solvent-free functionalization and transfer of aligned carbon nanotubes with vapor-deposited polymer nanocoatings, *J. Mater. Chem.* 21(3) (2011) 837-842.10.1039/C0JM02506B

[237] S.J. Yu, K. Pak, M.J. Kwak, M. Joo, B.J. Kim, M.S. Oh, J. Baek, H. Park, G. Choi, D.H. Kim, J. Choi, Y. Choi, J. Shin, H. Moon, E. Lee, S.G. Im, Initiated Chemical Vapor Deposition: A Versatile Tool for Various Device Applications, *Adv. Eng. Mater.* 20(3) (2018) 1700622.<https://doi.org/10.1002/adem.201700622>

[238] O. Mohammadmoradi, G. Ozaydin Ince, Encapsulation of interdigitated electrodes by PTFE coatings via closed batch initiated chemical vapor deposition, *Vacuum* (2021) 110691.<https://doi.org/10.1016/j.vacuum.2021.110691>

[239] K.K.S. Lau, K.K. Gleason, Initiated Chemical Vapor Deposition (iCVD) of Poly(alkyl acrylates): A Kinetic Model, *Macromolecules* 39(10) (2006) 3695-3703.10.1021/ma0601621

[240] A. Pakdel, C. Zhi, Y. Bando, T. Nakayama, D. Golberg, A comprehensive analysis of the CVD growth of boron nitride nanotubes, *Nanotechnology* 23(21) (2012) 215601.<https://doi.org/10.1088/0957-4484/23/21/215601>

[241] A. Pakdel, C. Zhi, Y. Bando, D. Golberg, Low-dimensional boron nitride nanomaterials, *Mater. Today* 15(6) (2012) 256-265.[https://doi.org/10.1016/S1369-7021\(12\)70116-5](https://doi.org/10.1016/S1369-7021(12)70116-5)

[242] P. Ahmad, M.U. Khandaker, Y.M. Amin, Synthesis of boron nitride nanotubes by Argon supported Thermal Chemical Vapor Deposition, *Physica E: Low-dimensional Systems and Nanostructures* 67 (2015) 33-37.<https://doi.org/10.1016/j.physe.2014.11.003>

[243] T. Oku, I. Narita, A. Nishiwaki, Atomic structures of bamboo-type boron nitride nanotubes with cup-stacked structures, *Journal of the European Ceramic Society* 26(4) (2006) 443-448.<https://doi.org/10.1016/j.jeurceramsoc.2005.07.037>

[244] D. Golberg, W. Han, Y. Bando, L. Bourgeois, K. Kurashima, T. Sato, Fine structure of boron nitride nanotubes produced from carbon nanotubes by a substitution reaction, *J. Appl. Phys.* 86(4) (1999) 2364-2366.<https://doi.org/10.1063/1.371058>

[245] Z. Gao, C. Zhi, Y. Bando, D. Golberg, M. Komiyama, T. Serizawa, Efficient disentanglement of boron nitride nanotubes using water-soluble polysaccharides for protein immobilization, *RSC Advances* 2(15) (2012) 6200-6208.<https://doi.org/10.1039/C2RA20765F>

[246] L. Wirtz, A. Rubio, R.A. de la Concha, A. Loiseau, Ab initio calculations of the lattice dynamics of boron nitride nanotubes, *Physical Review B* 68(4) (2003) 045425.<https://doi.org/10.1103/PhysRevB.68.045425>

[247] B. Pankoke, K.M.T. Yamada, G. Winnewisser, High Resolution IR-Spectra of Furane and Thiophene, *Zeitschrift für Naturforschung A* 48(12) (1993) 1193-1202.<https://doi.org/10.1515/zna-1993-1207>

[248] C. Chen, Z. Jia, X. Wang, H. Lu, Z. Guan, C. Yang, Micro Characterization and Degradation Mechanism of Liquid Silicone Rubber Used for External Insulation, Dielectrics and Electrical Insulation, *IEEE Transactions on* 22 (2015) 313-321.<https://doi.org/10.1109/TDEI.2014.004188>

[249] R. Arenal, A.C. Ferrari, S. Reich, L. Wirtz, J.Y. Mevellec, S. Lefrant, A. Rubio, A. Loiseau, Raman Spectroscopy of Single-Wall Boron Nitride Nanotubes, *Nano Lett.* 6(8) (2006) 1812-1816.<https://doi.org/10.1021/nl0602544>

[250] Y. Yorulmaz, Optimization of synthesis conditions of boron nitride nanotubes (BNNTS) and their effects on epoxy resin curing, Sabanci University, 2018,

[251] S.B. Giddings, Hawking radiation, the Stefan–Boltzmann law, and unitarization, *Phys. Lett. B* 754 (2016) 39-42.<https://doi.org/10.1016/j.physletb.2015.12.076>

[252] V. Yablokov, Y.A. Vasina, I. Zelyaev, S. Mitrofanova, Kinetics of thermal decomposition of sulfur-containing amino acids, Russian Journal of General Chemistry 79(6) (2009) 1141-1145.<https://doi.org/10.1134/S1070363209060188>

[253] A.K. Vasiliou, H. Hu, T.W. Cowell, J.C. Whitman, J. Porterfield, C.A. Parish, Modeling Oil Shale Pyrolysis: High-Temperature Unimolecular Decomposition Pathways for Thiophene, The Journal of Physical Chemistry A 121(40) (2017) 7655-7666.<https://doi.org/10.1021/acs.jpca.7b07582>

[254] T.V. Reshetenko, S.R. Khairulin, Z.R. Ismagilov, V.V. Kuznetsov, Study of the reaction of high-temperature H₂S decomposition on metal oxides (γ -Al₂O₃, α -Fe₂O₃,V₂O₅), Int. J. Hydrogen Energy 27(4) (2002) 387-394.[https://doi.org/10.1016/S0360-3199\(01\)00143-4](https://doi.org/10.1016/S0360-3199(01)00143-4)

[255] K.S. Kim, T.H. Kim, Nanofabrication by thermal plasma jets: From nanoparticles to low-dimensional nanomaterials, J. Appl. Phys. 125(7) (2019) 070901.10.1063/1.5060977

[256] S. Şener, G. Özbayoğlu, Separation of ulexite from colemanite by calcination, Miner. Eng. 8(6) (1995) 697-704.[https://doi.org/10.1016/0892-6875\(95\)00030-T](https://doi.org/10.1016/0892-6875(95)00030-T)

CURRICULUM VITAE

Deniz Köken

EDUCATION

Sabanci University (Full Tuition Fee Exemption) 2017-Current

Ph.D. in Material Science and Nanoengineering (GPA 3.67/4.0)

Sabanci University (Full Tuition Fee Exemption) 2014-2016

MSc in Material Science and Nanoengineering (GPA 3.8/4.0)

Yıldız Technical University 2010-2014

BSc in Material Science and Engineering (GPA 3.2/4.0)

PUBLICATIONS

&

PRESENTATIONS

SUP137-Hiyerarşik Yapıya Sahip Mikro-/Ya Da Nanomalzeme – **Patent, Published (TR 2017 22996 A2)**

Photothermal waterborne polydopamine/polyurethanes with light-to-heat conversion properties – **Journal Article, Accepted (ACS Applied Polymer Materials)**

Waterborne polydopamine-polyurethane/polyethylene glycol-based phase change materials for solar-to-thermal energy conversion and storage – **Journal Article, Accepted (Industrial & Engineering Chemistry Research)**

An Effective Growth of Hierarchical BNNTs/SiC Fibers with Enhanced Interfacial Properties – **Journal Article, Accepted (Composite Science and Technology)**

Sulfur assisted, Low Temperature Synthesis of BNNTs By CVD From Various Boron Minerals – **Journal Article, Under Review (ACS Applied Nano Materials)**

Functionalization of BNNT surfaces with Teflon by ICVD technique. – **Journal Article, In progress**

Polymer/BNMF composites fabrication to be used in electrical applications. – **Journal Article/Patent, In progress**

Synthesis of Boron Nitride Nanotubes on Silicon Carbide Fibers and Investigation of the Mechanical Properties – **Poster Presentation, MRS'17 Fall, Boston**

Synthesis and Characterization of Boron Nitride Nanotubes on Ceramic Nanofibrous Materials – **Poster Presentation, MRS'17 Fall, Boston**

Synthesis of Boron Nitride Nanotubes via Growth Vapor Trapping-BOCVD for Stable Aqueous Dispersions – **Oral Presentation, NanoTR-13**

Synthesis of Boron Nitride Nanotubes on Silicon Carbide Fibers for Ceramic Fiber Reinforced Polymer Composites – **Oral Presentation, PPS-35**

THESES

Ph.D. Thesis – Sabancı University/ h-BN Nanostructures: Synthesis and Applications (Advisors: Assoc. Prof. Dr. Fevzi Ç. Cebeci)

- Decoration of the SiC fiber surfaces with “fuzzy fiber” boron nitride nanotubes (BNNTs) were achieved via growth vapor trapping boron oxide chemical vapor deposition (GVT-BOCVD) method
- Successful synthesis of boron nitride nanofibers (BNNFs) was reported followed by the fabrication of polymer/BNNF composites for electrical applications.
- Teflon coating on the BNNTs surfaces were investigated using initiated chemical vapor deposition technique to ensure conformal and thin coating of Teflon on BNNT surfaces.
- Low temperature synthesis of BNNTs was achieved using boron minerals such as colemanite and ulexite with the assistance of sulfur containing molecules.

Master Thesis - Sabancı University) Synthesis and Optimization of Boron Nitride Nanotubes for Stable Aqueous Dispersions (Advisor: Assoc. Prof. Dr. Fevzi Ç. Cebeci, 2014 - 2016)

- Boron oxide chemical vapor deposition-growth vapor trapping method was utilized for the synthesis of BNNTs
- Non-covalent functionalization (Polymer wrapping and Surfactant) of BNNTs allowed efficient dispersion of BNNTs in aqueous media.

BSc Thesis - Yıldız Technical University/ Design of Solar Cell Electrodes Containing Nanotubes (Advisor: Prof. Dr. Figen Kaya, 2013 - 2014)

- Incorporation of carbon nanotubes with TiO₂ nanotubes to create higher efficiency Dye-sensitized solar cells.
- Cheap electrophoretic deposition method to produce electrodes was used.

RESEARCH PROJECTS

ITUNOVA - Safran Group/ An Effective Growth of Hierarchical BNNTs/SiC Fibers with Enhanced Interfacial Properties (Advisor: Assoc. Prof. Dr. Hülya Cebeci, Assoc. Prof. Dr. Fevzi Ç. Cebeci, 2016 - Present)

- Successfully synthesized Boron Nitride Nanotubes on Silicon Carbide Fibers by simple chemical vapor deposition method.
- Decoration of BNNTs improved the interfacial shear strength of the single fiber by 87.8%.

Sabancı University – İstanbul Technical University/ Synthesis and Characterization of Boron Nitride Nanotubes on Ceramic Nanofibrous Materials (Advisor: Assoc. Prof. Dr. Fevzi Ç. Cebeci Assoc. Prof. Dr. Hülya Cebeci, 2016 - Present)

- Unique nanotube/nanofiber structure was achieved.
- Simple catalyzation and the synthesis process allowed novel synthesis

Tubitak – Sabancı University/ Synthesis of Cathode Materials for Li-ion Batteries (Advisor: Dr. Serap Hayat Soytaş, 2014 - 2015)

- Sn nanoparticle doped carbon fibers showed longer lifetime.
- Learned electrospinning technique for synthesis of carbon nanofibers.